DIAGNOSING THE ONSET OF NORTH PACIFIC JET RETRACTIONS USING PIECEWISE TENDENCY DIAGNOSIS AND A LINEAR INVERSE MODEL

By

Melissa L. Breeden

A dissertation submitted in partial fulfillment of

the requirements for the degree of

Doctor of Philosophy

(Department of Atmospheric & Oceanic Sciences)

at the

UNIVERSITY OF WISCONSIN-MADISON

2018

Date of final oral examination: Monday 9 April 2018

The dissertation is approved by the following members of the Final Oral Committee:
  Jonathan E. Martin, Professor, Atmospheric and Oceanic Sciences, UW-Madison
  Michael C. Morgan, Professor, Atmospheric and Oceanic Sciences, UW-Madison
  Daniel J. Vimont, Professor, Atmospheric and Oceanic Sciences, UW-Madison
  David J. Lorenz, Research Scientist, Center for Climatic Research, UW-Madison
  Zhengyu Liu, Professor, Department of Geography, Ohio State University

Acknowledgements

The first person I can remember supporting my interest in science – specifically physics – is my mother. An avid NOVA TV series enthusiast, we watched the episode Brian Greene hosted that dove into string theory and the universe, and we both found it fascinating. She then bought me his book on the subject (I was in the 8th grade) and while I only made it through the first chapter, my interest in physics had been irreversibly piqued. It was also my mother who steadfastly encouraged me to enroll in AP physics, the subject I continued to puruse in my undergraduate studies here at Wisconsin. Without her guidance as an adolescent I literally would not have set out on the path I've now completed in earning this degree.

Beyond this concrete support to pursue my passion for physics, my mother has unwittingly taught me crucial survival skills by example. She hung a painting in our kitchen with the phrase "if your ship doesn't come in, swim out to it", reflecting the toughness (mixed in with a whole lotta love) she taught me and my siblings to embrace. During the most challenging weeks of graduate school, a call to mom would always do the trick. Regardless of if she was advising me to just cry it out, or tough it out, or just chill, the phrase 'mother knows best' has only increased in veracity as the years have go on.

Similarly resilient but in his own way, my father has been a rock of support since I had my first existential crisis at the ripe age of nine. With a calmer, chiller demeanor than my mom, Dad taught me the importance of timing early on – and how important it is to decide whether *seize the moment* or *wait*. When I would call all whipped up about my research or someone at work, Dad would remind me that often times "easy does it", or, to rephrase in Hoosier, "easy trigger". Ever the optimist, my father is one of the mentally strongest people I have ever known, finding something lighthearted and positive in confronting most obstacles.

Spending time with my sister Natalie (and her cat, Louie!) during school breaks was one of my favorite ways to relax between grueling semesters. Excursions to Toni, and times when we were just 'driving around' and goofing off, compose some of my favorite, calming memories during the last several years. Plus all the time spent in Louie's lounge watching our favorite shows and watching our cats 'get along'. Natalie's mental fortitude, and emphasis on self-love, helped me through challenging days and reminded me that *I am enough*, and *what I have done is enough*. Although farther away physically, talking to and spending time in the Grand Canyon with my brother Grant has been instrumental in my getting this far. And this holds literally, since Grant pulled me out of the grown-up pool *twice* when I was a toddler causing trouble. So, really, thank you big brother, for keeping me alive! More recently, Grant has always pushed me to go beyond – to get away from what's comfortable and to explore what is new and unknown. His fearlessness and confidence are something I work on cultivating in myself every day, and have learned to embrace while finishing this degree.

I would not have gone to Wisconsin without the support of my Aunt Claudia. Diagnosed with stage four breast cancer when I was little, it took that disease 18 years to bring her down. During that time, despite the pain and discomfort that constantly followed her, my aunt never complained and only ever filled my life with joy (particularly since we were both among the sassiest of family members). Aunt Claudia drove me to my freshman orientation, pre-ordered my Harry Potter books for me and taught me all the state capitols. Without her, and her quiet, unobtrusive strength during her illness, I wouldn't be as strong or as self-possessed as I am today. My Gram and Grandbob equally shared their strength and love with me, from spaghetti sleepovers (featuring parmigiano-reggianno cheese and manicures) to buying my cello for me, to helping pay for college. Blood is thicker than water, and while as a teenager this was less

obvious, the impact my family has had on me has only become increasingly apparent as time marches forward. Thank you, family!!

My family primed me for graduate school, but unfortunately they don't know much about positive vorticity advection by the thermal wind. For this I had to mix the lessons learned from loved ones with what Professor Jon Martin could teach me. Jon is, literally, the most supportive advisor there ever was or will be. Jon initiated the transition of my research interests from climate variability to synoptic meteorology, and kindled my passion for jet stream dynamics in particular. Regardless of what idea or research question I came up with, Jon somehow managed to maintain only my enthusiasm for research; not a single time comes to mind in which Jon was discouraging, negative, or in any way unsupportive during my five-year journey through this degree. Even more inspiring is how Jon maintains his *own* enthusiasm for research and teaching so far into his career. Learning and working with someone who is so clearly happy in life has been one of the highlights of my higher education. And this includes Jon allowing me to be me – he has put up with my sometimes irregular schedule, excursions to the Electric Forest, and working while laying all-too-comfortably on my office couch, as long as the research was flowing. For such an inspiring and understanding advisor I will be eternally grateful.

In addition to Jon, Professor Galen McKinley was instrumental in helping me become the scientist I am today. As a senior undergraduate Galen trusted me with – and patiently guided me through – a hefty modeling/statistics project through which I learned an enormous amount. Galen is one of the few female professors with whom I've worked closely, and she showed me (whether aware of it or not) what it takes to be a successful professor and mother all at once. She also guided me through my first publication and oral presentation, both enormously important and challenging tasks for a young graduate student. And let's not forget that she sent me to

Hawaii!! In February!! Galen, thank you for your early support and confidence that I could become a scientist at the highest level.

Equally encouraging while I pursued my degree was Professor Michael Morgan. Michael, it seems, can recall just about any equation about anything he learned at any point during his own education at any time. AND, he can recall the most minute and insufferable of details involved in numerical methods used in atmospheric science (potential vorticity inversion I'm lookin' at you). Despite juggling a cornucopia of administrative, scholarly and professional roles, Michael is endlessly patient with students (like me) who storm into his office confused about various scientific or computational problems. Without talking through my research with Michael during the past several years, my own understanding of the atmosphere would be far less complete than it is today. Thank you Michael! And P.S. a hot dog is not a sandwich!!!!! I would also like thank Dr. Brett Hoover, who has financially supported me throughout the last few years of school, and has introduced me to the field of prediction and forecasting. Brett, similar to Michael, seems to have the ability to seamlessly understand a plethora of different methods and perspectives regarding atmospheric prediction. Even more impressive is his extraordinary ability to *communicate* that information, no matter how complicated, to others. Brett has placed a lot of trust in me to work independently and diligently, for which I am exceedingly grateful.

Finally, Professor Dan Vimont has rounded out my mentorship network through a keen and altogether different, statistical understanding of the earth system than Jon and Michael's synoptic approach. The year of statistics I took with Dan opened my eyes to an alternate way to understand my research. And he did so with a slew of jokes, stories, and generally amusing gestures that made learning statistical theory… "fun". Working with and getting to know Dan

has made me a versatile researcher who can understand synoptic methods to diagnose atmospheric phenomena as well as statistical methods – and the power of the blend of these two approaches has heavily influenced the thesis presented here.

Friends are as crucial for earning a doctorate as doing homework and passing your prelim. Early in my degree, I was split between Galen and Jon's groups, which led me to meet some of my closest long-term friends. Alexis and I knew we'd get along when she saw my Harry Potter time turner key chain (a gift from another best friend!). Her blend of intense organization and intelligence with a shockingly expletive-laden sense humor helped me complete my first talk (while we were sipping on mai-tai's at the pool!) and take over as the Welcome Committee chair without disaster striking. Seeing Alexis skype in for my defense boosted me with that last bit of confidence I needed before the presentation began. I love you Alexis!

Andrew, Zak and Kyle were all members of the Martin group when I started graduate school, and our discussions about details and dynamics of the jet stream (which we all studied) gave me a jump-start to the understanding I've cultivated since. Zak was first my TA, later just a colleague I bothered near-constantly about various issues, scientific or otherwise. Now we exchange both jet stream theories *and* Westworld theories on a frequent basis. Andrew showed me how to become a TA, handing down his office and wisdom in preparing for teaching an extremely demanding laboratory section. We catch up so frequently at conferences, and digitally, that new scientific ideas are constantly being discussed and improved and it seems almost as if he never left. Kyle helped me network with other schools, in addition to being perpetually ready to discuss the current weather – with use of his amazing automated maps which I still use today. To these three men – whom I consider my research brothers – I ow a debt of gratitude in mentorship and friendship. After my academic brothers graduated, my

academic sisters, Jessica and Maria, joined the Martin group. Maria and Jessica have provided

unwavering support as I finished this monumental task, and joined in the subsequent celebration

to help make it an ever merrier occasion to celebrate. Between all of us being too involved in

committees (and often complaining about it), to somewhat incessant boy-talk, to drinking wine

in our hotel room during the Cyclone Workshop in Quebec, the last few years has been a blast.

The thoughtfulness of Maria and Jessica, plus their sincerity, is humgling, and overall their

friendship has made me a better person.

My oldest and absolute best friend Ali and I met on Halloween in the fifth grade – she

was Mickey from *Fantasia* and I was a witch. Through over a dozen Halloweens since (most

recently she was eyeballs and I was a lizard), Ali has been a constant source of joy, support and

inspiration as we traversed puberty (not without man terrible at-home hair makeovers), the

transition to college, and all that has come since. Our matching tattoos, impulsively chosen hard

to explain, make me laugh and smile to this day. More recently Ali has been my go-to

powerhouse of motivation to finish this darn degree, having completed her Master's herself.

Every time we get together it fills me with joy and grounds me to what I truly am, and reminds

me where I came from.

My first college roommate was randomly assigned by our 1000-student dorm, and by

some miracle I was matched up with Taylor, who has remained one of my best friends since.

Kind, patient, hard-working and addicted to peanut butter, Taylor is one of the most genuine and

interesting people I know. Her warmth, humor, and positive attitude know no bounds, and some

of her patience has miraculously rubbed off on me through years of living together. I met Casey

soon after Taylor, equally thoughtful and witty as Taylor is (but with more an addiction to cheese

than peanut butter). Together the three of us, with time, love and utter foolishness, became part

of an amazing group of people who danced, hooped, and cajoled their way through our paths to graduation. We also temporarily lived in a tin foil covered space ship apartment. Trent joined in the silliness a few years in, and only made things more ridiculous with his size-14 high heels and peerless smizing. We met Sara senior year, who joined in the fun as if she had been with us the whole time. She introduced me to "the internet" proper, and taught me how to prioritize my own needs without being needlessly aggressive. All the while my best high school friend Sam (calm, collected, German heritage) came along for the ride, donning a Hawks jersey and scoping out good concert spots with his tallness. Driving home to Illinois with Sam and Chroma year after year has been a calming constant in my life (plus, Culver's!). Later in graduate school, friends Dave and Anna joined us for Frozen watch parties (I mean come on it is SO cold here!) enjoying adult beverages and playing endless card games including Exploding Kittens. In finishing my degree, going to Dave's for a distraction of card games, yelling and general shenaniganry was a way to, paradoxically, stay sane. And finally, chatting with Anna, ever supportive and optimistic about my success when I was feeling particularly discouraged, truly helped me make it across the finish line. To all my friends along the way, I cannot thank you enough for reminding me that I am more than my scholarly success.

The past five years have awarded me the opportunities and experiences of a lifetime, from Norway to Hawaii to the AOS rooftop. The AOS department has been more than a place to work, and has shaped me into someone prepared to confront the challenges facing my generation. I cannot thank the department staff, funding, and people who have made this journey towards my doctorate possible. I am now ready to take the skills I've cultivated here, through the help of everyone mentioned above, and apply them to protect our environment and improve the well-being of all of us living on this irreplaceable, hallowed planet.

TABLE OF CONTENTS

FOREWARD: NAVIGATING THIS THESIS

The north Pacific jet stream is one of the most dynamically potent features of the northern hemisphere wintertime circulation and affects the position and strength of the storm track and the associated sensible weather. Given vast connections to atmospheric and coupled phenomena that occur on the order of hours to years, understanding changes in the jet has impacts for phenomena across all timescales. Even glacial changes, which are often viewed as occurring over the scale of millennia, have been traced to anomalous circulation patterns over just one season, which can lead to the rapid destabilization of a glacier from which the feature may not recover. Unsurprisingly, a wealth of previous literature has been devoted to untangling the vast amount of interactions related to the jet, and in particular the 'merged' jet that resides in the north Pacific during boreal winter. Specifically, understanding the transition of the jet from strong and zonal to weak and wavy, and often 'blocked', has been and remains a focal point of ongoing meteorological research.

The present document aims to further understanding of the processes that facilitate the zonal *retraction* of the jet north Pacific stream. This objective is approached by employing two independent diagnostic techniques. First, two case studies of jet retractions, both associated with Hawaiian precipitation and flooding, are presented. Piecewise Tendency Diagnosis (PTD), a quantitative means of partitioning the quasi-geostrophic (QG) height tendencies into contributions from various physical processes, is applied to features associated with retraction onset in each case. Then, PTD is expanded to arrive at a piecewise diagnostic of the geostrophic wind tendency, a novel approach to understanding deceleration of the jet. The background material, methodology and results from applying PTD to two cases, and from the new piecewise zonal wind tendency diagnostic, are presented in Chapters 1-4.

To complement the investigation of individual cases of retractions, an alternative and altogether distinct approach is employed. A linear inverse model (LIM) composed of stream function and tropical outgoing longwave radiation was applied to diagnose structures that routinely precede retractions and, by definition, most rapidly amplify into a retracted state. The LIM is flexible in that growth in the model can be optimized based on any prescribed circulation pattern, such as one associated with jet retractions. The structures that grow most rapidly into the prescribed pattern are determined at various lags and then compared to what is common among the LIM and observations.

Given the differences between the two diagnostic techniques applied, separate, more detailed introduction and methodology sections for the PTD and LIM approaches will be presented in this dissertation. Chapters 1-4 offer an overview of jet stream dynamics and variability, current methods employed to diagnose that variability, and present results from two case studies of jet retractions. Chapter 5 includes the introduction, methodology and results from applying the LIM to examine jet retractions. Chapter 6 will combine these results into a discussion of how these two points of view complement one another and provide a comprehensive understanding of the processes governing jet retractions, and how this knowledge may be applied to forecast retractions, and their associated weather impacts, in the future.

LIST OF TABLES

LIST OF FIGURES

development) in blue.

2.16   Barotropic Deformation. a) The color shading shows the 300hPa $q_u{}'$ field, which is being advected by $\overline{\boldsymbol{v}}_g$, parallel to the geopotential height lines (black contours). The arrows indicate the background geostrophic winds and their ability to advect the $q_u{}'$ field downstream. The white contours show the height anomaly A, and the contour interval is 50m starting at +/- 100 m, positive values only. b) The color shading shows the height tendency field from inverting Term A in Eqn (2.6), $(-\overline{\mathbf{v}}_g \cdot \nabla q_u')$, at 00z 13 February. Contour interval is 50m starting at +/- 100 m, positive (negative) is solid (dashed) lines, and zero is solid. The A indicates the location of maximum height of Feature A, and positive tendencies overlapping with A indicates that this term is aiding in further development of A.

2.17   Time series of barotropic and baroclinic contributions to Term A in Eqn (2.6). The sum of the right-hand-side of Eqn (2.6) is shown in red. Units m*(6hr)$^{-1}$.

2.18   As in Figure 2.16, but for 00z on February 14$^{\text{th}}$.

2.19   Time series of all terms on the right-hand-side of Eqn 2.6: Term A, deformation/superposition, is in green, the sum of Term B (downstream development) and PV intrusion component of Term C (baroclinic development, 750-550hPa) is in dark blue, surface component Term C (baroclinic development, 800-1000hPa) is in light blue, and the sum of Terms D and E (vortex-vortex interactions) is in pink. The red line is the sum of all terms in Eqn 2.6.

2.20   11-15 February mean QGPV at 300hPa, units $10^{-4}\,\text{s}^{-1}$.
3.1   The fill shows the potential temperature anomalies on the 2PVU surface on a) 13 b) 16 and c) 19 February 2006. Jet retraction began 15-16 February (Jaffe et al., 2011). The potential temperature anomalies were calculated with respect to the 1979-2015 mean for each day. The contours show the total 315, 330 and 345 K potential temperature surfaces on the 2PVU surface at each time. Anticyclonic anomalies A and B are labeled.

3.2   Schematic demonstrating the distribution of the local acceleration of the zonal wind around a positive height anomaly. Where height tendencies increase with latitude, the zonal wind will weaken, and where height tendencies decrease with latitude, the zonal wind will strengthen (blue arrows).   Adding the blue arrows to a mean westerly wind on the ridge's southern edge indicates the effect of a ridge north of the jet, and its ability to weaken the zonal jet.

3.3   In the top panels the fill is the 300hPa height tendency field on a) 11 February and c) 12 February. Units of height tendencies are meters per six hours, with values less than a magnitude of 15 m (6hr)$^{-1}$ whited out. In contours are the 300hPa height anomalies, calculated with respect to the 11-15 February time mean (same anomaly definition as PTD in part one of this paper). Contours start

at +/-50 m every 100m, solid positive and negative dashed. Anticyclonic anomalies A and B are labeled. In the bottom panels the fill shows the corresponding change in the geostrophic zonal wind calculated from the height tendency fields on b) 11 February and d) 12 February. Units of deceleration are m s^{-1} (6hr)$^{-1}$, and values less than a magnitude of 4 are whited out. The contours show the geostrophic wind contoured every 10 m s^{-1} starting at 30 m s^{-1}.

3.4   As in Fig. 3.3 but for a), b) 13 February and c), d) 14 February 2006.

3.5   The fill shows the 11-15 February change in zonal wind in m s^{-1}. The contours show the 11-15 February mean geostrophic zonal wind, contoured starting at 30 m s^{-1} every 10 m s^{-1}. The green box indicates the region over which the retraction is diagnosed.

3.6   Time series tracking zonal wind change (units m s^{-1} (6 hr)$^{-1}$ averaged from 170-200°W, 30-40°N, from 11-15 February, using six-hourly data. a) shows deceleration using the total height field (black line), height anomaly field (blue line) and the inverted height anomaly field associated with 50-500hPa perturbation QGPV (pink line). b) The pink line is as in a), and the red line shows the deceleration explained using the height tendencies from PTD (Eqn 3.6). The close correspondence between the time series provides confidence in the ability of the PTD methodology to explain the majority of the observed jet retraction.

3.7   Time series of the individual PTD components' contribution to deceleration using Eqn 3.6 from 11-15 February. The red line is the sum of all terms, the green line is Term A, dark blue line Term B, light blue line Term C, pink line Term D, and yellow line Term E, from Eqn 3.6.

3.8   The color shading shows the integrated deceleration from 00z 11 February – 18z 15 February 2006 from terms in Eqn (4.6) in ms^{-1}. a) shows the sum of terms A-E, b) Term A (advection by mean flow, deformation, superposition), c) Term B (downstream development), d) Term C (baroclinic development), e) Term D (upper-level vortex-vortex interactions), and f) Term E (low-level vortex-vortex interactions). The contours in each plot are the same and show the 11-15 February mean geostrophic wind, contoured starting at 30 m s^{-1} at intervals of 10 m s^{-1}.

3.9   a) The color shading shows the 12 February average q'_u field in units of 10^{-4} s^{-1}. The black contours show the 12 February average ϕ'_u field, with positive (negative) values in solid (dashed) lines contoured starting at +/- 20 m every 100 m. Red arrows denote v'_{gu}. b) The color shading shows the 12 February height tendencies associated with Term D and the forcing shown in (a). Height tendencies are in units m (6hr)$^{-1}$, with positive values about 10 shown. The black contours are as in (a).

3.10   The color shading shows the average height tendencies associated with Term D, with values less than 5 m (6hr)$^{-1}$ whited out. The black contours show the 11-15

ABSTRACT

The north Pacific jet stream is a powerful dynamic feature of the circulation during boreal winter, simultaneously reacting to and guiding the evolution of transient midlatitude disturbances, and bearing the shock caused by divergent outflow from tropical convection. The transition of the north Pacific jet from a strong, zonally-extended jet core to a weaker, wavier state remains a challenging phenomenon to predict and to understand dynamically. The present dissertation aims to further understanding of the zonal retraction of the north Pacific jet through case study analysis and analysis of output from a linear inverse model. Case studies reveal that anticyclonic wave breaking often coincides with retraction onset and maintenance. The lifecycles of two high-amplitude anticyclonic anomalies, both of which ultimately overturn anticyclonically, are diagnosed within a quasi-geostrophic framework using Piecewise Tendency Diagnosis (PTD), a quantitative means of partitioning the Quasi-Geostrophic (QG) height tendencies into contributions from various physical processes. Application of this method reveals that barotropic deformation heavily influences the development in both cases.

To diagnose how the features involved in retraction force the zonal geostrophic wind to weaken, a novel extension of PTD is introduced to diagnose geostrophic zonal wind tendencies in a piecewise manner. In both cases, nonlinear potential vorticity advection drives the weakening of the zonal wind. The synoptic context in which this nonlinear eddy feedback leads to retraction involves a positively-tilted wave train located on the cyclonic shear side of the jet. This configuration is conducive to barotropic growth, consistent with the dominance of barotropic deformation in the lifecycles of the waves that develop during retraction.

To complement results from these two case studies, a linear inverse model (LIM) was employed to diagnose the optimal structures that would most rapidly amplify into a pattern

associated with retraction. The resultant optimal initial pattern includes features identified in the case studies as important for retraction onset, particularly anticyclonic anomalies located poleward of the jet entrance region over Eurasia and downstream in the eastern Pacific. The consistency between the features identified in individual cases and by the LIM provides a robust understanding of retraction onset through two independent methods.

CHAPTER ONE: INTRODUCTION TO JET VARIABILITY AND BLOCKING

The tropopause-level jet stream in the north Pacific is one of the most dynamically influential features on the planet, affecting both the day-to-day sensible weather as well as elements of the low-frequency general circulation around the globe (Palmén 1948; Namias and Clapp 1949; Krishnamurti 1961; Eichelberger and Hartmann 2007; Martius et al 2010; Winters and Martin 2014; Rothlisberger et al. 2016; Griffin and Martin 2017). At the same time, it is one of the most complex structures as it is affected by tropical convection, continental, monsoon-scale cold surges, and internal jet dynamics, all acting together within very close proximity in the north Pacific. Hadley (1735) first introduced the notion of an atmospheric circulation cell wherein tropical air moves poleward at high altitude. Held and Hou (1980) used a simplified channel model to demonstrate that air parcels moving northward on a rotating sphere, as occurs in the tropics when divergent outflow from deep convection is produced, conserve angular momentum and lead to westerly acceleration. Thus a subtropical jet forms at the edge of the Hadley Cell, generally around 30°N (Krishnamurti 1961). Assuming geostrophic and hydrostatic balance, the presence of a horizontal temperature gradient corresponds to substantial vertical wind shear, manifested as strong wind speeds in the upper troposphere (Reiter 1963). There are thus two mechanisms by which the strong westerlies observed in the midlatitude upper troposphere are produced, momentum transport and thermal wind balance, both constantly occurring and leading to a climatological westerly jet in both hemispheres.

Initially observed by Ooishi in the 1920s using balloons in Japan (Lewis 2003), the East Asian, or north Pacific, jet stream is a focal point of ongoing research. Given the proximity of strong tropical convection in the west Pacific and a strong temperature gradient off the coast of Eurasia during boreal winter, the north Pacific jet becomes a 'merged' subtropical and eddy-

driven feature (Hoskins and Valdes 1990; Eichelberger and Hartmann 2007; Handlos and Martin 2016). The climatological storm tracks, regions of greatest eddy kinetic energy, are located on the northern side of the north Pacific and Atlantic jet streams, near their exit regions (Blackmon et al., 1977; Athanasiadis et al. 2010). By altering the paths of synoptic features, changes in the strength and position of the jet affect sensible weather across the globe, particularly over the United States and North Atlantic (Strong and Magnusdottir 2008; Moore et al 2010; Winters and Martin 2014; Henderson et al. 2016; Griffin and Martin 2017).

The jet stream varies in strength and position throughout the year, becoming stronger in the winter hemisphere when the meridional temperature gradient intensifies (Ooishi 1926; Palmén 1948; Weickmann and Chervin 1988; Newman and Sardeshmukh 1998). In addition to a pronounced seasonal cycle, substantial intra-seasonal variability prevails, often associated with low-frequency, high-impact weather including atmospheric blocking, large-scale cyclones, and changes in the track and frequency of extratropical cyclones (Rex 1950; Palmén and Newton 1969; Dole and Gordon 1983). As an example, the north Pacific jet on 11 February 2006 is shown in Fig. 1.1a. At this time the jet core had a value of 80 m s^{-1} and extended as one zonal feature from eastern China to 160°W. A broad region of lower heights was located in the central Pacific north of the strong jet core, while the western edge of a high-amplitude ridge over the west coast of North America marked the jet exit region. The ridge corresponded to warmer temperatures on the west coast, and cooler temperatures downstream over the central United States where a trough was present. On 20 February 2006, the jet core was much weaker and zonally confined to the west Pacific (Fig. 1.1b). "Split flow" characterized the central Pacific, as winds were diverted around the sprawling anticyclone. A trough was now located over the west coast, indicating cooler temperatures, in contrast to the flow pattern on 11 February.

Understanding the relationship between the jet, and changes in sensible weather associated with different jet configurations, has been the focus of a large body of research since the 1940's. The pattern of divergence around the jet entrance and exit regions provides preferential regions for mass evacuation and surface cyclogenesis (Namias and Clapp 1949). Periods when the zonal, westerly flow rapidly breaks down and becomes 'blocked' were investigated by Namias (1947), Elliot and Smith (1949) and Rex (1950), who were perplexed by the stark changes in sensible weather observed in a broad region that extended thousands of kilometers beyond the block itself. Baroclinic disturbances indeed rely upon the jet for their energy source, converting available potential energy to eddy kinetic energy. Thus by understanding changes in the jet, a wealth of understanding linked to sensible weather and longer-term climate fluctuations is attained.

1.1 Teleconnections and Wave Breaking

Motivated by the changes in the position and strength of the jet on monthly, weekly, and daily timescales, and the far-reaching influence such changes can exert on sensible weather, many studies have investigated coherent modes of variability in the middle-to-upper troposphere. Wallace and Gutzler (1981) investigated the covariance of monthly-mean 500hPa geopotential height anomalies for December-February 1962-1977, by correlating various base points around the Northern Hemisphere with the total two-dimensional height field. Their analysis revealed the presence of large-scale 'teleconnection' patterns where certain geopotential height anomalies separated by great distances varied together, often as dipoles or quadrupoles. In the Pacific basin, the Pacific-North American (PNA) pattern, a quadrupole structure, whose positive phase is characterized by an anticyclonic anomaly in the subtropical central Pacific, a sprawling cyclonic feature to its north in the midlatitudes, followed by another trough-ridge pair

downstream over the west coast of North America and the southeastern United States, prevailed (Figure 1.2). Blackmon et al. (1984) performed a similar analysis on daily mean 500hPa geopotential height fields but filtered for long (>30 days), intermediate (10-30 days) and short (2.5-6 day) timescales. They found that long-time-scale teleconnections involved a geographically-fixed dipole structure that flanked the jet exit regions of the east Asian/north Pacific and Atlantic jet streams. In the Pacific sector the anomalies were consistent with the location of the PNA pattern centers of action identified by Wallace and Gutzler (1981). Horel and Wallace (1981) demonstrated that there is a strong correlation between the phase of the El Nino-Southern Oscillation (ENSO) and the long timescale PNA anomalies.

In addition to the low-frequency, stationary teleconnection pattern, Blackmon et al (1984) found that the intermediate timescale teleconnection in the north Pacific also revealed a PNA-like structure. The authors described the pattern as a 'mobile' teleconnection pattern that is not rooted in stationary features, but interestingly resembles the monthly-timescale teleconnection pattern in the Pacific. It is clear that a PNA-like pattern is a characteristic 'mode' of variability, given its prevalence in height anomalies with a frequency in a broad range from ten days to longer than 30 days. While the low-frequency pattern has been linked to ENSO, an explanation for the 'mobile' teleconnection pattern eludes consensus.

Another curious characteristic of the jet is that it both modulates, and is modulated by, the lifecycles of transient, baroclinic eddies. Simmons and Hoskins (1980) used a baroclinic channel model and varied the shear in the domain to investigate how this alteration to the background state affects the lifecycle of a prescribed, small-amplitude perturbation. Thorncroft et al. (1993) performed a similar experiment at higher resolution, and found that enhancing the cyclonic shear in the domain leads to what they termed an 'LC2' type lifecycle, wherein a

developing cyclone remains on the cyclonic shear side of the jet and continues to rotate

cylonically as it decays (Figure 1.3b). In contrast, the same initial disturbance growing in a basic

state characterized by relatively reduced cyclonic shear was observed to migrate from the

cyclonic to anticyclonic shear side of the jet, while changing tilt from NW/SE (negative tilt) to

NE/SW (positive tilt) (Figure 1.3a). In the latter example, a streamer of high, cyclonic potential

vorticity (PV) air is cutoff while the disturbance decays, reflective of Rossby wave breaking,

defined as the reversal of the climatological meridional PV gradient which points south-north

(McIntyre and Palmer 1983). Thorncroft et al. (1993) dubbed this particular lifecycle 'LC1',

terminology that has been adopted by many authors since. Wave breaking is a frequent precursor

to midlatitude blocking (Pelly and Hoskins 2003), so additional understanding of the

environments conducive to the LC1/LC2 lifecycles is desired.

Changing the mean shear in the environment or background state dramatically alters the

evolution of identical initial disturbances. Simultaneously, the momentum and heat transport

achieved by the evolving waves influences the mean state, and Thorncroft et al. (1993)

diagnosed this eddy-mean feedback for the LC1/LC2 simulations. They applied two-

dimensional Eliassen-Palm flux diagnostics after Edmon et al. (1980) and showed that the LC1

lifecycle accelerated the zonal mean, zonal wind to the north of its original location, while the

LC2 lifecycle strengthened it to the south.

Wave breaking is formally understood as the process by which a wave propagating along

a potential vorticity (PV) gradient suddenly becomes stationary, starts to tilt, and ultimately

overturns. Large-scale mixing and an 'irreversible' rearrangement of the mean flow results

(McIntyre and Palmer 1983). Linear wave theory states that the location where this occurs, the

'critical surface', coincides with where the phase speed of the wave equals the mean zonal wind.

A common way to measure this is through the stationary wave number K_s, which is inversely

proportional to the zonal wind $\overline{U}$ and directly proportional to the meridional gradient of absolute

vorticity $\beta^* = \beta \quad - \frac{\partial^2 \overline{U}}{\partial y^2}$:

$$K_s = \sqrt{\frac{\beta^*}{\overline{U}}} \qquad (1.1)$$

The jet stream is characterized by a strong meridional absolute vorticity gradient relative to the

zonal wind as a result of strong shear, leading to a higher stationary wave number north of the jet

(Hoskins and Ambrizzi (1993)). Also, the stationary wave number increases at lower latitudes,

where the planetary vorticity gradient increases.

Since teleconnections, jet variability and wave breaking are physically related, clarifying

the finer points of their relationship remains an active area of research. Martius et al. (2007)

showed how the frequency of *LC1/LC2* wave breaking events, identified via PV streamers on

various isentropic surfaces, differed significantly during various phases of well-known

teleconnection patterns like the PNA and North Atlantic Oscillation (NAO). Pertinent to the

present thesis is the reduction in LC2 (cyclonic) wave breaking associated with the negative

polarity of the PNA, during which time a sprawling anticyclone is present in the central north

Pacific and the jet is retracted. Martius et al. (2007) found the primary change in wave breaking

frequency on 310K during the negative PNA occurs in the vicinity of the midlatitude

anticyclone, which suppresses baroclinic wave activity and cyclone development in that region.

Franzke et al. (2011) examined the synoptic evolution of each phase of the PNA and found that

the negative phase coincides with a weaker jet and a series of anticyclonic/LC1 wave breaking

events, consistent with the results of Martius et al. (2007). Associated with LC1 wave breaking

is the formation of a trough that forms and is advected equatorward by the large anticyclonic

feature surging northward (Figure 1.4). Consistent with the association between low-latitude troughs and LC1 wave breaking, Otkin and Martin (2004) found that subtropical (or Kona) cyclogenesis, known to enhance Hawaiian precipitation (Otkin and Martin 2004), is more frequent during the negative PNA phase as a result of the diverted storm track.

1.2 Jet Stream Variability

Rapid changes in the westerlies, particularly the transition from strong, zonal westerlies to sinuous, blocked flow, have begged explanation for decades. Rex (1950) compared blocks in the atmosphere to hydraulic jumps as studied in fluid mechanics. A hydraulic jump is a region characterized by a flow discontinuity, which he described as a region where a laminar current would break down into turbulent eddies. He argued that deformation associated with atmospheric blocks resembled a flow discontinuity, yet how the deformation region was formed remained elusive. Berggren et al. (1949) noted that eddies, defines as deviations from a long-term time mean, approaching diffluent flow are elongated meridionally, leading to their weakening and reinforcement of the low-frequency deformation. Shutts (1983) proposed an eddy straining mechanism to explain the observations of Berggren et al. (1949), by which eddies approaching a block are deformed, leading to a net flux of negative (positive) vorticity into the anticyclonic (cyclonic) branches of a block, maintaining the block's strength. The eddy straining mechanism represents one sort of eddy-mean flow interaction, wherein the transport achieved by migratory eddies reinforces the slowly-varying basic state. Shutts (1983) also observed that this vorticity flux forcing was located on the upstream edge of the block, coincident with the region of deformation, further supporting the notion that the influence of deformation, versus processes in the center of the block, are most important for blocking maintenance.

More recently, Yamazaki and Itoh (2013) proposed an alternative mechanism for the maintenance of blocks through vortex-vortex interactions. Their 'selective absorption mechanism' (SAM) suggests that when eddies of different sizes come into close proximity, the larger anomaly exerts a dominant influence on the smaller one, and that influence acts to either attract or repel the smaller anomaly. Whether the smaller feature is absorbed or repelled depends on the polarity of the two anomalies, and they argued that a large-scale anticyclone will preferentially absorb smaller anticyclonic features, and will repel cyclonic ones. In contrast to the eddy straining mechanism proposed by Shutts (1983), in which the effect of positive and negative anomalies on the block is considered the same, the SAM is dependent upon the signs of the two anomalies that interact. While these two proposed mechanisms emphasize the nonlinear advection of QGPV, they differ dramatically in terms of their explanation for how anticyclonic PV is differentially advected into a blocking anticyclone by eddies.

Eddy-mean interactions occur during many circulation transitions, although much of the literature preferentially focuses on blocking. Hoskins et al. (1983) introduced their **E**-vector (Eqn 1.2) by manipulating the quasi-geostrophic framework to derive relationships between the shape and orientation of height anomalies, and how those characteristics influence the slowly-varying basic state. In this framework a variety of eddy-mean flow interactions may be investigated. The orientation of the **E**-vector is related to the direction of propagation of Rossby wave energy, and depends upon the relative zonal and meridional scales of a wave, as well as its tilt (Fig. 1.5). Hoskins et al. 1983 also showed that **E**-vector convergence is proportional to changes in the low-frequency quasi-geostrophic potential vorticity (QGPV) gradient (and low-frequency geostrophic zonal wind) (Eqns 1.3-1.4). They applied this diagnostic to a blocking anticyclone over the Atlantic in November 1981, and demonstrated that during the block

transient eddies were associated with net QGPV convergence into the blocked region, which coincided with the weak QGPV gradient and quiescent zonal wind observed during the blocked period. The **E**-vectors were strongest near the edges of the block overlapping the deformation regions, and were convergent in the center of the anticyclone, broadly consistent with Shutts' (1983) emphasis on the role of deformation in maintaining blocks.

$$\boldsymbol{E} = \left[\overline{v'^2 - u'^2}, \, \overline{u'v'}, \frac{f_o \overline{v'\theta'}}{\Theta_p} \right] \quad (1.2)$$

$$\left(\partial_t + \overline{\boldsymbol{v_g}} \cdot \nabla \right) \bar{q} + \nabla \cdot \overline{v'q'} = S \quad (1.3)$$

$$\nabla \cdot \overline{v'q'} \approx \partial_y \nabla \cdot \boldsymbol{E} \quad (1.4)$$

Hoskins et al. (1983) also considered the E-vector configuration associated with high- (<10 day) and low- (>10 day) frequency height anomalies for December-February 1979-1980. They found that low-frequency anomalies were associated with a tendency to weaken the zonal wind in the jet exit regions of the north Pacific and Atlantic jet streams, while the high-frequency anomalies provided a forcing for acceleration. They linked the difference in the eddies' feedback on the zonal wind to differences in the horizontal shape of the anomalies, wherein zonally elongated, low-frequency anomalies with lower wave number weaken the zonal jet, and meridionally elongated high-frequency anomalies have a higher wave number and strengthen the zonal jet. Deformation in the flow changes the shape of PV anomalies, which can modify the height field. In turn, changes in the eddy shape can correspond to a change in the eddy feedback on the zonal wind, which may be an important process that aids in the development and maintenance of a particular configuration of the jet. *Further elucidating the physical connections between deformation and eddy-mean interactions, and how they conspire to retract the north Pacific boreal winter jet, is a key goal of this dissertation.*

Mak and Cai (1989) similarly stressed how the shape and orientation of eddies can determine whether eddies are able to extract energy from their environment. In particular, they considered how the tilt of anomalies with respect to the axis of contraction in the flow influences the barotropic energy exchange between eddies and the background state kinetic energy. A positively-tilted trough in a region of cyclonic shear is conducive to barotropic intensification, as kinetic energy is extracted from the background flow and converted to the kinetic energy of the growing disturbance. The right combination of shear and tilt – and therefore baroclinic lifecycle (LC1/LC2) - could conspire to produce an environment in which the mean zonal wind is weakened at the expense of amplifying height anomalies in the flow. Determining the lifecycle of the anomalies related to the onset of jet retractions is a key goal in this thesis, and will reveal information about the relevant processes occurring during retraction.

Understanding the intimate interactions between the environment near a jet, and the way eddies can strengthen or weaken it, requires consideration of the shape, tilt, and position of transient disturbances with respect to deformation. The strength and shear of the zonal wind determines when waves will become stationary (Eqn 1.1), as well as heavily influences their lifecycles (Simmons and Hoskins 1980; Thorncroft et al (1993)). The evolution of waves in a manner similar to the LC1 or LC2 configuration is related to the tilt and shape of the height anomalies, which in turn governs the direction of momentum and temperature fluxes as represented in the E-vector that then feed back onto the mean state (Eqn 1.2). Therefore, understanding changes in the wind speed will advance understanding of subsequent changes in the evolution of transient features and their feedbacks onto the large-scale circulation. In this thesis understanding the eddy-mean feedback(s) that facilitate retraction is a primary goal.

1.3 Previous Research on north Pacific Jet Retractions

The central Pacific anomalies associated with the PNA are similar to the dipole in the leading mode of upper level (250-300mb) zonal wind speed in the north Pacific region, previously identified using empirical orthogonal function (EOF) analysis (Eichelberger and Hartmann 2007; Athanasiadis et al. 2010). This mode of variability represents the zonal extending or retracting of the jet exit region (EOF1), while the second mode indicates a north/south shifting of the exit region (Fig.1.7, EOF2, Athanasiadis et al., 2010; Jaffe et al., 2011; Griffin and Martin 2017). Athanasiadis et al. (2010) calculated the composite divergence of the E-vector for the four phases of the two leading zonal wind modes and showed that the eddy feedback on the zonal wind as represented by **E**-vector convergence was consistent with the zonal wind patterns. They thus concluded that jet variability is heavily influenced by the net effect of transient disturbances. The negative phase of EOF1 coincided with a retracted, split jet stream as in Fig.1.1b, and in their composite was associated with enhanced storm track activity (eddy vorticity flux convergence) weakening the zonal wind in the center of the jet exit region from 180-150°W, and reduced storm track activity (eddy vorticity flux divergence) strengthening the zonal wind north of the jet near 150-180°E. A reversal in storm track activity from its climatological position suggests that retractions are associated with a 'blocked' large-scale circulation pattern. However, even today less is known about the synoptic evolution that *facilitates* the initial weakening of the zonal wind, compared to the amount of research devoted to diagnosing processes occurring during the blocking period. *Accordingly, the first aim of this thesis is to consider the synoptic evolution that facilitates the transition of the north Pacific jet to a retracted state.*

Otkin and Martin (2004) found that the frequency of subtropical cyclones in the basin is greatly modulated by the zonal extent of the upper level jet, captured by EOF1. In particular, a retracted jet is associated with more frequent subtropical 'Kona Low' systems, consistent with the subsequent results of Martius et al. (2007) and Athanasiadis et al. (2010). The results from Otkin and Martin (2004) prompted an interest in the evolution of jet retractions in particular, given their association with Hawaiian precipitation and midlatitude blocking. Jaffe et al. (2011; hereafter JM) first defined criteria for a jet retraction using two independent methods, and examined the composite evolution of the three-dimensional flow field before, during, and after retraction onset (Fig.1.8). Retractions are objectively identified when the mean wind speed in a latitude-longitude box in the central Pacific is less than 10 m s^{-1} below climatology for at least five consecutive days (box location: 25°-40°N, 180°-200°E; JM Fig.2). This location coincides with the greatest amplitude in the pattern of EOF1 of 300mb zonal wind (JM Fig.4). Each case was then visually inspected to verify that the objective identification scheme was truly selecting a retraction, and not a north/south shift in a continuous jet core as represented by EOF2. A total of 19 cases were confirmed by both methods from November-March, 1980-2007.

Ten days before retraction onset (Fig.1.8a), no distinct upper level features are observed, while the jet extends past Hawaii. Five days prior, the jet is still extended, now accompanied by a cyclone in the left exit region and a high-amplitude ridge located downstream over western North America. An equivalent barotropic, sprawling anticyclone in the midlatitude central Pacific follows retraction, accompanied by a linear, cyclonic anomaly to its south in the subtropics (Fig.1.8c-e). Together the circulation of these two features is ideally located to create anomalous easterly winds that counter the westerly jet and maintain a retracted state. Additionally, by Day +5 (Fig.1.8d), anomalies similar to the negative PNA pattern are

exceedingly clear. How the anomaly pattern reverses between Day -5 and Day 0 is not clear from composite analysis, even looking at the daily evolution.

The present thesis seeks to reveal additional information regarding the dynamics that *initiate* the development of the evolution that leads to such dramatic jet transitions. The synoptic evolution and lifecycle analysis of a strong retraction is presented in Chapter 2. In Chapter 3 a novel expansion and application of piecewise tendency diagnosis to diagnose retraction case is presented. The QG diagnostics are then applied to a second retraction case presented in Chapter 4. Finally, an altogether distinct perspective is employed through use of a linear inverse model in Chapter 5. Conclusions drawn from the two methods – QG diagnostics and an empirical model – are presented in Chapter 6.
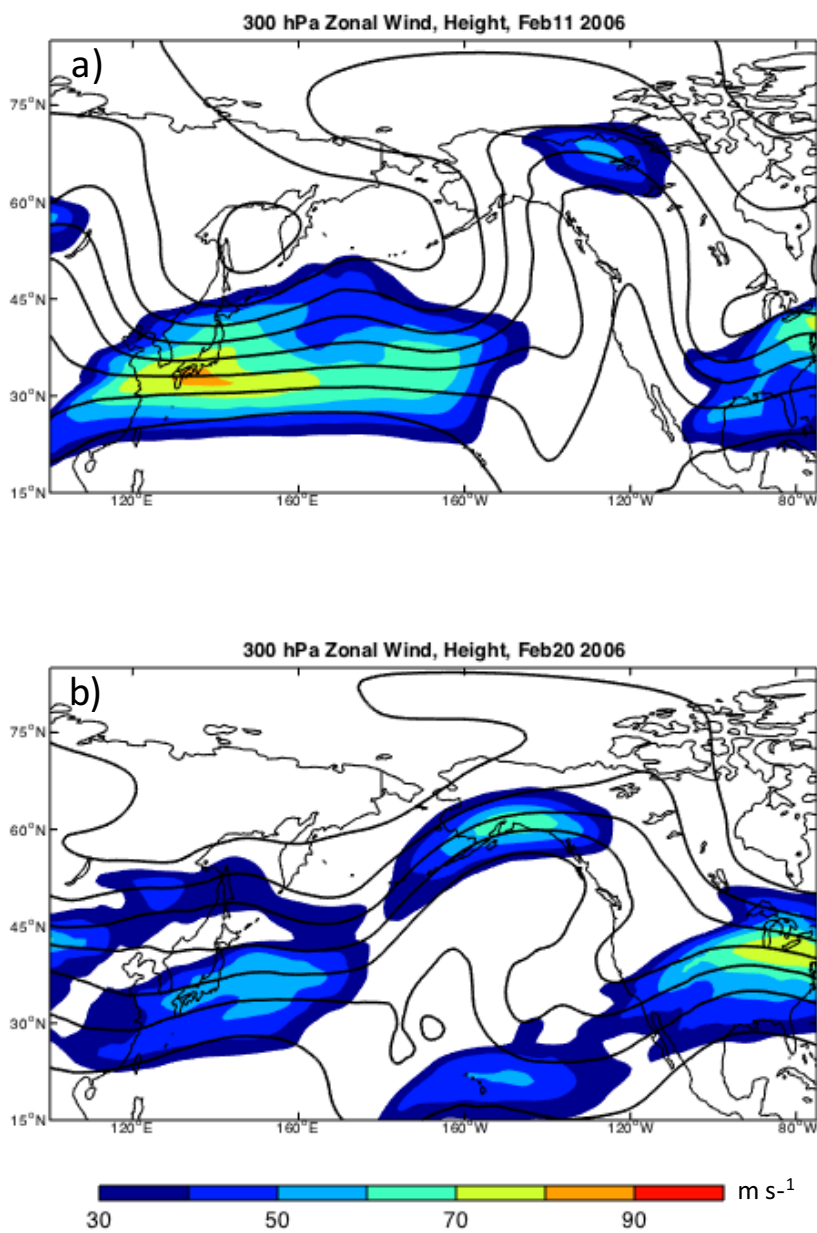
Figure 1.1: Daily mean 300hPa zonal wind on a) 11 February and b) 20 February 2006 is in the color shading in m s^{-1}, and daily mean geopotential height is in the contours in meters starting at 8000m in intervals of 200m.
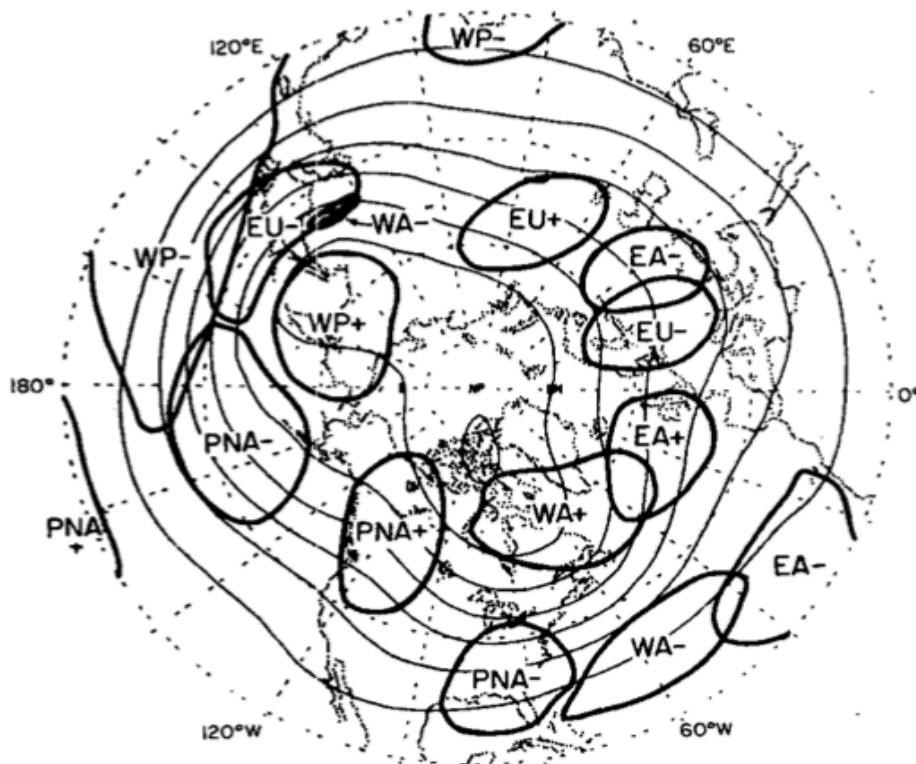
Figure 1.2: Adopted from Wallace and Gutzler (1981). +/- 0.6 isopleths of correlation coefficient between each of the five pattern indices and local 500 mb height (heavy lines), superimposed on wintertime mean 500 mb height contours (lighter lines), contour interval 120 m. Regions of strong correlation are labeled in terms of the respective pattern indices with which local 500 mb height shows the strongest correlation, and the sign of that correlation is indicated.
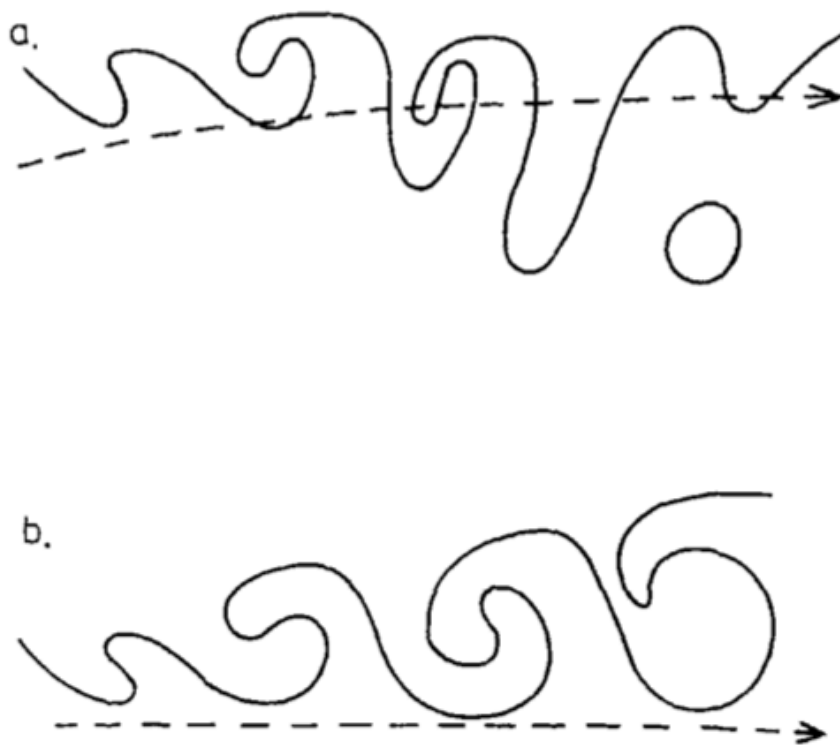
Figure 1.3: From Thorncroft et al. (1993), schematic of a PV contour evolving in an a) LC1/anticyclonic and b) LC2/cyclonic baroclinic lifecycle.
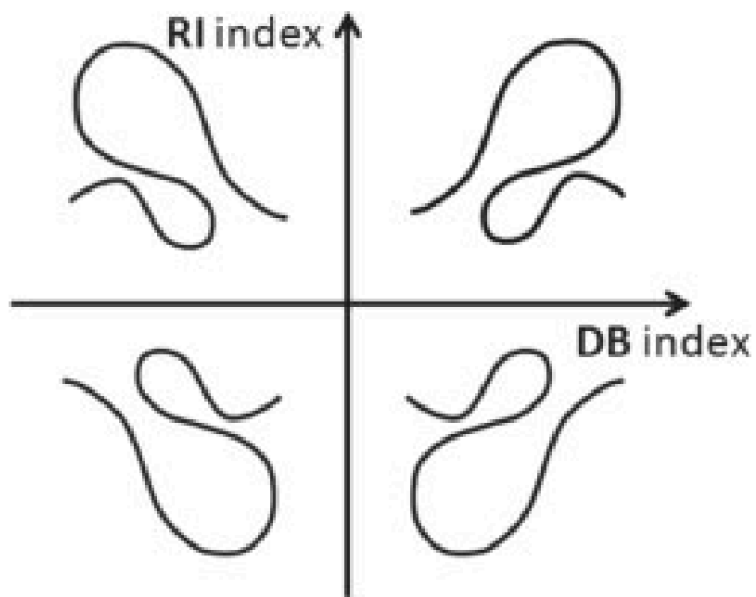
Figure 1.4: Adopted from Masato et al. (2011). Schematic for the Direction of Breaking (DB) – Relative Intensity (RI) plot. DB is on the x-axis while RI is on the y-axis. Positive values of the first index are for anticyclonic wave-breaking and positive values for the second one indicate warm air extrusion dominance. As sketched, a unique wave-breaking type is identified for each quadrant of this plot.
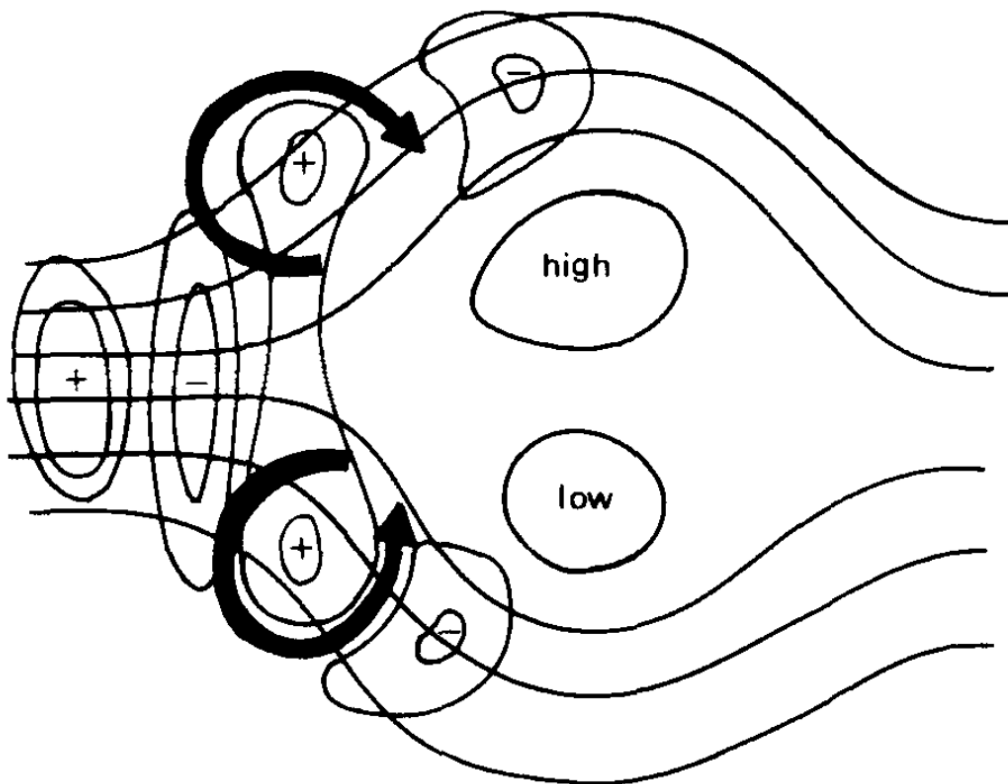
Figure 1.5 Adopted from Shutts (1983): Schematic picture of the production and subsequent deformation of eddies propagating into a split jetstream together with their associated vorticity forcing pattern.
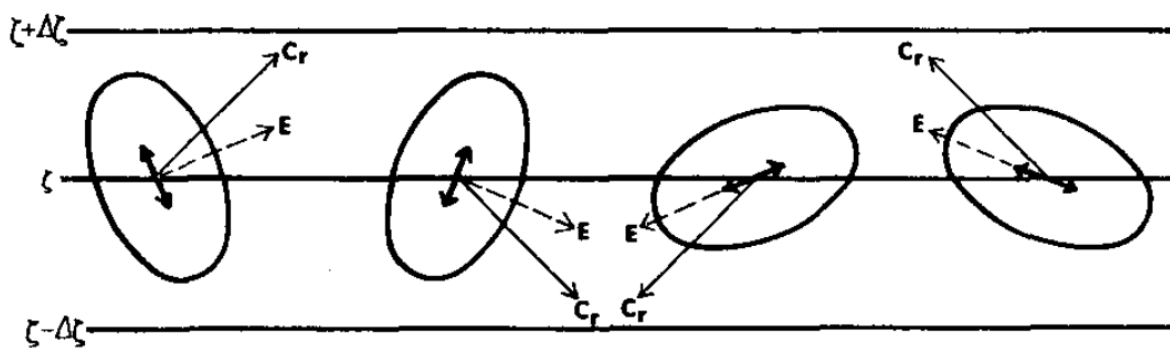
Figure 1.6 Adopted from Hoskins et al. 1983. Illustrating the relative orientations of the eddy anisotropy axis, the E vector and the group velocity relative to the mean flow $c_r = c_g - \bar{v}$. The left-hand par show configurations characteristic of the high frequency transients while those on the right are typical of the low-frequency transients.
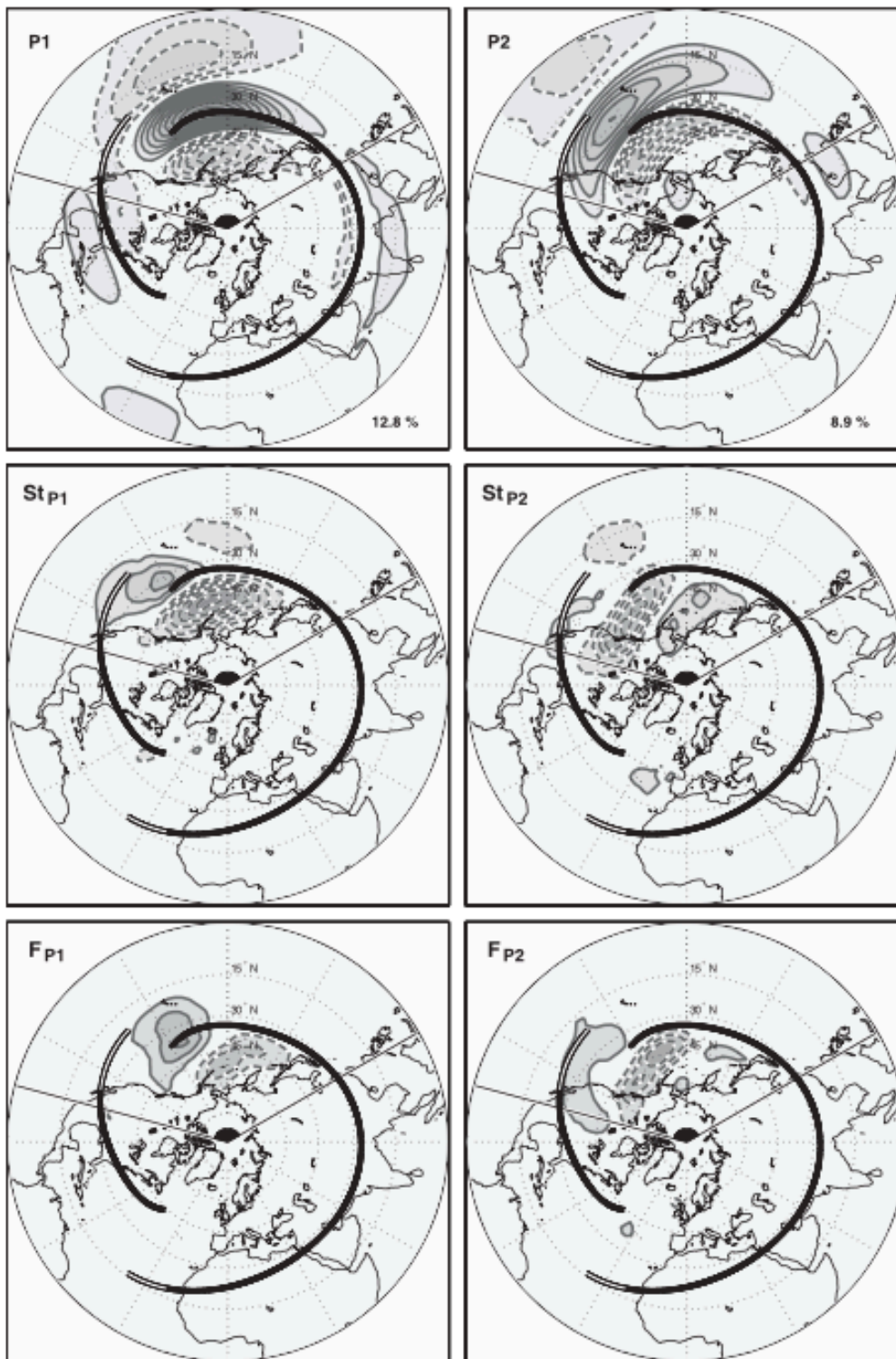
Figure 1.7 Adopted from Athanasiadis et al. 2010. Regressions onto standardized Pacific PC1 and PC2 for (top) U250 (contour interval = 2 m s^{-1}), center v'v' at 250 hPa (contour interval 15 m^2 s^{-2}), and (bottom) $\nabla \cdot E$ (contour interval = 1 X 10^{-5} m s^{-2}).
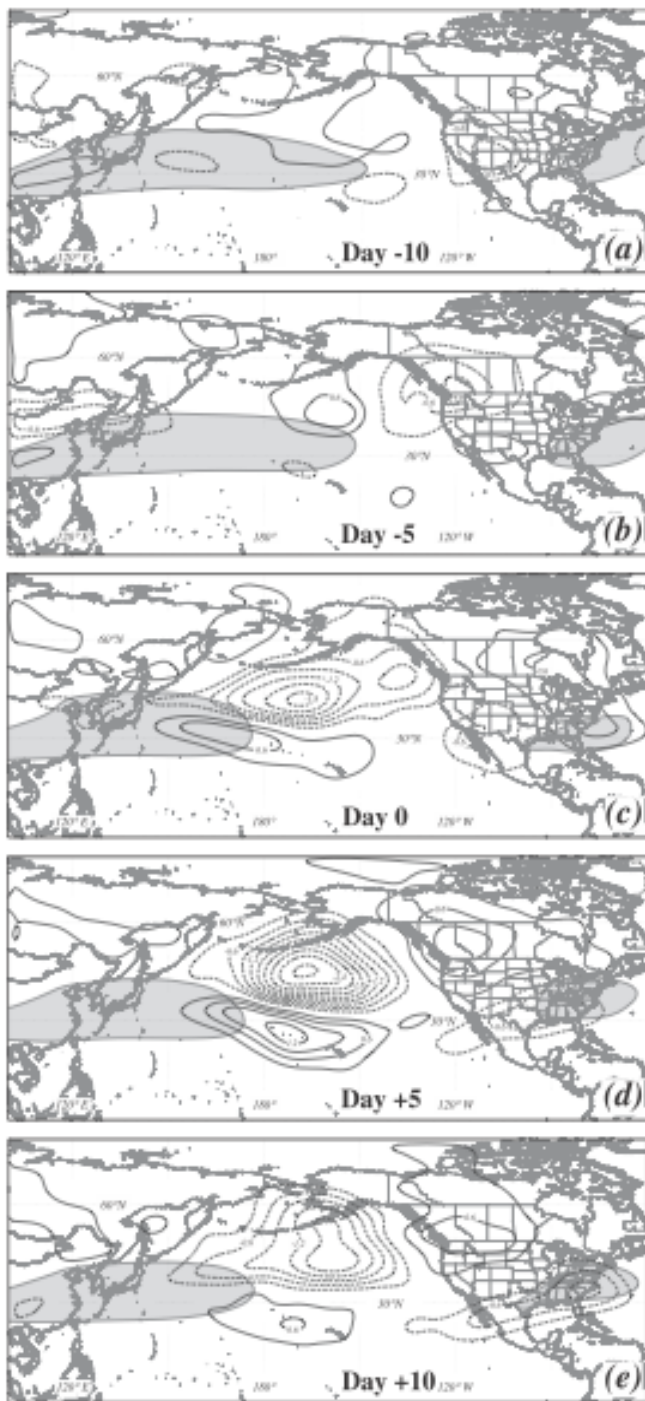
Figure 1.8: Adopted from Jaffe et al. (2011). Composite 200-250-hPa Ertel Potential Vorticity anomalies associated with a jet retraction event at days (a) -10, (b) -5, (c) 0, (d) +5, and (e) +10. Solid (dashed) lines indicated positive (negative) perturbation PV, contours every 0.3 PVU (1PVU = 10^{-6} m^2 K kg^{-1} s^{-1}) with the 0 line removed. Grey shading represents the 40 m s^{-1} isotach of the composite 250-hPa zonal wind.

CHAPTER TWO: SYNOPTIC OVERVIEW AND LIFECYCLE ANALYSIS OF AN EXTREME JET RETRACTION

This chapter examines the initiation of a long-lived retraction that occurred from February-March 2006, and led to an unprecedented period of rainfall, flooding and mudslides in Hawaii (Jayawardena and Chen (2010); Climate Prediction Center). Piecewise tendency diagnosis, first introduced by Nielsen-Gammon and Lefèvre (1996), is applied to the lifecycle of a key feature identified as important for initiating retraction. In Chapter Four the impact of the eddies involved in retraction will be quantified using a novel expanding of piecewise tendency diagnosis. In Chapter 5 the same analysis tools are applied to a retraction observed in February 2017 and will be compared to the 2006 case.

2.1 February 2006 Case

An unusually prolonged retraction of the tropopause-level jet transformed the circulation in the north Pacific for several weeks in mid-February and March 2006 and preceded the development of a long-lived negative Pacific-North American Pattern. The initiation of this jet retraction, associated with a series of anticyclonic/LC1 wave breaking events at high latitude, is investigated through the lens of quasi-geostrophic piecewise tendency analysis. Two key anticyclonic anomalies divert and retract the jet through serial LC1 wave breaking events, mostly confined to the 315-330K isentropic layer and occurring in regions of strong deformation. The rapid development of the first anomaly coincided with the beginning of retraction, and its development is diagnosed in a QG framework in order to quantify contributions to QG height tendencies from various processes. The resultant analysis reveals that growth was induced by a deep PV intrusion that perturbed the jet, while the remainder of the ridge's lifecycle was largely governed by upper-level deformation in the jet exit region. Deformation facilitated both growth

and decay, as the phasing between the ridge and deformation changed. Baroclinic development also contributed to growth, but substantially less than observed by previous studies.

2.2 Data and Methodology

The ensuing analysis employs European Centre for Medium-Range Weather Forecasting (ECMWF) ERA-interim gridded data, accessed at 1°x1° spatial resolution and six hourly temporal resolution, via the online archive (Berrisford et al., 2011). The ERA-Interim data set optimally combines observations (including those from polar orbiting and geostationary satellites) using a four-dimensional variational analysis (4D-Var) scheme, with model output, to create a Reanalysis dataset from 1979 to present. Geopotential was accessed on pressure levels from 1000-50hPa at intervals of 50hPa. The dynamical tropopause was considered in terms of Ertel (1940) potential vorticity on the 2PVU surface ($1PVU = 10^{-6}K\ kg^{-1}m^2s^{-1}$). Potential temperature (θ) on 2PVU is output by ECMWF, found by searching below 98hPa for the 2PVU value, and then evaluating θ at that location (Morgan and Nielsen-Gammon 1998; Berrisford et al., 2011). If the 2PVU value is not located below 98hPa, no value of θ is included.

Standardized height anomalies were computed using ERA-Interim output, by calculating the 1979-2016 average for each six-hour time step. This climatology is then subtracted from the total height field, and the resulting anomalies are standardized. Potential temperature anomalies on 2PVU were calculated in the same manner, and then the four six-hourly anomalies for each day were averaged to produce a daily anomaly. The potential temperature anomalies were not standardized.

The first empirical orthogonal function (EOF) of 250mb zonal wind was computed using National Center for Atmospheric Research (NCAR)/NCEP Reanalysis 2 output at 1°x1° spatial resolution and six-hourly temporal resolution for November-March 1980-2010 (*provided by the*

NOAA/OAR/ESRL PSD). The corresponding principal component time series (PC1) was averaged to a daily mean, and the EOFs were computed after the 30-year daily climatology was removed. The daily-mean Pacific-North American pattern index was accessed from the Climate Prediction Center (CPC) online archive and was calculated using Rotated Principal Component Analysis introduced by Barnston and Livesey (1987). NCEP/NCAR Reanalysis I data was used in the CPC analysis, performed over the period 1950-2014.

2.2.1 Piecewise Tendency Diagnosis

The quasi-geostrophic (QG) system can be used to arrive at a useful relationship between quasigeostrophic potential vorticity (QGPV) and geopotential. QGPV is the sum of the geostrophic relative vorticity, a stretching term, and planetary vorticity (Eqn 2.1). The sum reduces to the three-dimensional Laplacian of geopotential ($\mathcal{L}(\phi)$) and planetary vorticity (Eqn 2.1). Here, $\nabla^2 = (\frac{\partial^2}{\partial x^2}, \frac{\partial^2}{\partial y^2})$, the two-dimensional Laplacian, ϕ represents deviations from the reference atmosphere geopotential (taken to be the U.S. standard atmosphere), f is the coriolis parameter, and σ is the reference atmosphere static stability ($\sigma = -\frac{\alpha}{\theta}\frac{d\theta}{dp}$), where α is specific volume.

$$q = f + \frac{1}{f_o}\nabla^2\phi + f_o\frac{\partial}{\partial p}\left(\frac{1}{\sigma}\frac{\partial\phi}{\partial p}\right) = f + \mathcal{L}(\phi) \quad (2.1)$$

Holopainen and Karola (1991) and Hakim et al. (1996) demonstrated the utility of partitioning the total QGPV field about a basic state and then inverting the full-column perturbation QGPV, q'_{tot}, to retrieve the balanced geopotential height field (2.2a). As $\mathcal{L}$ is a linear operator, q'_{tot} can be split into components that linearly combine to the sum, without any loss of information.   Here q'_{tot} is split into two pieces, one from an upper layer extending from 50-500hPa, (q'_u), and one from a lower layer stretching from 550-1000hPa, (q'_l) (2.2b). The

circulation associated with each piece of the perturbation QGPV extends throughout the troposphere and is distinguishable using this technique.

$$\phi'_{tot} = \mathcal{L}^{-1}(q'_{tot}) \tag{2.2a}$$

$$\phi'_{tot} = \phi'_u + \phi'_l = \mathcal{L}^{-1}(q'_u) + \mathcal{L}^{-1}(q'_l) \tag{2.2b}$$

Additionally, surface potential temperature at the lower boundary is incorporated after Bretherton (1966), who demonstrated that a positive (negative) θ anomaly at the surface can be represented as a positive (negative) QGPV anomaly. Here surface θ effects are incorporated through a Neumann boundary condition of hydrostatic balance (2.3a) as in Nielsen-Gammon and Lefèvre (1996)[1].

$$\frac{\partial \phi}{\partial p} = -\frac{R}{p}\left(\frac{p}{p_o}\right)^{\kappa} \theta \tag{2.3a}$$

   Hakim et al. (1996) introduced a prognostic piecewise QGPV inversion wherein geostrophic QGPV advection is inverted to attain QG height tendencies. Nielsen-Gammon and Lefèvre (1996, hereafter NGL) further partitioned the advection term to quantify the contributions made by specific processes to the total QG height tendencies. They demonstrated the utility of this method, Piecewise Tendency Diagnosis (PTD), through a rigorous investigation of the development of a mobile trough over the United States.

   The mathematical steps taken to arrive at an expression for piecewise QG height tendencies are repeated here. First, the Eulerian time tendency of QGPV reduces to the 3D

---

[1] One further modification is made to retain the consistency between each *q'* field (upper/lower) and the surface θ field used in the inversion. Previous studies balance the surface θ field with only q'_l but there is also a piece of surface θ that is associated with q'_u (a smaller but nonnegligible contribution). In the present case the two surface θ fields are separated, and each QGPV piece is inverted with its corresponding θ field at the lower boundary. The surface θ fields are distinguished by first inverting q'_l with a Dirichlet lower boundary condition, in which the observed geopotential height anomaly is prescribed in the solution. The difference in surface θ calculated using the resultant height field and (3a), and that attained by inverting the *unpartitioned* q'_{tot} field is attributed to q'_u, and has a magnitude of +/- 5K (~25% of the observed 1000mb temperature anomalies).

Laplacian of height tendencies (Eqn 2.4), so that inverting the local QGPV tendency field yields

QG height tendencies (Eqn 2.5). Assuming adiabatic and frictionless flow, QGPV is conserved

following the geostrophic flow, and geostrophic QGPV advection can be substituted for the local

time tendency $\frac{\partial q}{\partial t}$ (right hand side of (Eqn 2.5)). The advection expression can be further

separated into several terms that represent distinct physical processes by partitioning the

advection around a time-mean basic state (denoted by overbars), and separating the anomalous

QGPV and wind fields into upper (q'_u, $\boldsymbol{v}'_{gu}$) and lower (q'_l, $\boldsymbol{v}'_{gl}$) layers as previously described

(Eqn 2.6). The anomalous geostrophic wind fields associated with the upper and lower layers,

$\boldsymbol{v}'_{gu}$ and $\boldsymbol{v}'_{gl}$, are calculated using the geopotential fields attained from inverting q'_u and q'_l,

including their respective surface temperature anomalies (Eqns 2.7a-2.7b).

$$\frac{\partial q}{\partial t} = \frac{1}{f_o}\nabla^2\left(\frac{\partial \phi}{\partial t}\right) + f_o\frac{\partial}{\partial p}\left(\frac{1}{\sigma}\frac{\partial}{\partial p}\left(\frac{\partial \phi}{\partial t}\right)\right) = \mathcal{L}\left(\frac{\partial \phi}{\partial t}\right) \qquad (2.4)$$

$$\frac{\partial \phi}{\partial t} = \mathcal{L}^{-1}\left(\frac{\partial q}{\partial t}\right) = \mathcal{L}^{-1}(-\boldsymbol{v}_g \cdot \nabla q) \qquad (2.5)$$

$$\qquad\qquad A \qquad\qquad\qquad B \qquad\qquad\qquad C$$

$$\frac{\partial \phi'_u}{\partial t} = \mathcal{L}^{-1}\left(-\overline{\boldsymbol{v}}_g \cdot \nabla q'_u\right) \ + \ \mathcal{L}^{-1}\left(-\boldsymbol{v}'_{gu} \cdot \nabla \overline{q}_u\right) \ + \ \mathcal{L}^{-1}\left(-\boldsymbol{v}'_{gl} \cdot \nabla \overline{q}_u\right) \qquad (2.6)$$

$$\qquad\qquad D \qquad\qquad\qquad E$$

$$+\mathcal{L}^{-1}\left(-\boldsymbol{v}'_{gu} \cdot \nabla q'_u\right) \ + \mathcal{L}^{-1}\left(-\boldsymbol{v}'_{gl} \cdot \nabla q'_u\right)$$

$$\boldsymbol{v}'_{gu} = \frac{1}{f_o}\boldsymbol{k} \times \nabla(\mathcal{L}^{-1}(q_u')) \qquad\qquad \boldsymbol{v}'_{gl} = \frac{1}{f_o}\boldsymbol{k} \times \nabla(\mathcal{L}^{-1}(q_l')) \qquad (2.7a, 2.7b)$$

Equation (2.6) shows the terms that contribute to the upper layer (500-50mb) QG height tendencies only; six additional terms of similar form can be determined for the low-level QG height tendency field. Term A represents the advection of upper level perturbation QGPV, q_u', by the background geostrophic winds $\overline{v}_g$. This term includes effects from the advection, deformation, and superposition of anomalies by the background flow (Fig.2.1). The mean wind will always tend to advect disturbances downstream, which leads this term to be high in magnitude and also flank the sides of the anomaly (Fig.2.1a). Development can occur due to asymmetry in the mean state, often manifested as confluence or diffluence (Fig.2.1b). The shape of a PV anomaly situated in an asymmetric background state can be rearranged, changing its attendant circulation. If the feature becomes more isotropic, the circulation will strengthen, and vice versa. The effect from the horizontal and vertical overlapping of QGPV anomalies, which may be brought together by the mean flow to superpose, is also included in Term A (horizontal example, Fig.2.2c). Term A will be referred to as the deformation/superposition term.

Term A has a barotropic component which can be isolated by setting the winds from 1000-50 hPa equal to their value at 300mb, and inverting the resultant advection. Doing so eliminates any advection caused by vertical wind shear that may exist in the background state, effectively prescribing the wind field to be barotropic. Height tendencies that remain after taking the difference between the unpartitioned $\overline{v}_g$ wind field and this barotropic component are attributed to vertical wind shear. Vertical shear can differentially advect anomalies so that they vertically overlap and strengthen the circulation of a particular feature, inducing growth. NGL consider development associated with the remaining height tendencies associated with Term A, after the barotropic component is removed, to be a sign of transient, 'nonmodal growth'. Transient growth occurs when the tilt of anomalies with height changes over time, leading to the

vertical overlapping of anomalies of the same sign ('modal' growth such as in the Eady problem involves a fixed tilt with height over time).

Term B represents the advection of upper level background QGPV, $\overline{q}_u$, by the circulation associated with upper level QGPV anomalies, $\boldsymbol{v}'_{gu}$. This term can be important at the leading edge of a wave packet, where individual waves have different amplitudes, leading to asymmetric $\overline{q}_u$ advection such that the waves at the front of the packet grow due to the effect of higher-amplitude anomalies upstream (Fig. 2.2). NGL found that this term contributed to the early stages of development of an upper-level trough in their case, and interpreted this development as resulting from Rossby wave energy propagating into the area from upstream, at the leading edge of a wave packet. By virtue of these allusions to downstream development or group velocity effects, we refer to this term as the downstream development term, following NGL.

Term C represents the effect of low-level perturbation QGPV, q_l', and its associated tropospheric- deep circulation, on $\overline{q}_u$. Given favorable phasing (ie, westward tilt with height) between upper- and lower-layer anomalies, the circulation associated with a low-level feature (such as a surface cyclone) can advect $\overline{q}_u$ and amplify a disturbance in the upper troposphere. Simultaneously, the circulation associated with the upper-level feature amplifies the lower-level one, and both features develop. Accordingly, this term is commonly interpreted as including effects from baroclinic development. Terms D and E represent nonlinear interactions between the upper and lower-level anomalous geostrophic circulations and QGPV features, and depend heavily upon the geometry of the flow field. These two terms involve the anomalous circulation ($\boldsymbol{v}'_{gu}$ or $\boldsymbol{v}'_{gl}$) rearranging q_u', and are considered vortex-vortex interaction terms.

Overrelaxation techniques are employed to solve for the tendencies associated with each term, which can be linearly combined to arrive at the overall piecewise QG tendency. Finally, to confirm that the QG height tendency components are representing the 'observed' development of ϕ_u', the height tendency values from the sum of all piecewise terms (2.6) are compared against the centered finite-differenced approximation to $\frac{\partial \phi_u'}{\partial t}$ using the ϕ_u' field (2.8), after all fields were smoothed with a 25-point smoother.

$$QG_{obs} = \frac{\phi_u'(t+1) - \phi_u'(t-1)}{2\Delta t} \qquad\qquad (2.8)$$

PTD is applied to an important feature associated with the initiation of an extreme jet retraction that began in mid-February 2006. The basic/mean/background state is defined as the five-day time mean from 11-15 February 2006, the period just prior to retraction onset. After an overview of the case is presented in Section 2.3, results from PTD are shown in Section 2.4.

2.3 Synoptic Overview

The north Pacific jet retraction that began in mid-February 2006 was related to a period of extreme rainfall over Hawaii that continued throughout March (Table 1 Jaffe et al. 2011; Jayawardena and Chen 2011). The Federal Emergency Management Agency (FEMA) declared the event a natural disaster due to the resultant flooding, mudslides and damages (FEMA Case #1640). The rapid onset of the precipitation broke a dry spell over Hawaii that had been associated with an extended jet (Climate Prediction Center). A synoptic overview of that initiation of this event is given in terms of tropopause maps and Hovmöller diagrams.

2.3.1 Tropopause Maps

Consideration of potential temperature on the 2 PVU surface, the dynamical tropopause, presents a succinct overview of the upper-tropospheric dynamical evolution (Morgan and Nielsen-Gammon 1998) and forms the basis of the analysis of the five days leading up to

retraction (Figs. 2.3-2.5). A positive θ anomaly on the 2PVU surface represents an anticyclonic anomaly, while a negative θ anomaly signifies anomalous cyclonic flow. Figure 2.3 shows the 1979-2016 February mean, with three θ contours highlighted. The strong west Pacific jet stream is evident where the meridional θ gradient is strongest, while its exit region is indicated by the diffluence of the θ contours near 160°W. Higher θ values are present in the subtropics, signifying a higher, potentially warmer tropopause. Values of θ decrease moving poleward, in some places over a short distance, indicating where the tropopause slopes dramatically and wind speeds are highest (as in the west Pacific). A lower, potentially colder tropopause is observed at higher latitude.

Daily mean θ anomalies, along with the 315, 330 and 345 K contours, are shown in Figs. 2.4-2.5. Beginning on 11 February, a strong, zonally extended jet reaches 160°W, as implied by the tight and zonally oriented isentropes (Fig.2.4a). Two high-amplitude ridges characterized by positive θ anomalies bookend the jet, one upstream of the jet entrance region labeled B, the other located downstream over northwestern Canada and Alaska. A small, zonally-elongated positive θ anomaly was situated within the jet over southern Japan, labeled A. Feature A develops rapidly into a high-amplitude, large-scale ridge by 15 February (Fig.2.4b-e). Feature A's emergence from the subtropics and movement into the midlatitudes first displaces the jet exit region westward and initiates the weakening of the jet by diverting the 315K contour northward as it grows, weakening the θ gradient on the dynamic tropopause and thus the tropopause-level geostrophic wind.

During this time, B moves southeastward, its shape changing from nearly circular on 11 February to zonally elongated by 13 February as the anomaly is deformed first by confluence in the jet entrance and then by the strong winds in the jet core. Feature A becomes stationary on 15

February and acquires a positive tilt the next day (Fig 2.4f), signifying the beginning of an anticyclonic/LC1 wave break over western North America[2]. Finally, we note that from 14-16 February, B hardly moved, remaining situated within the jet and maintaining its oblong shape. 15 February is the first day on which the Jaffe et al. (2011) jet retraction criteria were met, coinciding with when A was strongest. By 16 February, a trough-like feature had developed in the subtropics northwest of Hawaii at 330-345K.

Figure 2.5 shows the θ evolution from 17-27 February, now skipping every other day for brevity. On 17 February, A overturned, as its base remained in the eastern Pacific with its crest farther downstream over the Canadian archipelago. B was located near the date line and was more isotropic than one day earlier (Fig.2.5a vs Fig.2.4f). Two days later (Fig.2.5b) A and B had merged, as B encroached upon the nearly stationary A. The diffluence associated with the jet exit region was, by this time, located near 160°E, a combined result of the evolution of A and the emergence of B out of the jet core. The subtropical central Pacific remained characterized by a potent, stationary trough on 330-345K throughout the ten-day period. The trough diverted flow southward in the central Pacific, and, in concert with the ridge to its north, enhanced the deformation. The development of the subtropical trough also coincided with the beginning of the rainy period over Hawaii (Jayawardena and Chen 2011; Climate Prediction Center).

Yet another midlatitude anticyclonic anomaly, C, emerged over Japan on 21 February, rapidly developing and overturning two days later (Fig.2.5c-d). The resultant anticyclone remained through 25 February (Fig.2.5e). The attendant split flow, with one branch diverted north of C and the other to the south of the subtropical cyclone, persisted through 27 February, by which time the meridional θ gradient was extremely weak throughout most of the basin.

---

[2] Pelly and Hoskins (2003) showed that wave breaking can be identified when the meridional θ gradient reverses, as seen in the 315K contour on the 16th.

Considering the two-week period overall, the transition of the large-scale circulation from a strong, zonal jet to this split, wavy flow is rather stark.

To summarize, five days prior to retraction the jet was strong and zonal, and was subsequently split due to A and B, which both displaced the 315K contour northward and reduced the meridional tropopause potential temperature gradient on the dynamic tropopause. Both A and B halted in the east-central Pacific in regions of extreme deformation, and were associated with a period of anticyclonic wave breaking on 315K at rather high latitude and low altitude (low θ). To the south of these two anticyclonic features, stationary cyclonic anomalies developed in the subtropics, repeatedly inundating Hawaii with heavy precipitation (not shown). At times, the 330K contour overturned cyclonically northwest of Hawaii while the 315K contour wrapped up anticyclonically to its north (Fig.2.5d).

2.3.2 Hovmöller

A succinct overview of the flow transition associated with the jet retraction is evident in Hovmöller diagrams of 300hPa standardized height anomalies averaged over 20-30°N and 40-50°N (Fig.2.6). In the subtropics (Fig.2.6a), the first half of February is characterized by higher than normal heights from about 130°-180°E, which are then replaced by negative, cyclonic anomalies after 15 February for the remainder of the month and much of March. These low height anomalies are centered near the date line and coincide with the persistent, heavy precipitation over Hawaii. Also of note is how stationary the anomalies are, reflective of the dipole-type block. The midlatitude region (Fig.2.6b) in early February is characterized by many progressive systems as evidenced by cyclonic anomalies moving quickly from west to east over a short period of time. The high-amplitude ridge observed on 11 February at 240°W (Fig. 2.4a) is seen to form and stay in place from 5-11 February, when the jet is extended. Thereafter, 'A'

forms farther upstream at 200°E and similarly ceases to propagate as observed on the tropopause maps. 'B' is also evident, emerging out of the east as a +2 standard deviation anomaly on 11 February, moving eastward while 'A' remains at 200°E.

After the 15 February the formation of C heralds the beginning of a long-lived block that persists until about 5 March. The sprawling and potent anticyclonic anomaly is contemporaneous with cyclonic anomalies in the subtropics, the two forming a dipole-type block, which maintains a retracted jet. It is of interest that the midlatitude anticyclone is far more expansive zonally (120-200°E) than the subtropical cyclonic feature (160-190°E), indicating that the wavelengths of the two stationary features are rather different.

Later in March, the subtropics experienced another period of lower than average heights that remained fixed between 180°-200°E for 15 days. The stationary nature of the anomalies is similar to the earlier period just discussed. Interestingly, the attendant midlatitude behavior differs from the sprawling, blocked anticyclone that occurred in late February-early March. Rather, a series of progressive ridges interspersed with weak troughs occupies the basin during the latter period, with only one instance of quasi-stationary growth around 15-22 March.

2.3.3 EOF1 and the Pacific-North American Pattern

One final perspective is presented to investigate the large-scale flow transition associated with this jet retraction and how it is related to the PNA. Figure 2.7 shows the 250mb zonal wind EOF1 pattern overlaid with the mean jet position (contours Fig. 2.7a) and its corresponding PC1 time series, along with the PNA index for February-March 2006 (Fig. 2.7b). The phase of the jet as expressed by this EOF on a given day can be determined by multiplying the value of PC1 on that day by the pattern in Fig.2.7a. For example, from 10-12 February PC1 is positive, indicating that the jet is extended (confirmed by inspection of Fig. 2.4a). The PNA index is also positive at

this time. Thereafter, PC1 rapidly decreases and reaches values of -3-4σ, reflecting the extreme retraction that occurred. The PNA index also becomes substantially negative, although while PC1 decreases to -3σ before 20 February, the PNA reaches its minimum value one week later, near the end of February (see blue and red stars in Fig.2.7b). Clearly, there is very good correspondence between the transition of the jet from extended to retracted and the development of the negative PNA phase. Modification of the jet therefore seems important for maintenance and amplification of the negative PNA pattern.

2.4 Piecewise Tendency Diagnosis

Since the chain of events that led to the prolonged retraction event was initiated by the growth of Feature A, in this section the development of Feature A is diagnosed from the QG height tendency perspective using PTD.

2.4.1 Evaluation of QG Diagnosis

The 300mb geopotential height anomalies retrieved from inverting the perturbation QGPV, split into two levels using (2.2b), very closely match those calculated directly using ERA-Interim geopotential. The ERA-interim geopotential anomaly will be referred to as ϕ'_a. Figure 2.8 shows time series tracking the contribution to the maximum height value associated with Feature A using the three height fields[3], ϕ'_u, ϕ'_l, and ϕ'_a. The sum of the upper and lower layer contributions adds up to the pink line, ϕ'_{tot}. The extremely close match between the Reanalysis anomaly ϕ'_a (blue dash), and ϕ'_{tot}(pink), confirms the inversion method was successfully implemented, and shows that both fields undergo substantial development into a 300+ meter ridge during the five day period.

---

[3] At 0600, 1200 UTC on 11 February, a distinct height anomaly associated with A has not yet developed as shown in Fig.2.8b. Instead of tracking the position of maximum $\phi_{tot,}$ the grid point of most positive height tendencies, using the QG$_{obs}$ field, in the region from which Feature A emerges, (marked by the A in Figure 2.8b) is used. In this way, it is still possible to diagnose the initial development of Feature A.

From 11-13 February, ϕ_u' accounts for most of the upper level ridge (ϕ_{tot}'), while a substantial contribution on the order of 100m comes from ϕ_l' starting at 12z on the 14th, indicating a low-level ridge has developed and is located directly underneath Feature A at upper levels. To illustrate the evolution of the vertical structure of the circulation near A, Fig. 2.9 shows the 300hPa and 950hPa ϕ_{tot}' fields in black and red, respectively, at 12-hour intervals from 00z 13 February – 00z 15 February. At 00z 13 February, Feature A is amplifying, while a 950hPa anticyclone is beginning to develop to the east of A (labeled H), indicating a characteristic westward tilt with height, suggestive of baroclinic development (Fig. 2.9a). The 300hPa trough and surface cyclone upstream of A also exhibit westward tilt with height. Over the next 36 hours, the 950hPa ridge amplifies and remains rather stationary, while A amplifies but moves eastward (Fig. 2.9b-d). By 12z 14 February, the anticyclones are vertically stacked in the east Pacific, and remain so at 00z 15 February. The implications of the change in the vertical structure of feature A from baroclinic to equivalent barotropic will be discussed in section 2.4b. However, as the ϕ_u' field accounts for the majority of the total 300mb ridge during its development period from 11-13 February, PTD is applied to diagnose the development of the upper-level ridge using (2.6).

Confirmation that the observed height tendencies, approximated by the finite-difference of the ϕ_u' field, (Eqn (2.8)), are reasonably represented by the sum of the QG piecewise terms (Eqn (2.6)) is given in Figure 2.10. When positive (negative) height tendencies are observed, development (decay) of the ridge is anticipated. The two methods of determining height tendencies, Eqn (2.6) and Eqn (2.8) both indicate that there were positive height tendencies over Feature A until 00z 14 February, reflecting the rapid development that was observed in the synoptic overview. Overall there is very good agreement between the observed and QG height

tendencies, although the QG, piecewise sum sometimes overestimates development or decay. The two time series shown in Fig. 2.10 have a correlation of 0.90, and overall the temporal evolution and general magnitude of amplification match quite well. The processes represented by the QG height tendencies therefore account for the majority of the observed growth of Feature A.

2.4.2 Components of QG Height Tendencies

In this section, the terms driving development of Feature A through its initial growth period on the 11th, sustained growth thereafter and subsequent weakening will be investigated. Negative PV advection into the center of Feature A drives height rises and amplification and was achieved via several processes during A's lifecycle. First, southerly flow on the eastern side of a deep, high-PV intrusion advected low background PV northward, producing a positive height anomaly, A, on 11 February. Next, upper-level deformation and superposition, as well as effects from a strong surface cyclone, continued to amplify Feature A through continued negative PV advection, from 12-13 February. Decay of Feature A begins on 14 February and was driven by the deformation term, which began to advect *high* PV into the ridge center, leading to height falls over A.

i. Initial Growth of Feature A due to a PV intrusion

As previously noted, Feature B, a high-amplitude ridge located on the tropopause over Eurasia, reached the poleward side of the jet entrance region on 11 February, and overturned anticyclonically. Figure 2.11a shows the perturbation QGPV at 12z 11 February, with B labeled. Downstream of B, a potent, positively tilted 300hPa trough developed (also evident in Fig.2.4b), and a cross section averaged from 130-140°E shows that the trough was linked to a deep intrusion of anomalous high-PV air into the troposphere to 750hPa (Fig. 2.11b). The high-PV intrusion tilted southward and crossed the upper-level jet axis, and corresponding $\nabla \overline{q}$, which is

shown in Fig. 2.11c. The total QGPV (i.e., sum of fields in Fig. 2.11b and Fig. 2.11c) indicates

the position of the PV intrusion with respect to the strong 300hPa $\nabla \overline{q}$ and the jet. Southerly

flow on the intrusion's eastern side (arrows Fig. 2.11 b, d) was positioned to advect low PV

northward, inducing positive height tendencies and development of A.

Inverting q_l' between 550-750hPa isolates the PV intrusion and its associated height field,

which will be referred to as ϕ_{l_intr}'. Figure 2.12a-b shows the ϕ_{l_intr}' field at 300hPa in contours,

with the background QGPV in the fill, at 12z and 18z 11 February. The negative height anomaly

associated with the PV intrusion was centered over southern Japan, and southerly winds on the

intrusion's eastern side crossed the strong background QGPV gradient, transporting low PV

northward. Inverting the baroclinic development term, $-\mathbf{v}_{gl}' \cdot \nabla \overline{q}_u$, using winds associated *only*

with ϕ_{l_intr}' produces positive height tendencies in the location of negative PV advection in a

broad region to the east of Japan from about 25-55°N. The southern extent of the positive height

tendencies in the subtropics is the location from which Feature A emerges by 18z on the 11th

(Fig. 2.12c-d).

The circulation associated with the upper-level trough that is located upstream of A, and

is linked to the PV intrusion just discussed, also plays a role in A's initial development. Similar

to the mid-tropospheric PV intrusion, on 11 February, southerly flow on the upper-level trough's

eastern side advected low background PV northward in generally the same region as the PV

intrusion (negative height anomaly in Fig. 2.11c-d). The downstream development term $(-\mathbf{v}_{gu}' \cdot$

$\nabla \overline{q}_u)$, captures the height tendencies associated with this upper level influence on the

background QGPV. The time series of height tendencies associated with advection caused by the

upper level trough and PV intrusion, evaluated at Feature A's ϕ_{tot}' maximum, are shown in Fig.

2.13. The baroclinic term (550-750hPa component of Term C in Eqn (2.6)) and the downstream

development term (Term B Eqn (2.6)), both contribute notably to the growth of A on 11 February. The influence of the PV intrusion weakens but remains positive through 12-13 February, while the downstream development term opposes development after 12z 11 February.

ii. Prolonged Growth of Feature A Via Upper-level Deformation & Superposition, and a Surface Cyclone

The upper-level trough and PV intrusion also led to the development of a surface cyclone that amplified in the central Pacific from 12-14 February (see Fig. 2.9, red dashed contours). The surface cyclone was located upstream of A and downstream of the upper-level trough from 00z 13 February – 00z 14 February. The height field attained by inverting q_l' from 1000-800hPa only, ϕ_{l_sfc}' isolates the influence of the lower tropospheric PV/ θ, which extends throughout the troposphere. The cyclone's circulation was strong enough, and positioned in such a way, that southerly flow on its eastern side crossed the strong 300hPa background PV gradient associated with the jet (arrows in Fig. 2.14a). The resultant negative $\overline{q}_u$ advection promoted A's growth in a manner similar to that of the streamer and upper-level trough on the 11 February. Inverting the baroclinic development term $(-\mathbf{v}_{gl}' \cdot \nabla \overline{q}_u)$ using only the circulation due to ϕ_{l_sfc}' yields the height tendency response due to the surface cyclone, showing strong positive height tendencies overlapping with A (Fig. 2.14b). Figure 2.15 shows the temporal evolution of the height tendency contribution to Feature A's growth from the 1000-800hPa component of the baroclinic development term. Height rises from this term show the cyclone contributes strongly and consistently to development of A until 14 February. After this time, the cyclone is diverted northward, away from the strong, 300hPa background PV gradient (Fig. 2.9d-e).

In addition to the surface cyclone, upper-level deformation and superposition strongly contribute to amplification of Feature A from 00z 12- 12z 13 February. The

deformation/superposition term, $-\overline{\mathbf{v}}_g \cdot \nabla q'_u$, captures the effect of the background circulation advecting and reorganizing upper-level QGPV anomalies, including Feature A. High-amplitude deformation is evident in the mean state jet exit region (contours, Fig. 2.16a), leading the background winds to modify the shape of Feature A, in a manner suggested by the schematic in Fig. 2.1b. Figure 2.16a shows the q'_u field at 00z 13 February along with the background geopotential height contours, from which $\overline{\mathbf{v}}_g$ can be discerned. At this time Feature A was situated in between strong, zonal flow on its western side and weak, northward-diverted flow on its eastern side. The position of A in the deformation region is similar to the PV anomaly in the schematic in Fig. 2.1b. The modification of A's shape by the mean flow increased A's isotropy at this time, evidenced by height rises due to the deformation/superposition term overlap with the center of Feature A (Fig. 2.16b). The temporal evolution of the deformation/superposition term shows that deformation amplifies A during its most rapid development period, 12-13 February (Figure 2.17). A further partition of this term shows that the *barotropic* component, which captures the effect of horizontal deformation, most strongly amplifies Feature A. The barotropic component changes sign and promotes A's decay, starting at 18z 13 February, discussed in the next sub-section.

A positive contribution from the *non-modal* component of Term A to intensifying Feature A is observed in Fig. 2.17 from 00z 12 February – 12z 14 February. This indicates that, in addition to horizontal asymmetry in the mean state, vertical shear in the mean state rearranged the three-dimensional q'_u field in a manner conducive to A's development. This component of the deformation/superposition term contributed to A's growth during the period when the vertical tilt between upper- and lower-levels evolved from westward tilted to vertically stacked (Fig. 2.9b-e). The vertical superposition of the upper- and lower-level anticyclones, brought together

by the vertical shear in $\overline{\mathbf{v}}_g$, evidently occurred during this period. Once the upper- and lower-level anticyclones became vertically stacked by 12z 14 February, this term no longer promoted development of Feature A (Fig. 2.9d-e).

iii. Decay of Feature A

As Feature A propagates further into the region of deformation in the eastern Pacific, the direct effect of deformation transitions from strengthening to weakening A, as observed in the time series in Fig. 2.17. Feature A, and the trough upstream of A, propagate eastward with time, and positive q'_u advection associated with the upstream trough strengthens and encroaches on Feature A. By 00z 14 February, the background geostrophic wind reorganizes q'_u such that A becomes *less* isotropic and its circulation is attenuated (Fig. 2.18a). Simultaneously, there is strong *positive q'_u* advection on A's upstream side, associated with the upstream trough. The associated positive q'_u advection by $\overline{\mathbf{v}}_g$ partially overlaps with the center of Feature A, inducing height falls and weakening A on the 14th, evident in Fig. 2.18b.

iv. PTD Summary

The cumulative effect of all processes that contribute to the QG height tendencies associated with Feature A is summarized in Fig. 2.19, which shows time series of all components in (2.6). First an upper-level trough and its deep PV intrusion initiated development and created a distinct positive height anomaly through negative $\overline{q}_u$ advection on its eastern edge (dark blue line). Thereafter, effects from tropopause-level deformation, vertical shear, and a strong surface cyclone cause continued and intense amplification by importing low-PV into Feature A (green, light blue lines, respectively). Overall a lifecycle emerges wherein downstream development associated with the leading edge of a wave packet, including a tilted, deep, small-scale PV intrusion, initiates growth and creates a positive height anomaly in the subtropics on the

equatorward side of the jet. Thereafter, effects from a deformed tropopause and a strong surface cyclone drive development, including a contribution to growth related to vertical shear in the mean state. Feature A propagates northeastward along $\overline{\nabla q}_u$ as it amplifies, splitting the jet as it propagates, evident in Fig. 2.4c-d. Decay of A is driven by deformation as well, which begins to weaken the q'_u anomaly associated with Feature A as the positive PV anomaly upstream of A becomes closer in proximity to A, and the associated height falls led to a weaker anticyclonic anomaly.

2.5 Discussion and Conclusions

This study investigated an extreme jet retraction in the North Pacific that transformed the circulation in this basin from one characterized by a progressive storm track and a strong zonal jet, to a split, blocked flow in mid-February and March 2006. Retraction onset preceded the development of a long-lived negative PNA pattern. The initiation of this jet retraction is associated with the lifecycles of two key anomalies, A and B, that divert and retract the jet through serial LC1 wavebreaking events, mostly confined between 315-330K and occurring in regions of strong deformation. The lifecycle of the first wave to break anticyclonically is diagnosed within a QG piecewise tendency framework, and confirms the physical connections between jet variability, Rossby wave breaking, and the PNA teleconnection pattern revealed in prior studies.

NGL found that downstream development contributed to the amplification of an upper-level mobile trough very early on in the trough's lifecycle, when a Rossby wave packet, and its associated energy, propagated into the region from the west. Baroclinic development drove the majority of development of the trough thereafter, while effects from deformation were variable and minimal. Evans and Black (2003) used PTD to diagnose persistent (>7day duration) 500hPa

anticyclonic anomalies in the North Pacific, the closest analogue to Feature A that has been diagnosed with PTD. During the most rapid development period of the anticyclones they identified, 90% of intensification was associated with baroclinic growth, the other 10% with deformation. Downstream development drove decay of anticyclones in this study, similar to results in NGL, and at no point did this term aid in growth of persistent, 500hPa anticyclones.

Similar to the results found by NGL, an upstream trough located poleward of the jet axis promoted the initial development of Feature A, corresponding to a contribution to growth from the downstream development term. In addition to growth linked to the upstream, upper-level trough, an even stronger contribution to amplification from a deep PV intrusion was observed during A's preliminary development. The intrusion tilted southward across the jet axis, producing negative PV advection and height rises on the equatorward side of the jet, where A first emerged. The development of anticyclones equatorward of the jet are most commonly attributed to divergent outflow associated with tropical convection, but here the forcing for height rises is rooted in the midlatitudes.

Another novel result in the case presented here is that deformation exerts a dominant influence on the growth *and* decay of Ridge A, which has not been previously diagnosed in the Pacific region. Additionally, the downstream development opposed the effect of deformation, promoting growth when the ridge decayed, in direct opposition to the results of both NGL and Evans and Black (2003) (Fig. 2.19 dark blue line).

The mean-state deformation is collocated with a weak meridional QGPV gradient (Fig. 2.20), which is proportional to the zonal phase speed (c_x) of a two-dimensional Rossby wave (2.9), where *k* and *l* are the zonal and meridional wave numbers, respectively.

$$c_x - \bar{u} = -\frac{\frac{\partial \bar{q}}{\partial y}}{(k^2 + l^2)} \qquad (2.9)$$

As Feature A propagates into the region of weak $\nabla \overline{q}_u$, $\overline{u}$ and its phase speed decrease rapidly, and A becomes stationary by 15 February. The downstream development term captures the effect of Rossby wave energy propagation, which is also proportional to the meridional gradient of $\overline{q}_u$. As a result the group velocity is weakened as it reaches the weak $\overline{\nabla q}_u$ in the mid-latitude east Pacific. In this case, the change in sign of the downstream development term between 13 and 14 February, coincident with A reaching the region of strong deformation/weak $\nabla \overline{q}_u$, is a sign that energy is blocked from propagating downstream by the deformation region. Time series of the deformation and downstream development terms from 11-15 February are negatively correlated (r = -.77), another suggestion that the two terms are governed by the same characteristic of the environment: the deformation region. This inverse relationship between deformation and downstream development's influence on growth has not been diagnosed by previous studies employing PTD.

Mak and Cai (1989) discussed how the shape and orientation of eddies with respect to axis of contraction of the background flow influences the barotropic energy exchange between eddies and the background state kinetic energy. A positively-tilted trough in a region of cyclonic shear is conducive to trough intensification as energy is extracted from the background. The trough upstream of A on 11 February (see Fig. 2.9b) is in such an environment, suggesting barotropic growth was occurring within the vicinity of A. Indeed, Evans and Black (2003) interpreted growth from the barotropic deformation term in the PTD framework as evidence of barotropic growth, which they found was important for developing cyclones and anticyclones in the Atlantic region. The lifecycle of Feature A, dominated by the deformation term, provides additional evidence for a connection between a positively tilted wave structure, barotropic growth, and finally, a weakened zonal jet.

Shutts (1983) demonstrated how deformation associated with a block led to a vorticity flux forcing on the zonal wind that maintained the block. His Fig.1 shows how eddies approaching the deformation and block are stretched out and weakened within the block themselves, as observed in this case on 14 February. It is shown through PTD that this process can be captured through a change in sign of the deformation and downstream development terms, and the coincidence of deformation both weakening the ridge by stretching it out *and* preventing the downstream propagation of Rossby wave energy.

Returning to consideration of the composite flow evolution during jet retractions (Fig.1.8), many previously elusive features can now be placed in an emerging dynamical context. An extended jet accompanied by a high-amplitude ridge, whose meridional extent exceeds is zonal extent, in the exit region sets up an environment conducive to initiating a retraction by forming a region of strong deformation. The negative PV anomaly on the cyclonic shear side of the jet in the composite, B in this case, encounters the jet entrance region, at which point it initiates a positively-tilted, southeastward-directed wave train, leading to the growth of a ridge, Feature A, in the subtropics. A's subsequent development marks the beginning of the disruption of the zonal jet. Meanwhile, the subtropical waveguide (345K, Figs. 2.4-2.5) is displaced southward and is characterized by a strip of synoptic-scale, cyclonic PV anomalies to the south of the sprawling anticyclone, accounting for the zonally-extended but meridionally confined cyclonic PV anomaly observed in the composite. This subtropical component represents the southern branch of the split flow observed during Rex blocking events, and in this case was related to a period of unprecedented rainfall over Hawaii.
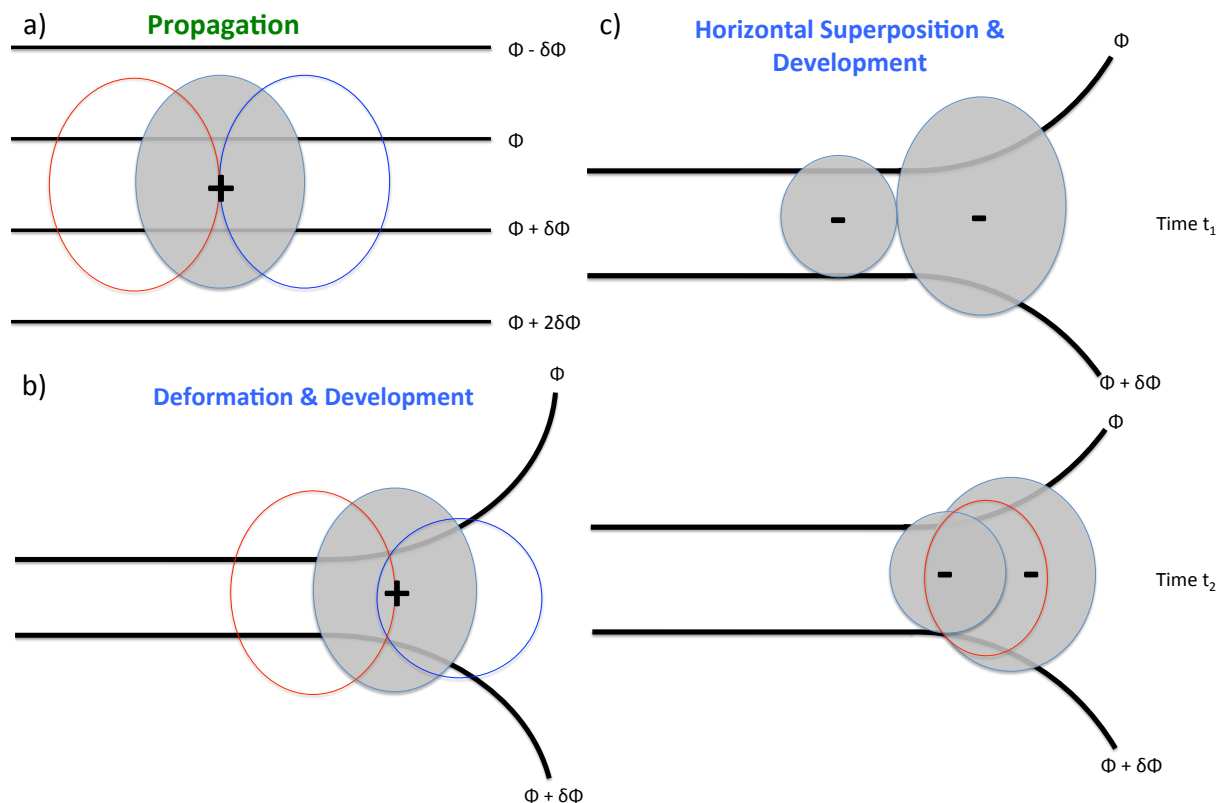
Figure 2.1. Schematics for processes include in Term A. a) Propagation of a theoretical height anomaly situated within a symmetric, geostrophic background flow, with the location of positive (negative) height tendencies shown in red (blue) open circles. b) Development due to diffluence in the background flow. Note the change in the shape of the height tendencies, indicating development due to the overlap of tendencies and the center of the height anomaly. c) Development due to the horizontal superposition of separate anomalies, differentially advected by the background flow, resulting in overlap at t_2.

Downstream Development
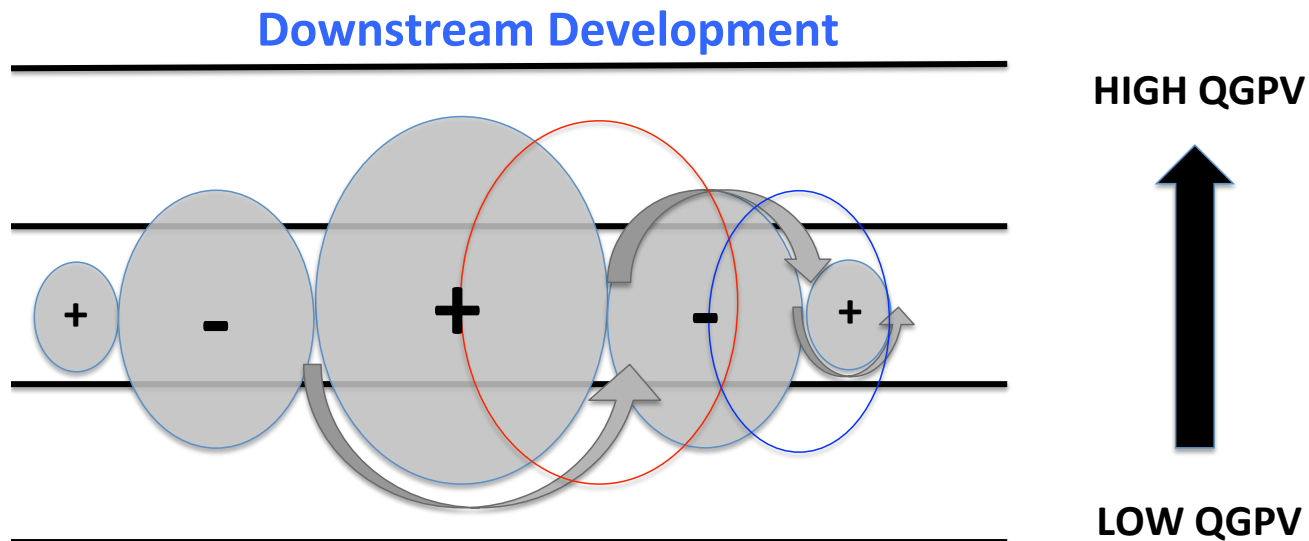
Figure 2.2: Schematic for Term B, downstream development. Anomalies in a wave packet situated within a background QGPV gradient will advect QGPV, with the influence of the largest anomaly in the center of the packet leading to the growth of the smaller feature downstream. The largest red circle represents height tendencies associated with the largest, center anomaly, cyclonic here, which advects low-QGPV into the center of the smaller anticyclonic feature downstream, leading to height rises and development. See text for explanation.
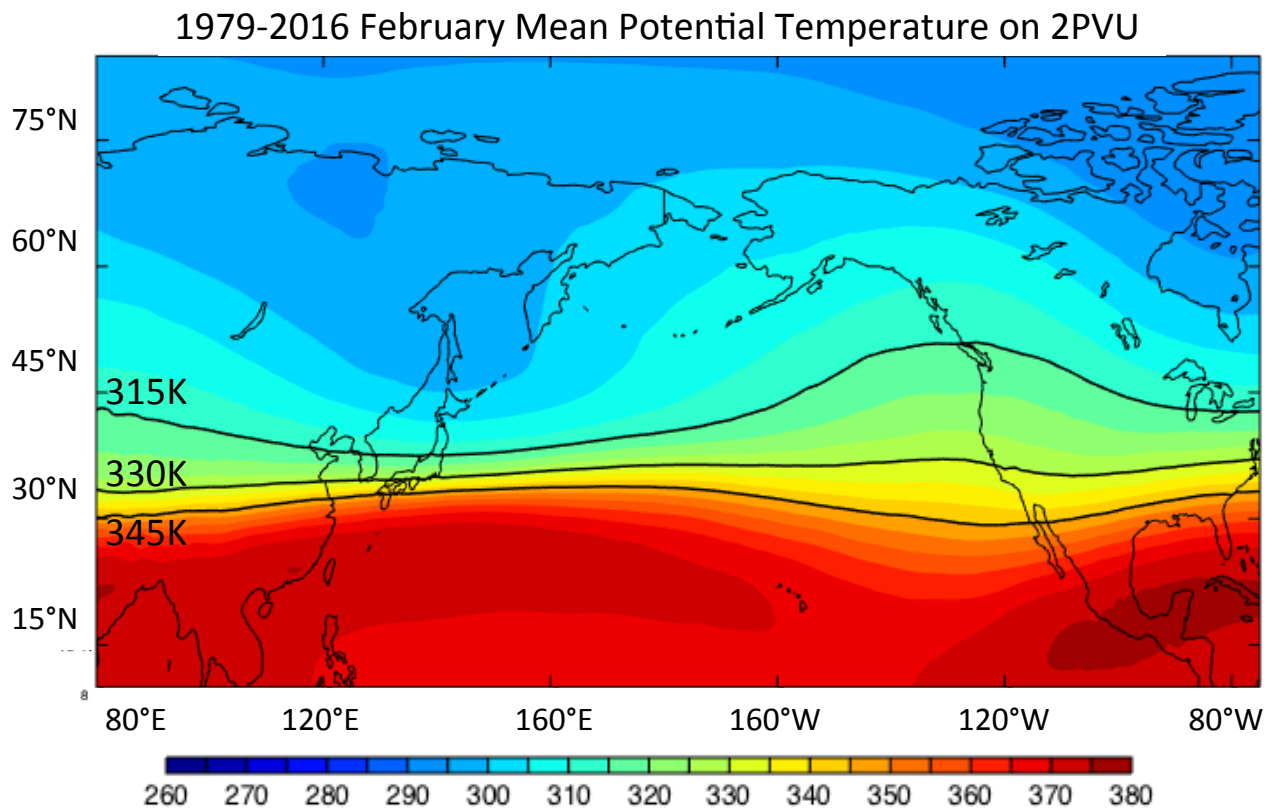
Figure 2.3: 38-year (1979-2016) February mean potential temperature on 2PVU from ERA-Interim. Fill is potential temperature (θ) in units of K contoured according to the accompanying scale. Solid black contours are the individual 315, 330 and 345 K isentropes.
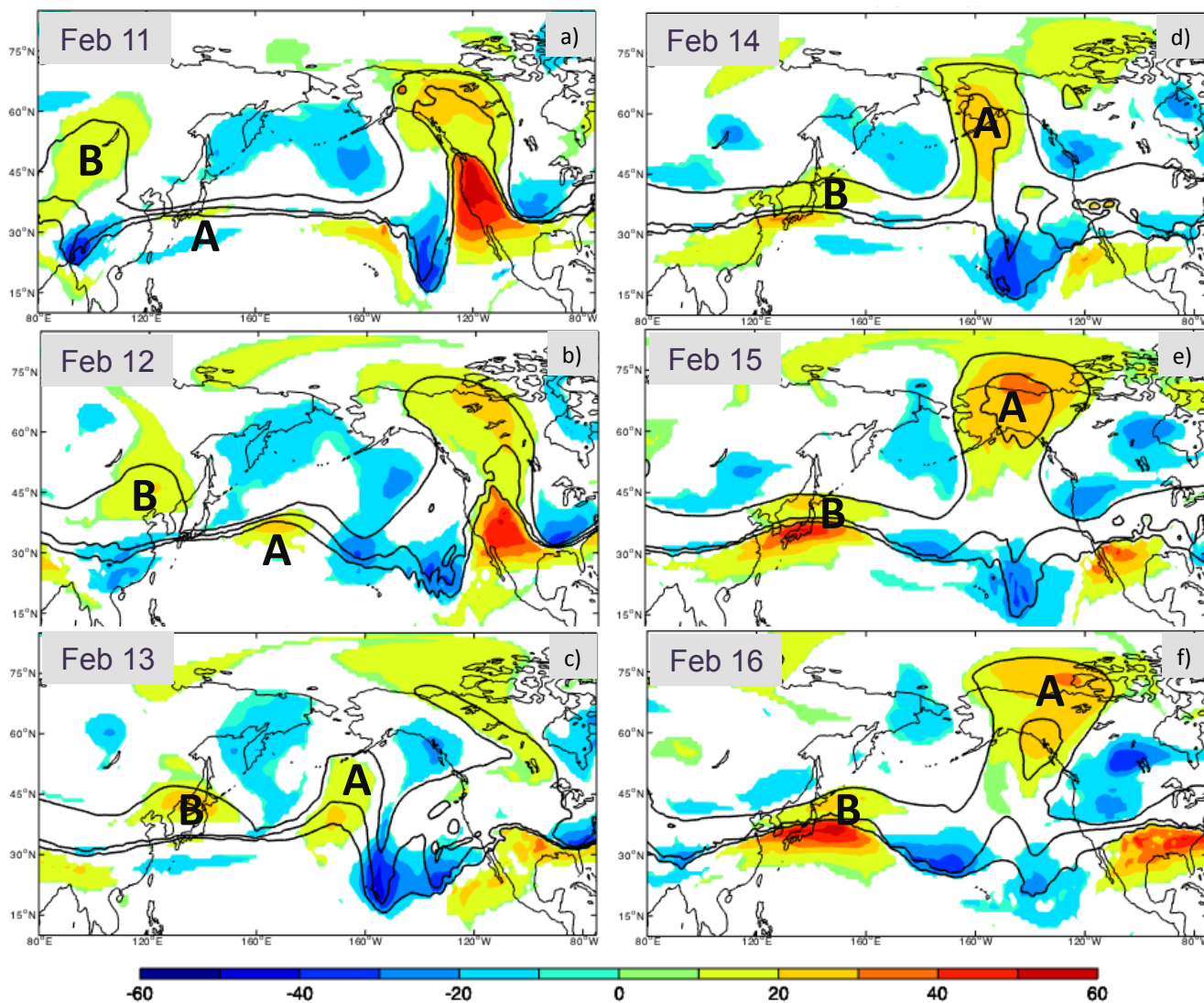
Figure 2.4: Daily mean potential temperature anomalies (fill patterns in units of K contoured according to accompanying scale) on 2PVU for 11-15 February 2006. Solid black lines are the 315, 330 and 345 K isentropes for (a) 11 February, (b) 12 February, (c) 13 February, (d) 14 February, (e) 15 February and (f) 16 February.
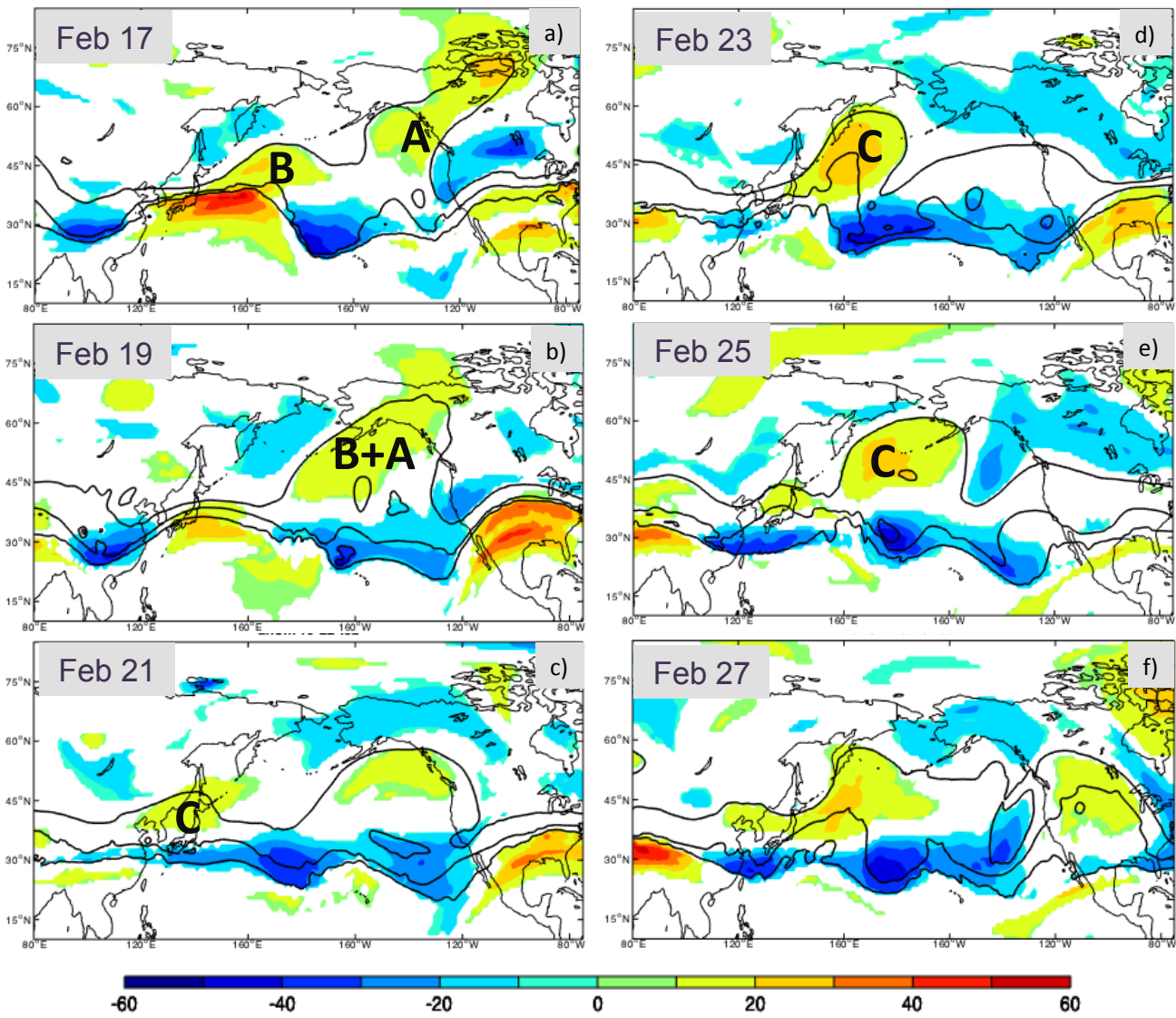
Figure 2.5: Same as Fig. 2.4 but for (a) 17 February, (b) 19 February, (c) 21 February, (d) 23 February, (e) 25 February and (f) 27 February.
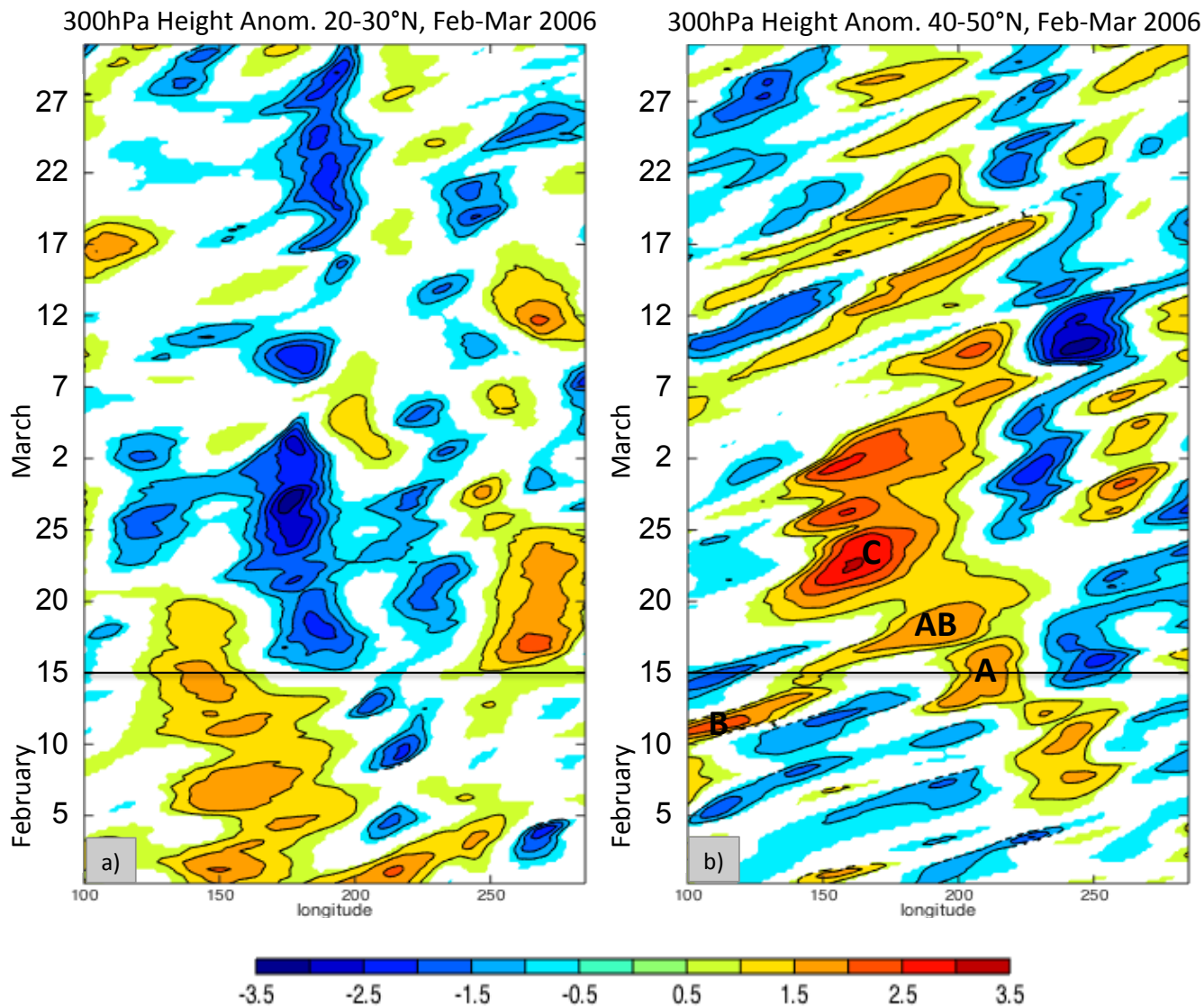
Figure 2.6. Hovmöller of standardized 300mb height anomalies taken with respect to the 1979-2016 climatology for each day, averaged over a) 20°-30°N and b) 40°-50°N for February-March 2006. Black line marks day that retraction is first identified.
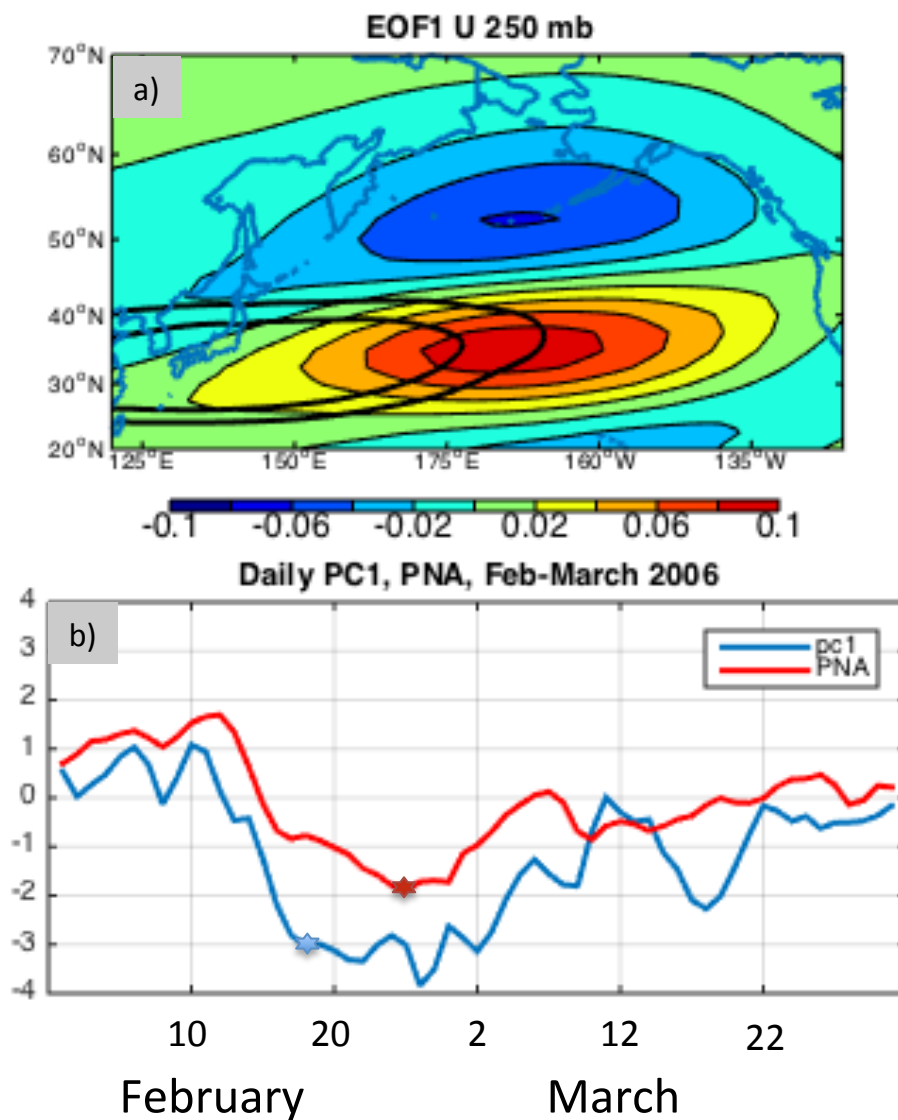
Figure 2.7: a) Dimensionless EOF1 of 250mb zonal wind shading according to accompanying scale, and 40-50 m s^{-1} December-March 2006 mean 250mb zonal isotachs (solid black lines). b) Standardized daily mean PC1 associated with EOF1 pattern (blue solid line) and the standardized daily-mean PNA index (red solid line). The blue and red stars note when PC1 and PNA are near minimum values, with PC1 leading the PNA.
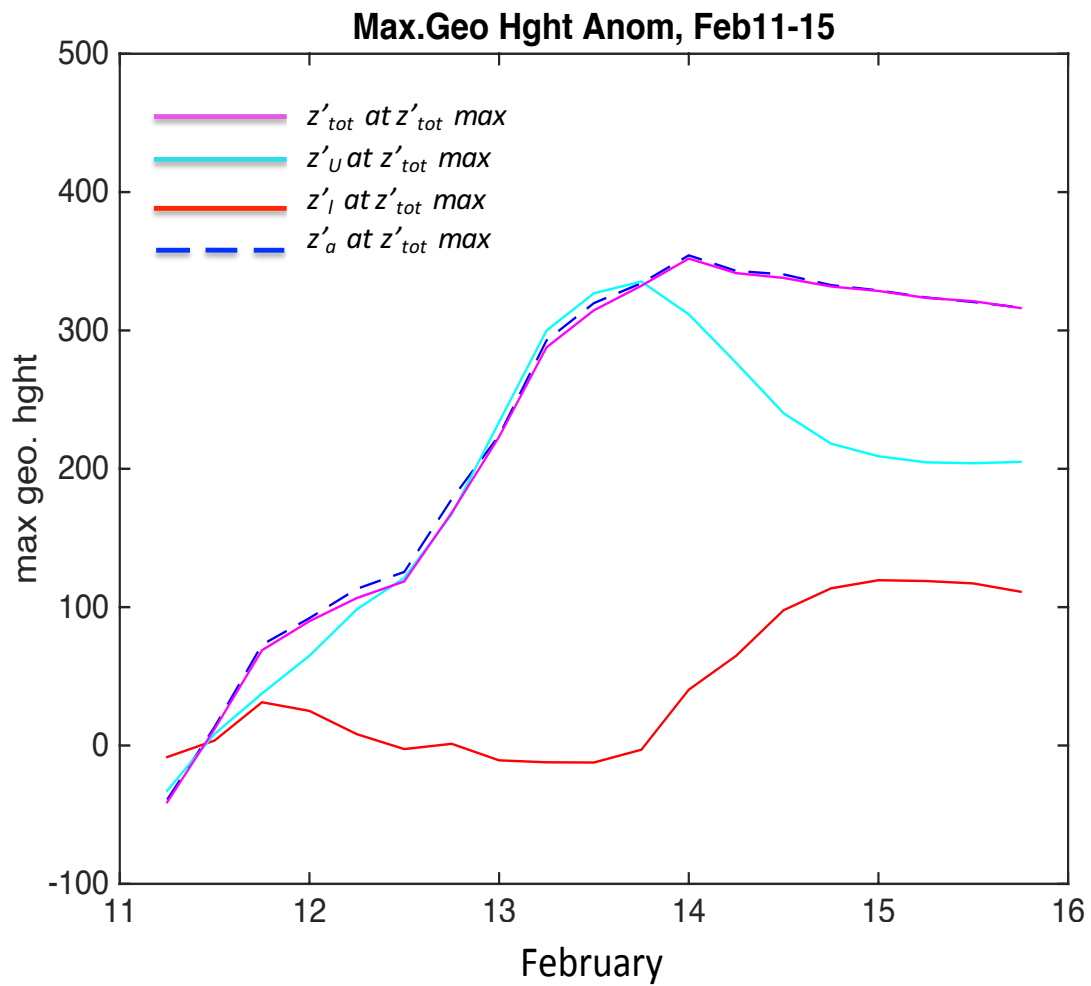
Figure 2.8: Time series of the maximum 300mb geopotential height anomaly (in magenta) associated with Ridge A using the ERA-Interim (blue) and inverted QG height fields (cyan, red, magenta). See text for explanation.
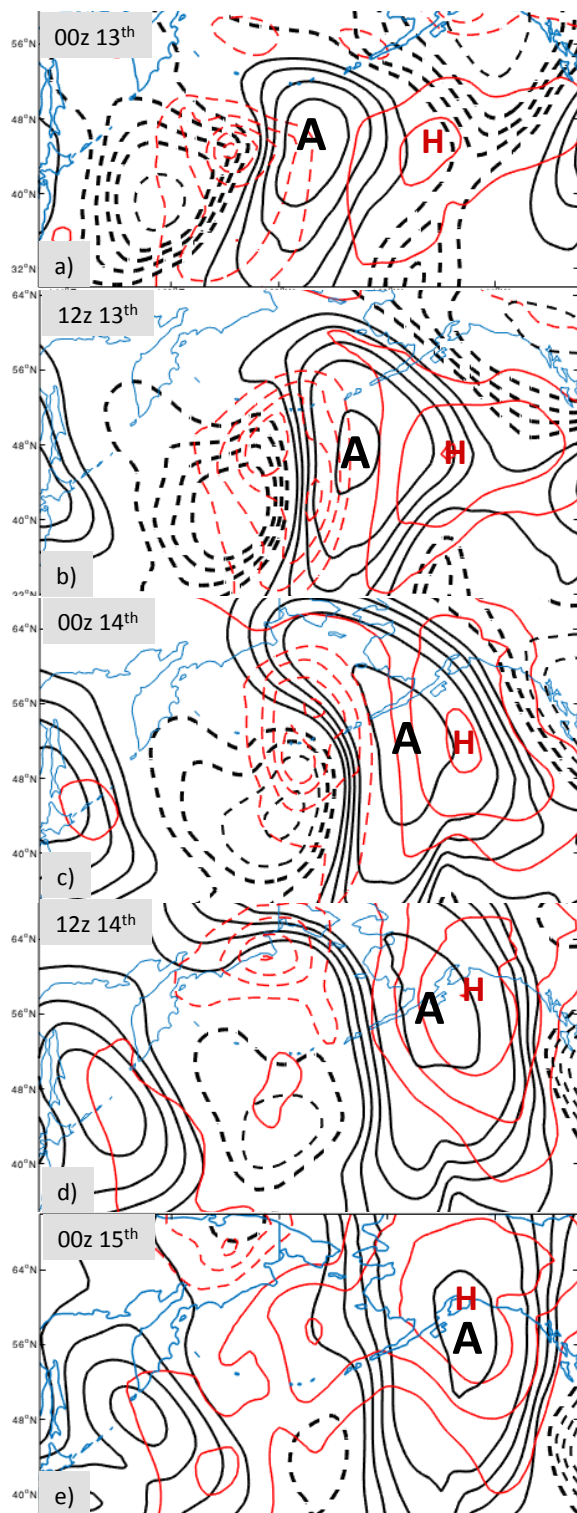
Figure 2.9: Black (red) contours show 300hPa (950hPa) ϕ_{tot}' from a) 00z 13 February – e) 00z 15 February. Height anomalies are labeled in m and contoured every 50 m with positive (negative) values in solid (dashed) lines. The 'A' denotes the location of Feature A at 300hPa, and the red H marks the location of the 950hPa ridge.
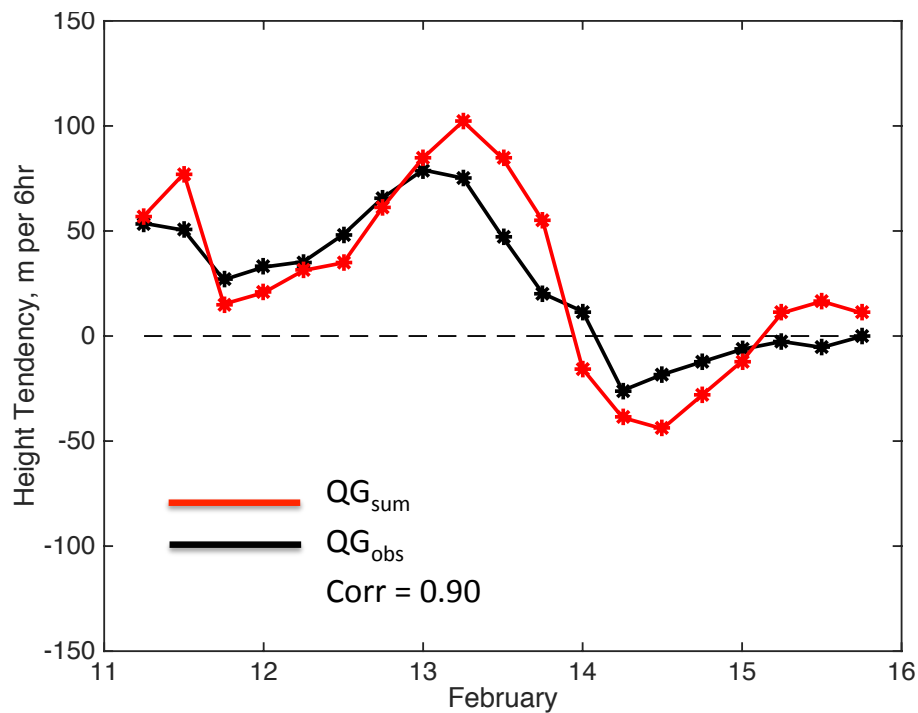
Figure 2.10: Black line is a timeseries of the 'observed' height tendency of ϕ_u', calculated using a centered finite difference calculation to produce the QG$_{obs}$ height tendency (Eqn 2.8) evaluated at the position of the maximum value of the total, inverted QG height anomaly. The red line is the sum of piecewise tendencies (Eqn 2.6) evaluated at the same grid point. The correlation between the two lines is 0.90. Units for height tendencies is m*(6hr)$^{-1}$.
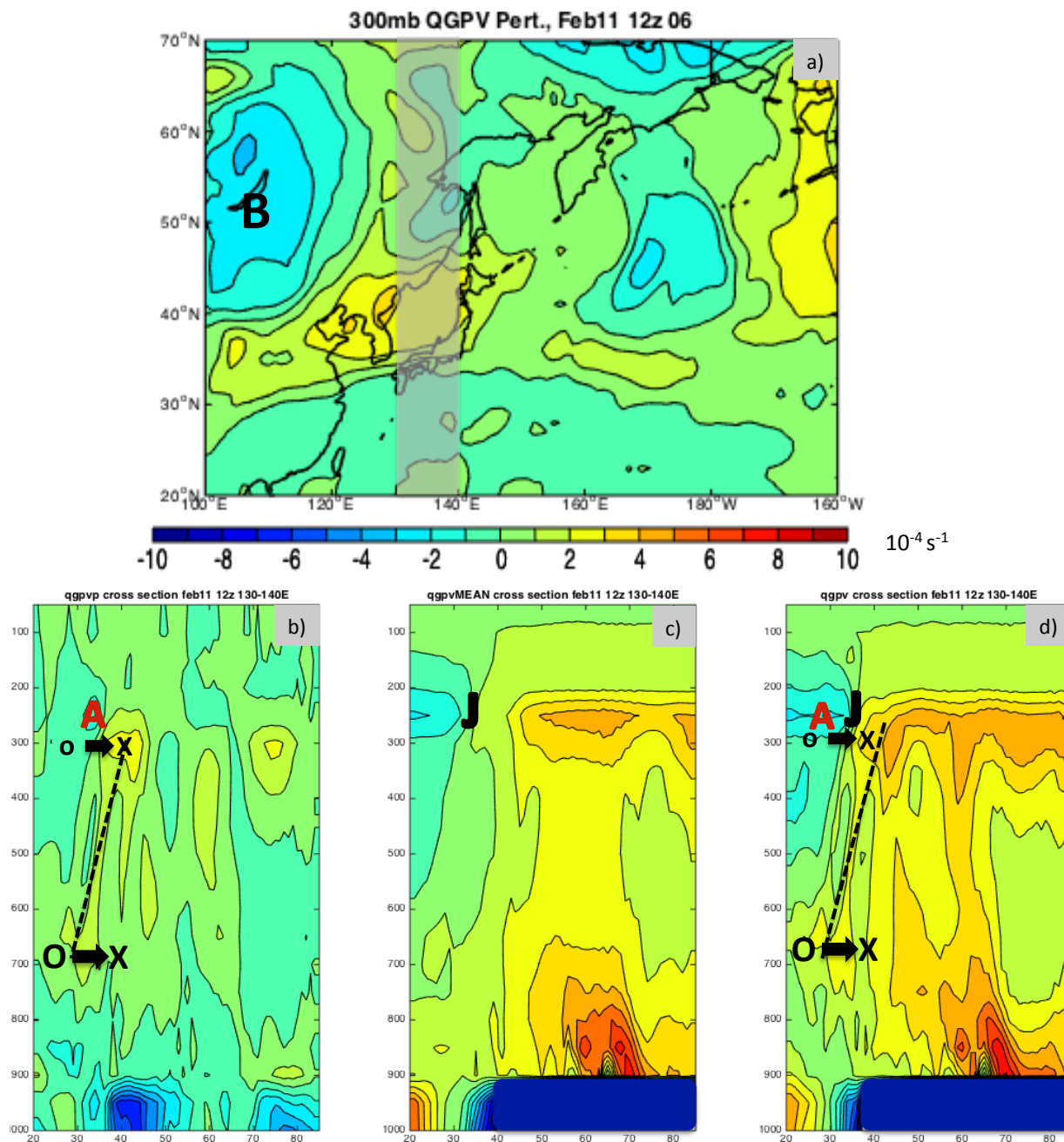
Figure 2.11: a) Perturbation QGPV at 12z 11 February with location of averaged cross section shown by the light gray box. b)-d) Meridional cross sections, averaged over 130-140°E, of b) perturbation QGPV at 12z 11 February, c) 11-15 February average QGPV and d) total QGPV at 12z 11 February. The respective locations of the jet (J) and Ridge A (A) are indicated. The black dashed lines in b) and d) indicate the axis of the anomalous PV intrusion. The arrows, 'o' and 'x's represent the anomalous southerly flow on the eastern edge of the cyclonic PV intrusion, responsible for the strong negative QGPV advection that results. Units are 10^{-4} s^{-1}.
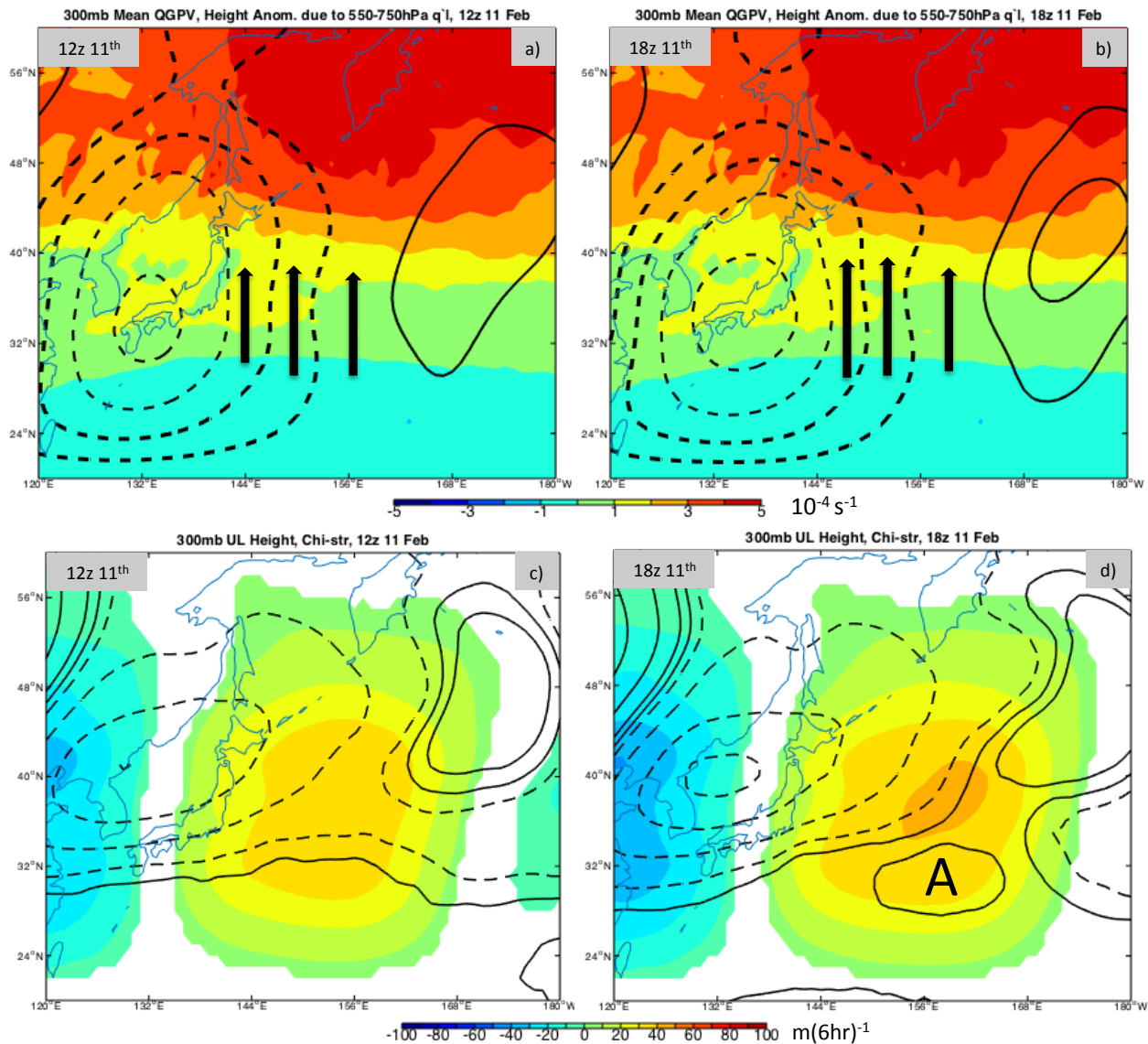
Figure 2.12: a) Color shading is the 11-15 February 2006 mean QGPV field at 300hPa labeled in units of 10^{-4} s^{-1}. Contours are the geopotential height anomalies at 12z 11 February associated with 550-750hPa q' in meters, and contoured at 0, +/- 30, 100, 200 300. Solid (dashed) lines indicate positive (negative) height anomalies, and zero is solid. The arrows demonstrate the southerly flow associated with the anomalous circulation from 550-750hPa. Corresponding negative background PV advection and resulting height rises are shown in c). b) As in (a) but for 18z 11 February. c) The color shading is the height tendency pattern resulting from background PV advection by the height field shown in (a). The contours are the 300hPa geopotential height anomalies associated with q_u', contoured as in (a). d) is the same as c) but at 18z 11 February, with Feature A labelled.
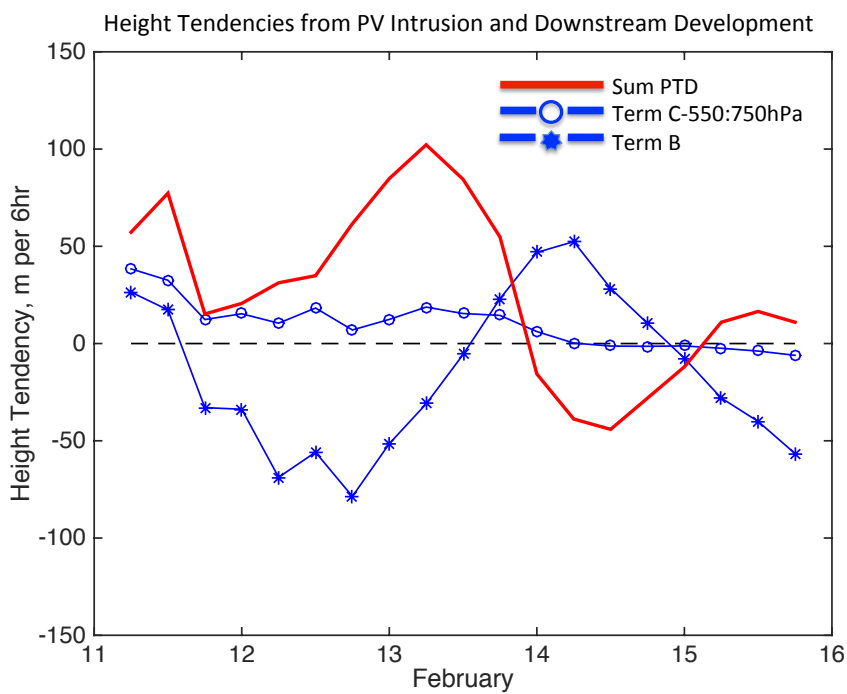
Figure 2.13: Time series of the height tendencies at the position evaluated in Figures 2.8 and 2.10. Term B Eqn (2.6) (blue stars), Term C (resulting from 550-750hPa only; blue circles) and the sum of all terms in Eqn. (2.6) (red). Units are meters per six hours.

Forcing (top) and Associated Height
Tendency Field (bottom) from Surface
Cyclone (Term C)
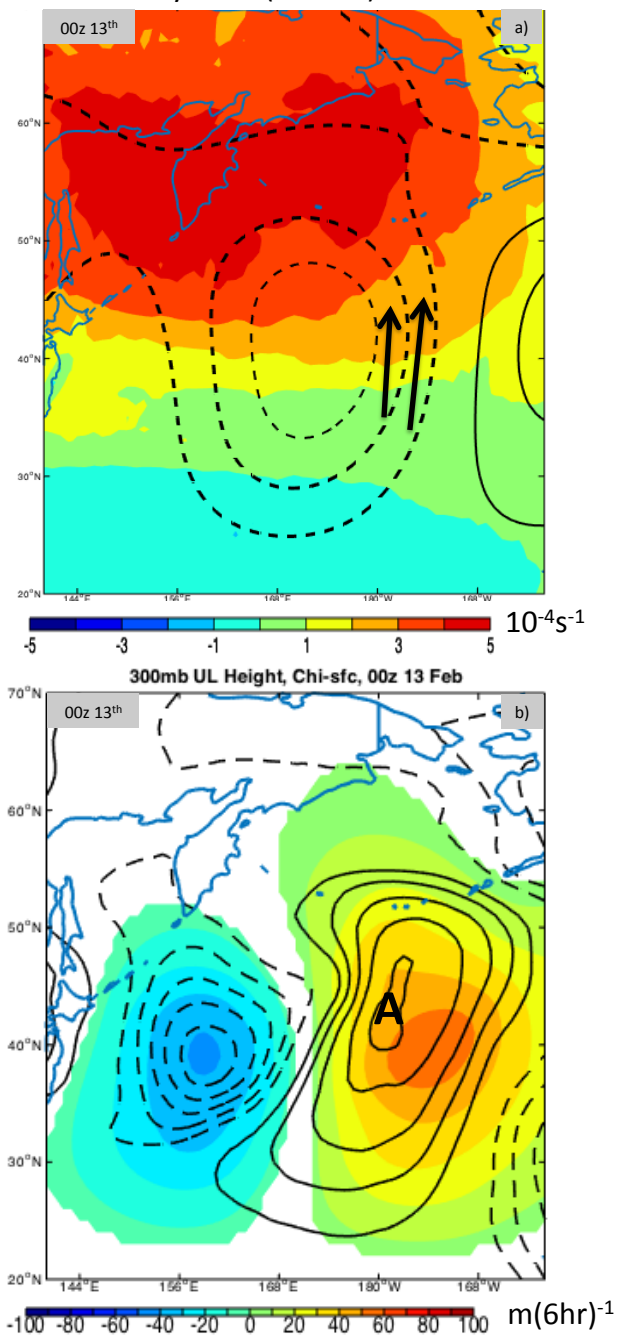
Figure 2.14: a) As in Figure 2.12a except the contours are the height anomalies at 300hPa associated with q_l' from 800-1000hPa, ϕ'_{l_intr}, at 00z 13 February. The arrows mark the southerly flow on the surface cyclone's eastern side. b) The color shading is the height tendency pattern attained from inverting $-\mathbf{v}'_{gl} \cdot \nabla \overline{q}_u$, using the geostrophic wind associated with ϕ'_{l_intr}. Contours show the 300 hPa ϕ'_u field, starting at 50 meters at intervals of 50 meters, solid (dashed) lines indicating positive (negative) values.
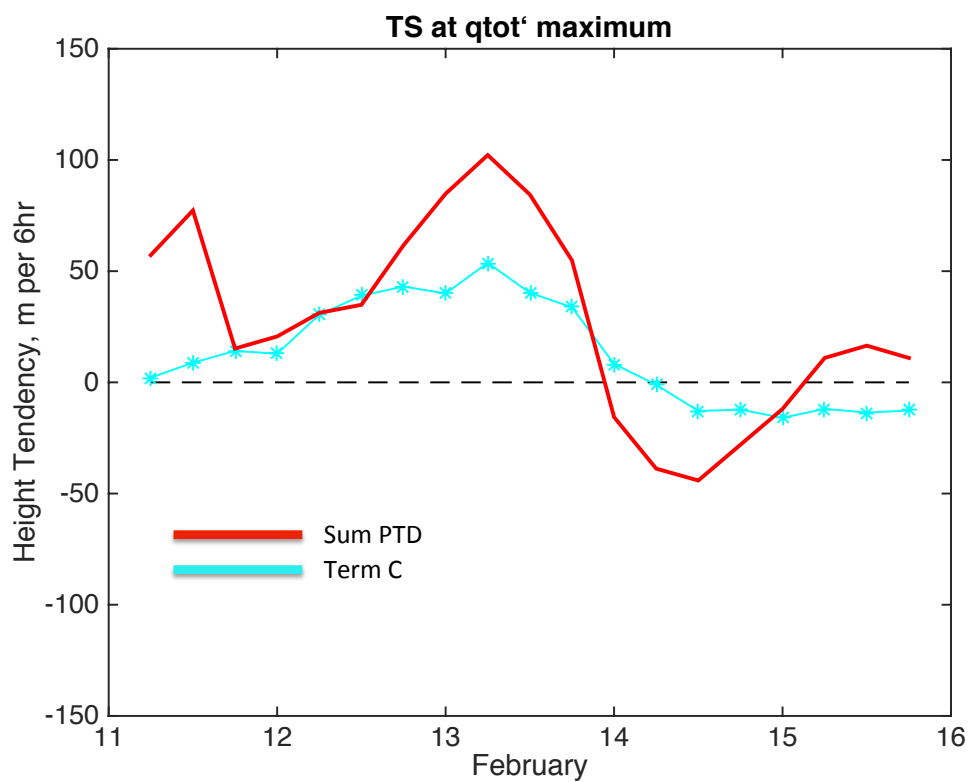
Figure 2.15: As in Fig. 2.13 except for 1000-800hPa component Term C (baroclinic development) in blue.

Forcing (top) and Associated Height Tendencies (bottom) from Deformation/Superposition

Figure 2.16: Barotropic Deformation. a) The color shading shows the 300hPa q_u' field, which is being advected by $\overline{\boldsymbol{v}}_g$, parallel to the geopotential height lines (black contours). The arrows indicate the background geostrophic winds and their ability to advect the q_u' field downstream. The white contours show the height anomaly A, and the contour interval is 50m starting at +/- 100 m, positive values only. b) The color shading shows the height tendency field from inverting Term A in Eqn (2.6), $(-\overline{\mathbf{v}}_g \cdot \nabla q_u')$, at 00z 13 February. Contour interval is 50m starting at +/- 100 m, positive (negative) is solid (dashed) lines, and zero is solid. The A indicates the location of maximum height of Feature A, and positive tendencies overlapping with A indicates that this term is aiding in further development of A.

Figure 2.17: Time series of barotropic and baroclinic contributions to Term A in Eqn (2.6). The sum of the right-hand-side of Eqn (2.6) is shown in red. Units $m*(6hr)^{-1}$.

Forcing (top) and Associated Height Tendencies
(bottom) from Deformation/Superposition
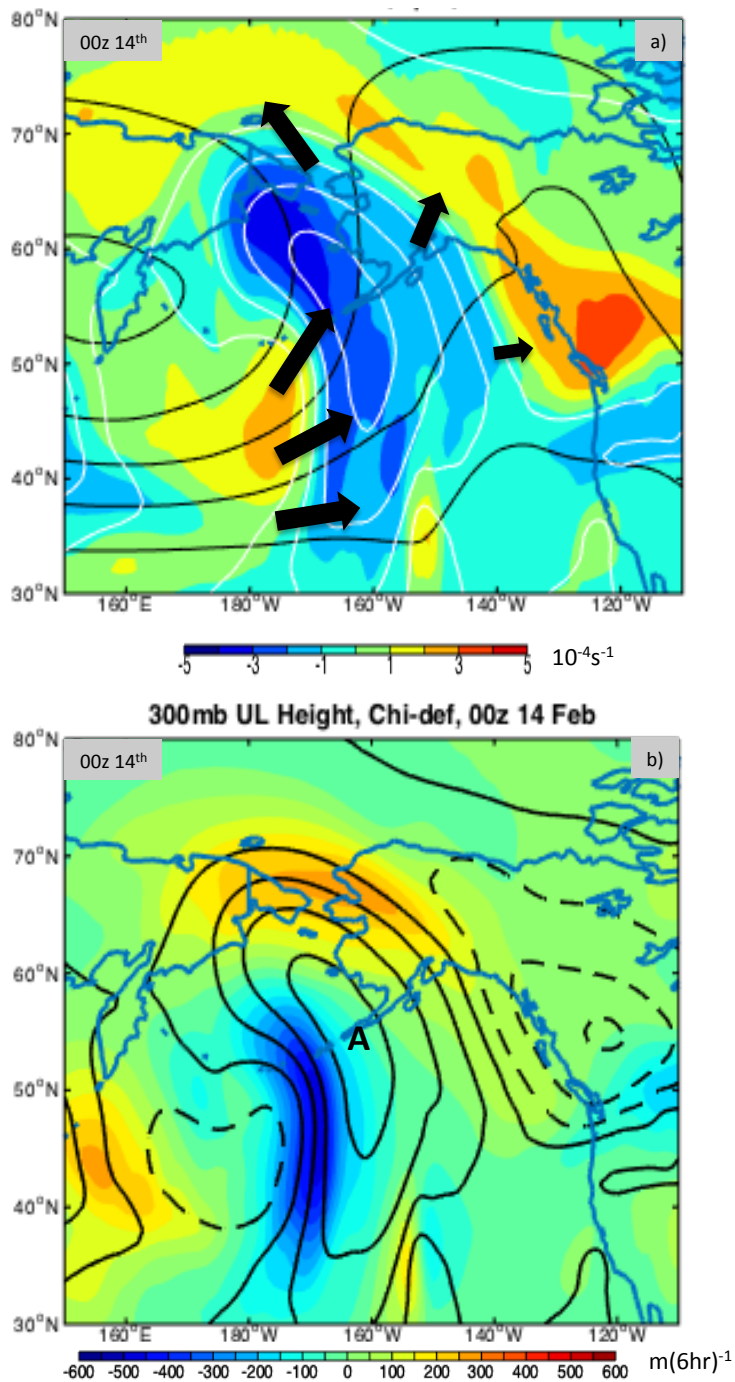
Figure 2.18: As in Figure 2.16, but for 00z on February 14th.
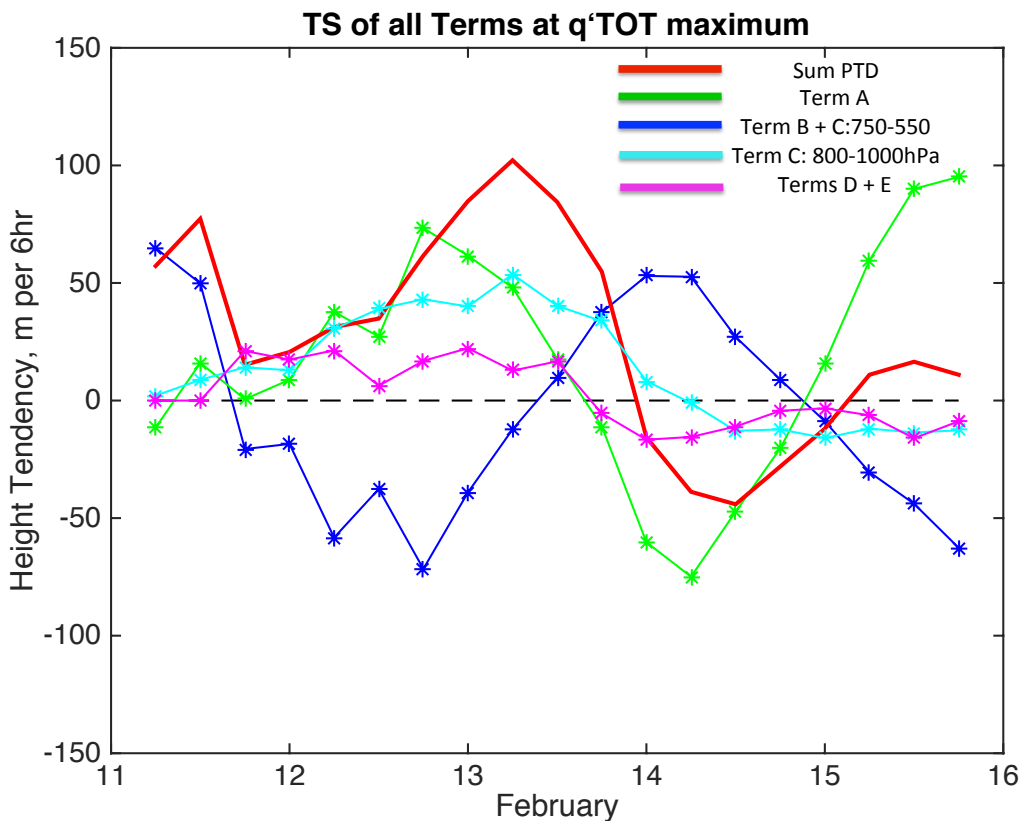
Figure 2.19: Time series of all terms on the right-hand-side of Eqn 2.6: Term A, deformation/superposition, is in green, the sum of Term B (downstream development) and PV intrusion component of Term C (baroclinic development, 750-550hPa) is in dark blue, surface component Term C (baroclinic development, 800-1000hPa) is in light blue, and the sum of Terms D and E (vortex-vortex interactions) is in pink. The red line is the sum of all terms in Eqn 2.6.
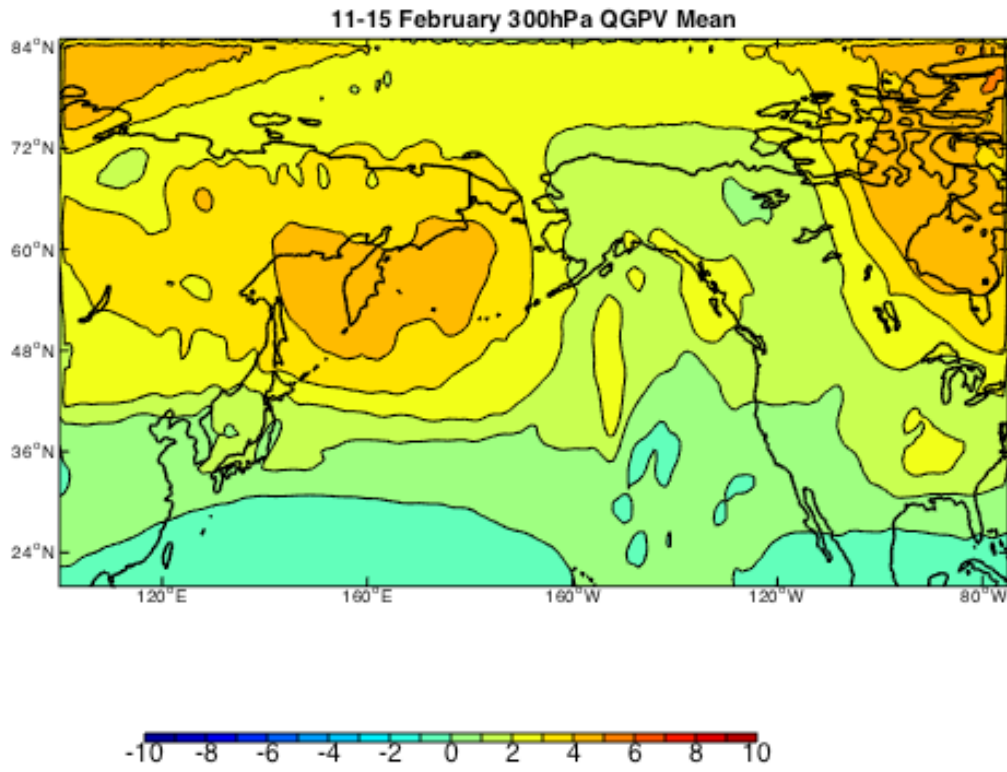
Figure 2.20: 11-15 February mean QGPV at 300hPa, units 10^{-4} s^{-1}.

CHAPTER 3: PIECEWISE GEOSTROPHIC WIND TENDENCY DIAGNOSIS

3.1 Introduction

The zonal extension or retraction of the tropopause-level jet stream is intimately linked to the position and strength of extratropical disturbances like cyclones, blocks, and atmospheric rivers (Berggren et al. 1949; Rex 1953; Martius et al. 2007; Jaffe et al. 2011; Handlos and Martin 2016; Griffin and Martin 2017). In the north Pacific, the zonal pulsing of the jet exit region between 160°E – 160°W dominates 250-300 hPa zonal wind variability (Eichelberger and Hartmann 2007; Athanasiadis 2010; Jaffe et al. 2011; Griffin and Martin 2017). A retracted north Pacific jet is associated with more frequent subtropical cyclogenesis and midlatitude blocking (Otkin and Martin 2004). While periods of retraction and the attendant wavy (and often blocked) flow are well-known forecast challenges, and are associated with notable sensible weather impacts such as flooding and extreme cold (Hoskins and Sardeshmukh 1987; Otkin and Martin 2004; Jayawardena and Chen 2011), a complete understanding of this transition is lacking in the current literature. Various physical mechanisms for blocking onset and blocking maintenance have suggested to be related to deformation, vortex-vortex interactions, diabatic heating and tropical convection, but consensus regarding which of these processes is the most important has not yet been acheived (Shutts (1983); Frederiksen (1983); Yamazaki and Itoh (2013); Pfahl et al. (2015); Henderson et al. (2016)).

Shutts (1983) discussed how transient disturbances lead to the continued advection of low-PV into a midlatitude block, reinforcing the block itself. Andrews and McIntyre (1976) first linked eddy momentum and temperature flux convergence, as represented by the Eliassen-Palm (E-P) flux, to a weakening or strengthening of the zonal mean, zonal wind. Hoskins et al. (1983), Plumb (1985) and Trenberth (1986) all presented formulations that expanded the two-

dimensional E-P flux diagnostics to three dimensions, often referred to as the E-vector, and demonstrated how this diagnostic can be used to study blocking. In particular, the convergence of the three-dimensional E-vector, or related formulations, similarly corresponds to a weakening of the low-frequency zonal wind. Another aspect of E-vector convergence is that it is proportional to the flux convergence of quasi-geostrophic potential vorticity (QGPV), and this represents a forcing for Lagrangian changes in the low-frequency QGPV gradient. This has an important physical consequence as regions of persistent, QGPV flux convergence will weaken the QGPV gradient and, in turn, the zonal wind (see Hoskins et al., 1983 Eqn (38)). Takaya and Nakamura (2001) attained a diagnostic formulation that is applicable for a zonally-varying basic state and can be applied instantaneously, but it relies upon the 'pseudoconservation' of eddy enstrophy and is again, only approximate in its relationship with the acceleration of the wind. In this chapter, we extend QG piecewise tendency diagnosis (PTD, Nielsen-Gammon and Lefèvre 1996), assuming QGPV is conserved, to arrive at a prognostic relationship between various physical processes and their direct influence upon the Eulerian tendency of the geostrophic wind.

Chapter 2 examined a long-lived jet retraction that began in mid-February 2006 and was associated with persistent Hawaiian precipitation and flooding. The synoptic overview of the case showed that anticyclonic (LC1) wave breaking events in the 315-330K isentropic layer facilitated retraction (Features A, B in Figure 3.1). First, Feature A amplified in the central Pacific from 11-15 February (Fig. 3.1a), and proceeded to overturn anticyclonically thereafter (Fig. 3.1b). Feature B moved through the jet core in the 315-330K layer from 13-16 February, and then became superposed with A by 19 February (Fig 3.1c). The lifecycle of A was diagnosed using the PTD methodology introduced by Nielsen-Gammon and Lefèvre (1996). PTD employs QGPV inversion to identify various processes that influence the lifecycle of a

growing synoptic disturbance using QG height tendencies. Applying PTD to Feature A revealed that large-scale deformation in the background state governed the amplification of the ridge, and in concert with baroclinic amplification and transient growth, Feature A was able to grow rapidly in magnitude and size in the central Pacific.

In this chapter, the PTD methodology is expanded to quantify the explicit contributions from the two anticyclonic anomalies – Feature A and Feature B - to retracting the jet. The expanded PTD methodology is outlined in Section 3.2 and its use is applied to the 2006 jet retraction in Section 3.3.   Discussion and conclusions comparing this diagnostic to other studies related to jet stream variability are presented in Section 3.4.

3.2. Data and Methodology

This study employs European Centre for Medium-Range Weather Forecasting (ECMWF) ERA-interim gridded data, accessed at 1°x1° spatial resolution and six hourly temporal resolution, via the online archive (Berrisford et al., 2011). The ERA-Interim data set optimally combines observations (including those from polar orbiting and geostationary satellites) using a four-dimensional variational analysis (4D-Var) scheme, with model output, to create a Reanalysis dataset from 1979 to present. Geopotential was accessed on pressure surfaces from 50-1000hPa at 50hPa intervals and was used for QGPV inversion as well as calculation of the geostrophic wind. 300hPa height anomalies were calculated with respect to the 11-15 February 2006 average at each time step, and were averaged to a daily mean. Height tendencies at each grid point were computed using a 12-hour, centered finite difference approximation (Eqn 3.1), where Δt = 6 hours. Geopotential height tendencies were then averaged to produce a daily mean.

$$\frac{\partial \phi}{\partial t} = \frac{\phi_{(t+1)} - \phi_{(t-1)}}{2\Delta t} \qquad (3.1)$$

The dynamic tropopause was considered in terms of Ertel (1940) potential vorticity on the 2PVU surface (1PVU = 10^{-6}K kg^{-1}m^{2}s^{-1}). Potential temperature (θ) on 2PVU is output by ECMWF, found by searching below 98hPa for the 2PVU value, and then evaluating θ at that location (Berrisford et al., 2011). If the 2PVU value is not located below 98hPa, no value of θ is included. Potential temperature anomalies from the long term mean were computed with respect to the 1979-2016 average at each time step, and then were averaged to a daily mean.

3.2.1 Expanded Piecewise Tendency Diagnosis

The traditional piecewise tendency diagnosis (PTD) methodology was explained and applied in detail in Chapter 2. If one assumes that quasi-geostrophic potential vorticity (Eqn 3.2, QGPV) is conserved following geostrophic motion, QG height tendencies are directly related to geostrophic QGPV advection (Eqn 3.3). Inverting advection will yield the corresponding QG height tendencies. By defining a basic state (overbars) and perturbations around that basic state (primes), and splitting the atmosphere into an upper and lower layer (denoted by subscripts u and l, respectively), advection can be split into several components that represent distinct physical processes (Eqn 3.4). Equation 3.4 includes the terms that contribute to upper-level height tendencies only, and in Chapter 2, Eqn 3.4 was applied to diagnose the lifecycle of a high-amplitude ridge that initiated retraction.

$$q = f + \frac{1}{f_o}\nabla^2\phi + f_o\frac{\partial}{\partial p}\left(\frac{1}{\sigma}\frac{\partial\phi}{\partial p}\right) = f + \mathcal{L}(\phi) \qquad (3.2)$$

$$\frac{\partial\phi}{\partial t} = \mathcal{L}^{-1}\left(\frac{\partial q}{\partial t}\right) = \mathcal{L}^{-1}(-\boldsymbol{v}_g \cdot \nabla q) \qquad (3.3)$$

$$\qquad\qquad\quad A \qquad\qquad\qquad\quad B \qquad\qquad\qquad C$$

$$\frac{\partial\phi'_u}{\partial t} = \mathcal{L}^{-1}\left(-\overline{\boldsymbol{v}}_g \cdot \nabla q'_u\right) + \mathcal{L}^{-1}\left(-\boldsymbol{v}'_{gu} \cdot \nabla\overline{q}_u\right) + \mathcal{L}^{-1}\left(-\boldsymbol{v}'_{gl} \cdot \nabla\overline{q}_u\right) \qquad (3.4)$$

$$\qquad\qquad\qquad\qquad\qquad D \qquad\qquad\qquad\qquad E$$

$$+ \mathcal{L}^{-1}\left(-\boldsymbol{v}'_{gu} \cdot \nabla q'_u\right) \quad + \mathcal{L}^{-1}\left(-\boldsymbol{v}'_{gl} \cdot \nabla q'_u\right)$$

The terms in (3.4) include effects of tropopause-level deformation (Term A), downstream development (Term B), baroclinic amplification (Term C), and nonlinear vortex-vortex interactions (Terms D-E). Tracking the height tendencies at the center of a growing anticyclone provides a way to diagnose which processes contribute to amplification over the anticyclone's lifecycle. If positive height tendencies from a given term overlap with a geopotential height maximum, that term promotes development, while negative height tendencies would promote decay, otherwise propagation is diagnosed.

i. Geostrophic Wind Tendency Equations

While understanding the lifecycle of waves that facilitate retraction is illuminating, the amplification of a given ridge or trough alone does not directly correspond to a specific impact on the zonal wind. Rather, the movement of eddies, as represented by their associated height tendencies, leads to changes in geostrophic wind speed. Taking the local time derivative of the geostrophic wind and rearranging the partial derivatives yields a relationship between the local time tendency of the geostrophic wind and the horizontal gradient of local height tendencies:

$$\frac{\partial u_g}{\partial t} = -\frac{1}{f}\frac{\partial}{\partial y}\left(\left(\frac{\partial \phi}{\partial t}\right)\right) = -\frac{1}{f}\frac{\partial}{\partial y}\left(\mathcal{L}^{-1}\left(\frac{\partial q}{\partial t}\right)\right) \quad (3.5\text{a})$$

$$\frac{\partial v_g}{\partial t} = \frac{1}{f}\frac{\partial}{\partial x}\left(\left(\frac{\partial \phi}{\partial t}\right)\right) = \frac{1}{f}\frac{\partial}{\partial x}\left(\mathcal{L}^{-1}\left(\frac{\partial q}{\partial t}\right)\right) \quad (3.5\text{b})$$

Equation (3.5) reveals that if, in a certain location, the meridional gradient of height tendencies is positive, then the right-hand-side of (3.5a) is negative, and the zonal geostrophic wind will weaken at that location (Fig. 3.2a). If, as in the schematic and the 2006 retraction, a

ridge is located poleward of the mean jet axis, the ridge's movement will weaken the mean

westerly flow. A similar tendency to weaken the zonal wind occurs on the northern branch of a

trough, so a trough located *south* of the jet axis would similarly decelerate the jet.

Assuming QGPV is conserved following the geostrophic flow, geostrophic QGPV

advection can be substituted in for $\frac{\partial q}{\partial t}$ in (3.5), and the same partitioning of advection as done in

traditional PTD can be applied:

$$
\frac{\partial u_g}{\partial t} = -\frac{1}{f}\frac{\partial}{\partial y}\left\{\left(\mathcal{L}^{-1}\left(-\overline{\boldsymbol{v}}_g \cdot \nabla q'_u\right)\right) + \mathcal{L}^{-1}\left(-\boldsymbol{v}'_{gu} \cdot \nabla \overline{q}_u\right) + \mathcal{L}^{-1}\left(-\boldsymbol{v}'_{gl} \cdot \nabla \overline{q}_u\right) + \mathcal{L}^{-1}\left(-\boldsymbol{v}'_{gu} \cdot \nabla q'_u\right) + \mathcal{L}^{-1}\left(-\boldsymbol{v}'_{gl} \cdot \nabla q'_u\right)\right\} \qquad 3.6
$$

Through (3.6) it is shown that the local weakening and strengthening of the geostrophic wind can

be diagnosed in a piecewise manner, similar to how the height tendencies were diagnosed in

traditional PTD. Here the zonal wind component alone is emphasized, as retractions are defined

based upon zonal wind variability, which dominates jet variability in the north Pacific

(Athanasiadis et al. 2009; Griffin and Martin 2017). One may track the changes to the zonal

wind following a certain anomaly, such as Feature A, in a manner similar to that in which the

maximum height anomaly associated with Feature A was tracked and diagnosed. Alternatively,

it is possible to choose one location – for example, the jet exit region, and explore the processes

accelerating the zonal wind in that region through time. Consistent with the Eulerian definition

of jet retractions presented by Jaffe et al. (2011), the latter approach is used to understand how

retraction was initiated in February 2006. Recall that the jet exit region in the central Pacific

coincides with the location of greatest amplitude in the EOF1 pattern of the 300-250hPa zonal

wind (Jaffe et al. 2011 Fig. 4).

An example of the spatial relationship between height anomalies, their height tendencies, and the overall influence on the zonal wind is provided in Figure 3.3. For now, the daily mean height changes and zonal wind changes are considered. Figures 3.3a,c show height anomalies and height tendencies, using anomalies calculated with respect to the 11-15 February time mean, on 11 and 12 February.

From 11-12 February, two regions of positive height tendencies were observed in the north Pacific and were located downstream and partially overlapping with anticyclonic anomalies A and B (labelled). On 11 February Feature A was a small, weak feature, while the region of positive height tendencies downstream of it was somewhat stronger. According to Eqn (3.5a), whenever height tendencies increase with latitude, the zonal wind will decelerate. Indeed, on the southern edge of the positive height tendencies downstream of A, a negative zonal wind tendency on the order of 10-15 $\text{ms}^{-1}(6\text{hr})^{-1}$ was observed from 180-200°W, 30-40°N (Fig.3.3b). This location corresponds to where the zonal wind is tracked to identify retractions (Jaffe et al. 2011) and overlaps with the broad jet exit region, shown by the isotachs. Meanwhile, on 11 February Feature B was located over Eurasia, and its associated positive height tendencies were located downstream and slightly to its south (Fig 3.3a). A region of negative zonal wind tendency was observed on the southern edge of the positive height tendencies associated with B, from 120-140°E, 35-45°N (Fig. 3.3b).

One day later, the jet was more zonally confined as a result of the height tendencies observed downstream of A. At this time A was strengthening and was positively-tilted (Fig. 3.3c). Positive height tendencies downstream of A were more sprawling and stronger in magnitude than on the 11th. However, the deceleration to the south of the height tendencies was unchanged from the prior day, and had also moved eastward following the height tendencies.

Feature B moved slightly eastward from 11-12 February while weakening slightly, while the height tendencies downstream of B strengthened in magnitude and were associated with a stronger region of deceleration than on 11 February. The change in height tendencies reflects the influence of stronger wind speeds within the jet in advecting Feature B more rapidly downstream than one day earlier. In response to the stronger height tendencies, the deceleration associated with B increased, suggesting the jet can be somewhat self-destructive.

By 13 February, the shape of A, and its associated height tendencies, were both elongated in the meridional direction. As a result, the zonal wind deceleration on the southern edge of the positive height tendencies (40°N, 150°W) was *weaker* than in days prior, despite the increased amplitude of Feature A overall. The positive height tendencies downstream of B maintained their strength compared to 12 February, and the region of deceleration remained strong as well, as it moved slowly eastward. On 14 February, a weaker, less organized region of positive height tendencies associated with B produced weak deceleration in the jet exit region (Fig 3.4c-d).

As discussed in Chapter 2, Feature A approached a high-amplitude deformation region in the east Pacific on 14 February, which elongated the ridge meridionally and ultimately led to A's decay. As a result of the inopportune shape of Feature A and its height tendencies, A directly contributed more to retraction as a small, developing height anomaly on 11-12 February than it did as a large-scale, high-amplitude wave a few days later. In contrast, B remained rather isotropic from 11-14 February, coinciding with a more compact region of positive height tendencies, and a correspondingly stronger direct influence on the zonal wind. However, A was associated with strong southerly flow on its western edge on 13-14 February, and was located within the region of the jet exit region. Therefore A did disrupt the zonal jet by simply displacing westerly flow to the north on the ridge's western side (Fig. 3.4a,c).

Overall during this four-day period, the initial retraction was facilitated by the growth of Feature A, and maintained by B, both anticyclonic anomalies forming and propagating on the poleward side of the jet. Considering daily mean or instantaneous deceleration captures the periodic nature of transient disturbances, which leads to periodic, transient changes in the wind. Over the five-day period the jet weakened overall, suggesting that A and B produced a lasting effect on the zonal wind, not just a short-lived, oscillatory influence. As will be shown in the next section, it is possible through PTD to separate the wave-like (and net zero) components of deceleration from the persistent deceleration producing retraction. The individual zonal wind tendency terms in Eqn (3.6) were integrated from 11-15 February to ascertain each term's net effect on the zonal wind. The next section investigates the cumulative influence of A and B on retraction from 11-15 February, using the same PTD results as presented in Chapter 2.

3.3 Results from Applying Piecewise Zonal Wind Tendency Diagnosis

Figure 3.5 shows the total zonal geostrophic wind change from 11-15 February, attained by integrating the instantaneous geostrophic wind tendency using (3.5a). Over this five-day period the zonal wind weakened substantially along the southern portion of the jet core as well as in its exit region near 160°W. Understanding what features and, through (3.6), what processes contributed to the retraction/deceleration of the zonal jet is the focus of the ensuing analysis.

Retractions are focused on weakened zonal flow specifically within the climatological jet exit region in the central north Pacific, often associated with a split jet and a dipole-type block (Jaffe et al. 2011). Various time series of the deceleration averaged over an area encompassing the jet exit region are shown in Fig. 3.6a. The local deceleration was calculated using the full 300 hPa height field and height perturbations taken with respect to the 11-15 February mean, (black and blue lines, respectively). The close match between the two time series confirms that

the basic state chosen for the diagnosis is suitable for capturing the overall change in zonal wind. Both fields show that during 11-12 February the zonal wind weakened in this region, then strengthened on 13 February, and weakened thereafter. The first period of deceleration is associated with Feature A, the second with Feature B. The integrated, observed deceleration calculated using the total height field was -37 m s^{-1} over the five-day period (Table 3.1). Calculating the deceleration in this region using height anomalies yields -37 m s^{-1} as well. This provides confidence that the basic state definition employed in PTD in Chapter Two captures the observed, total weakening of the jet. Accordingly, the same PTD output is employed in this study. The PTD components in (3.6) pertain to only height tendencies associated with the *upper-level* QGPV structure, as the terms in (3.6) advect either background or perturbation upper-level QGPV. Chapter 2 demonstrated that most of Feature A's development was related to the reorganization of the upper-level (50-500 hPa) QGPV, so terms advecting low-level QGPV were excluded as in previous studies. To confirm that the upper-level QGPV structure similarly accounts for most of the total retraction, the height anomaly field attained from inverting upper-level (50-500 hPa) perturbation QGPV, q'_u, (3.7) was used to calculate deceleration.

$$\phi'_u = \mathcal{L}^{-1}(q'_u) \qquad (3.7)$$

The resultant height field ϕ'_u accounted for most of the total observed weakening of the zonal wind at 300 hPa, with an integrated wind speed change of -32 m s^{-1} (pink line Fig. 3.6). The cumulative deceleration attained using the QG height tendencies output by PTD using (3.6) accounts for -25m s^{-1}, 78% of the retraction associated with upper-level QGPV (red line Fig. 3.6b), confirming that the PTD method can explain the majority of the observed retraction of the jet exit region in this case.

3.3.1 Piecewise Zonal Wind Tendency Results

The terms that drove the amplification of Feature A are not necessarily the same terms that contributed most to the jet retraction. Figure 3.7 shows time series of the deceleration arising from the five terms in (3.6), revealing that the highest-magnitude term is the propagation/deformation term, which oscillates in concert with the total deceleration. This term includes the advection of ridges and troughs by the time mean geostrophic wind, so a large contribution from this term is not surprising. The downstream development term varies inversely with the advection/deformation term and the total deceleration. This term includes the effect of QGPV anomalies reorganizing the background QGPV gradient. For example, northerly flow on the western side of a trough will lead to positive background QGPV advection and height falls, reflecting the trough's tendency to propagate upstream. Upstream propagation is opposed by the background wind's tendency to advect the trough downstream. As a result, the advection/deformation term and downstream development term are anticorrelated.

The baroclinic development term first negated retraction on 11 February and then promoted it from 12-13 February. Thereafter this process makes barely any direct contribution. Interestingly, upper-level, nonlinear vortex-vortex interactions, which had barely any influence on the amplification of Feature A, systematically contributed to jet retraction throughout the five days. The contribution to retraction from low-level nonlinear interactions oscillated closely around zero in this location.

It was previously noted that the instantaneous change in zonal wind is heavily influenced by the transient movement of eddies into and out of the region where retractions are identified. Term A, including effects from advection, deformation and superposition, reflects the oscillatory behavior of height anomalies as they are advected by the background wind into and out of the

box. The downstream development term also reflects wave-like behavior. Nonetheless, from

11-15 February the jet exit region weakened overall, despite intermittent oscillations. To

eliminate the transient effect of waves propagating eastward, the changes in zonal wind from

each term in (3.6) were integrated over the five-day period. Results are shown in Table 3.1,

revealing that the integrated effects of Terms A, B, C, and E are all near zero. It is only Term D,

representing upper-level vortex-vortex interactions, which accounts for the -25 ms^{-1} deceleration

produced by all PTD terms. Figure 3.8 shows the spatial maps of the integrated terms from 11-

15 February, revealing that it is not only in this region where Terms A, B, C are near zero, but

everywhere in the domain (Fig.3.8 a-c). This is an artifact of the basic state definition employed

in this study, and will be changed in future analysis. The nonlinear terms exhibit strong,

opposing dipoles of acceleration and deceleration that straddle the jet meridionally (Fig. 3.8e-f).

Deceleration associated with upper-level non-linear advection was located within the jet exit

region and southern portion of the jet core, accounting for all of the retraction explained by the

QG terms.

To contextualize the conditions during which nonlinear interactions produce retraction,

Figure 3.9 shows the 12 February mean forcing associated with term D, as well as the height

tendency response. Negative QGPV advection produces positive height tendencies, which are,

in turn, associated with deceleration on their southern edge. The geostrophic wind associated

with ϕ_u' represents the advecting wind for term D, which rearranges the q_u' field shown (Figure

3.9a). Due to the slight offset in the phasing of ϕ_u' and q_u', negative q_u' advection occurs, most

notably on the eastern edges of Features A, B, as well as on the eastern edge of the trough in-

between, evidenced by the positive height tendencies in those locations (Figure 3.9b).   Features

A and B are associated with strong, negative q_u' anomalies that are greatest in magnitude near

45°N, leading northerly flow on each anomaly's eastern side to advect low q'_u southward, producing height rises. Simultaneously, southerly flow on the western edge of A and eastern edge of a trough, advected negative q'_u in the subtropics northward, also coinciding with negative q'_u advection. As a result of the coordinated negative PV advection by A, B and the trough in between, a continuous region of height rises extends from 110-200°E, and to their south, deceleration is observed, accounting for the observed jet retraction. All three height anomalies associated with negative q'_u advection were positively tilted on 12 February, the day marking the strongest forcing for deceleration during the five day period. Term D's net influence on height rises and deceleration is confirmed from inspection of the five-day mean height tendencies and deceleration in Figure 3.10. The positive height tendencies in Fig. 3.10 indicate that negative QGPV advection, specifically negative q'_u advection by v'_{gu}, systematically occurred throughout the jet axis during this five day period. To the south of the height tendencies, and as anticipated by (3.6a), deceleration of the zonal wind is continuous throughout the southern half of the jet from 100°E to almost 160°W.

3.4 Discussion and Conclusions

In this chapter a novel perspective for understanding wind speed changes derived as an extension to the PTD diagnostics introduced by Nielsen-Gammon and Lefèvre (1996) is presented. It was shown that the simple relationship between horizontal gradients in height tendencies and changes in the geostrophic wind holds for instantaneous or time-averaged changes in the geostrophic wind. This relationship can be combined with piecewise tendency analysis to split the total deceleration field into contributions from various, distinct processes. This approach was applied to investigate the onset of a long-lived north Pacific jet retraction in mid-February 2006, and the influence on retraction from a wave train including two potent

anticyclonic anomalies was quantified. Feature A, a rapidly growing, high-amplitude but meridionally elongated ridge, contributed to retraction more as a weak height anomaly early in its lifecycle than when it was strongest in amplitude. Following the initial retraction related to Feature A, Feature B, a modest but persistent and well-placed height anomaly, continued to retract the jet.

The influence of various processes that can contribute to QG height tendencies, and thus retraction, was quantified through extension of the piecewise tendency diagnosis method of Nielsen-Gammon and Lefèvre (1996). The instantaneous changes in the zonal wind were heavily influenced by mean-flow advection of anomalies, while the cumulative 11-15 February retraction was dominated by nonlinear vortex-vortex interactions – specifically, differential negative QGPV advection. The net flux of low QGPV from the tropics/subtropics northward is most commonly the way in which nonlinear advection is viewed as a mechanism to influence the mean state and aid in blocking onset or maintenance (Hoskins et al. 1983, Crum and Stevens 1988). Intriguingly, in this case it was shown in Figure 3.9 that negative QGPV anomalies associated with Features A and B and located north of the jet, were differentially advected *southward*. Anticyclonic anomalies that reach the poleward side of the jet, as observed in this case and in many retractions, seem to have a unique ability to influence the zonal wind given the relative position of their associated nonlinear advection and the jet.

Some advantages to the expanded PTD approach is that it can be applied to instantaneous, time mean, or spatially filtered data, as the only assumption made is QGPV conservation. Acceleration of both the zonal and meridional components of the geostrophic wind can be diagnosed in this manner, for stationary or transient features, with no requirement of a zonal basic state. The expanded PTD method also merges information about the amplification

and lifecycle of eddies with their propagation and influence on the geostrophic wind. Finally, merging QGPV inversion and a zonal wind diagnostic allows for separate quantification of the influence of both lower- and upper-level QGPV structures on the zonal wind.

Given that the basic state is defined as a five-day time mean in this study, the contribution to zonal wind tendencies from terms that reference only one anomaly field *must* add up to zero when integrating over the five-day period. This explains why the integrated effect of Terms A, B, and C are near zero. However, given that 78% of the total retraction is explained by the vortex-vortex interactions, even changing the basic state definition to, for instance, a spatial filter, would only possibly account for an additional 22% of the total zonal wind change. Thus it seems the results found here, consistent with previous studies regarding blocking and nonlinear processes, are not cripplingly dependent upon the time mean basic state definition. In the future a large-scale/small-scale definition of the basic state will be employed to provide as complete an analysis as possible.

Note that the interpretation of the contribution of the deformation/superposition term (Term A) differs dramatically depending upon whether one is diagnosing zonal wind changes or height changes, pursued in traditional PTD. Chapter Two diagnosed height tendencies at the instantaneous height maximum associated with Feature A. At the center of a height anomaly, any contribution from Term B cannot be due to the symmetric advection of A by the background wind, but arises rather from asymmetry (commonly deformation) in the flow. Such asymmetry rearranges the shape of anomalies and can enhance their circulation, thus amplifying an existing height anomaly (Figure 2.1). However, for the analysis of zonal *wind* tendencies, the region chosen was a fixed box in the exit region, used by Jaffe et al. (2011) to identify jet retractions. Therefore, the simple movement of ridges and troughs downstream contributes to the

instantaneous zonal wind tendency evaluated, regardless of whether there is deformation (or any asymmetry) in the mean state. The distinction between interpretations is made here not to diminish the effect of advection on the zonal wind, but rather to clarify the various ways in which the advection/deformation term may act.

3.4.1 Comparison with an alternative zonal wind diagnostic

The dominance of nonlinear vortex-vortex interactions in retracting the jet is consistent with discussion of the role of nonlinear interactions in changing the QGPV gradient following the geostrophic flow, presented by Hoskins et al. (1983). They showed that the eddy vorticity flux divergence is proportional to the Lagrangian derivative of the large-scale, or low-frequency, QGPV in the absence of sources and sinks:

$$\left(\partial_t + \overline{v_g} \cdot \nabla\right)\bar{q} = -\nabla \cdot \overline{v_g'q'} \qquad (3.8)$$

Where the right-hand-side of (3.8) is negative, the QGPV gradient and geostrophic wind will weaken. A common application of this relationship is to diagnose blocking regions, where a northward flux of negative QGPV will lead to or maintain a weak mean QGPV gradient, reinforcing the block (Hoskins et al. 1983; Shutts 1983; Trenberth 1986). To investigate the relationship between the Eulerian changes in wind speed as diagnosed using (3.6), versus the Lagrangian change in the QGPV gradient using (3.8), the eddy vorticity flux divergence was calculated averaged from 11-15 February (Fig. 3.11). Convergence (negative values) of the eddy vorticity flux leads to a weakening of the QGPV gradient and thus indicates a weakening of the zonal wind, moving with the geostrophic flow. Regions of strong convergence are observed within the jet core from 140-170°E, 35°N, and in the entrance region at 100-125°E, 40-45°N (Fig. 3.11a). Weaker convergence is observed in the exit region at 40-45°N, 170°E, but within the box used to evaluate retraction there is also some weak divergence. To the north and south

of the eddy vorticity flux convergence are areas of divergence, including one particularly strong

region to the north in a linear band at near 40°N. Eddy vorticity flux divergence implies a

strengthening of the QGPV gradient and geostrophic wind, suggesting that from 11-15 February

the mean QGPV gradient and jet core was forced to shift northward by the eddy fluxes.

Figure 3.11b shows the sum of the piecewise deceleration, essentially the sum of the

nonlinear interactions (Terms D and E), with the eddy vorticity flux convergence as in Fig. 3.10a

shown in the contours. The region of eddy vorticity flux convergence in the jet core is located

between a region of strong *local* deceleration to the south and acceleration to the north. This

spatial relationship suggests that the local changes in the zonal wind as diagnosed using (3.6)

also coincide with changes in the absolute magnitude of the QGPV gradient. Stronger westerly

wind to the north, and weaker westerly wind to the south appears to result in change in the

magnitude of the mean QGPV gradient, so that the gradient weakens in the region marked by the

vorticity flux convergence. In other words, the QGPV gradient is differentially advected by the

wind so as to weaken the QGPV gradient, and zonal wind, within both the jet core and exit

region, in both an Eulerian and Lagrangian sense.

The change in the jet structure associated with the beginning of retraction is presented

Figure 3.12, which shows the daily mean QGPV and zonal wind on 11 February and 15

February. The upstream movement of a persistent, high-amplitude ridge, located in the eastern

Pacific near 145°W on 11 February, and near 165°W by the 15th, coincided with retraction of the

jet exit region. The upstream movement of the ridge is attributable to the growth of Feature A.

While the eddies are included in the total QGPV field, it is evident that the QGPV gradient and

jet core strengthened to the north and weakened to the south during this period, just as the eddy

vorticity flux divergence indicated. In particular, near-zero PV air was located near 30°N on 11

February, and shifted northward to 40°N by 15 February, revealing that a northward shift of the jet core accompanied the retraction of the exit region. The northern shift of the jet core was forced by the circulation of Feature B at the same time that A shifted the exit region upstream, and together these two anticyclonic anomalies greatly modified the structure of the north Pacific basin over this five-day period. As discussed in Chapter 2, retraction continued after B approached the jet exit region, becoming more isotropic and further displacing the exit region upstream. Thereafter, a third anticyclonic anomaly repeated the process and reinforced retraction (see Fig. 2.5).

An important characteristic of the 2006 retraction was related to the propagation of anticyclonic anomalies on the poleward side of the jet and their impact upon the zonal wind. Chapter 2 diagnosed the amplification of a ridge that reinforced a low-frequency block, and by shifting the block upstream, facilitating retraction. The cumulative influence of A and B, and the trough located in between, on the zonal wind manifests itself through nonlinear interactions, which dominated the QG zonal wind tendencies from 11-15 February. Nonlinear advection was strongest on 12 February, coinciding with the time during which the wave train was most positive tilted. Mak and Cai (1987) demonstrated that a positively tilted eddy in a region of cyclonic shear, indicating shearing deformation, is conducive to the barotropic growth of the eddy at the expense of the kinetic energy of the environment. Here the retraction, and simultaneous amplification of Feature A, could indicate that a barotropic energy exchange in which kinetic energy from the environment is transferred to kinetic energy of an anomaly, is indeed occurring. Ongoing research suggests that this configuration (positively-tilted height anomalies on the cyclonic shear side of the jet) is often observed during jet retraction.

The dominant influence of nonlinear, vortex-vortex interactions in facilitating jet retraction, attained through a novel expansion of QG piecewise tendency diagnosis to the geostrophic wind tendencies, is consistent with Shutts's perspective on blocking, which emphasized the role of eddy vorticity flux convergence as an important force that maintains blocking against dissipation. More recently, Yamazaki and Itoh (2013) proposed an alternative way vortex-vortex interactions can impact the storm track and blocking through a 'selective absorption mechanism'. They considered the dominant interaction as one where eddies of different sizes impose different net accelerations on the eddies surrounding them, and how a blocking anticyclone preferentially 'attracts' smaller-scale anticyclones, maintaining the block. What differs in this case is the linear band of height tendencies produced by three height anomalies in a wave train, which all produced nonlinear, negative PV advection throughout the jet core and exit region. There are, it appears, a wealth of ways in which vortex-vortex interactions can alter the circulation.
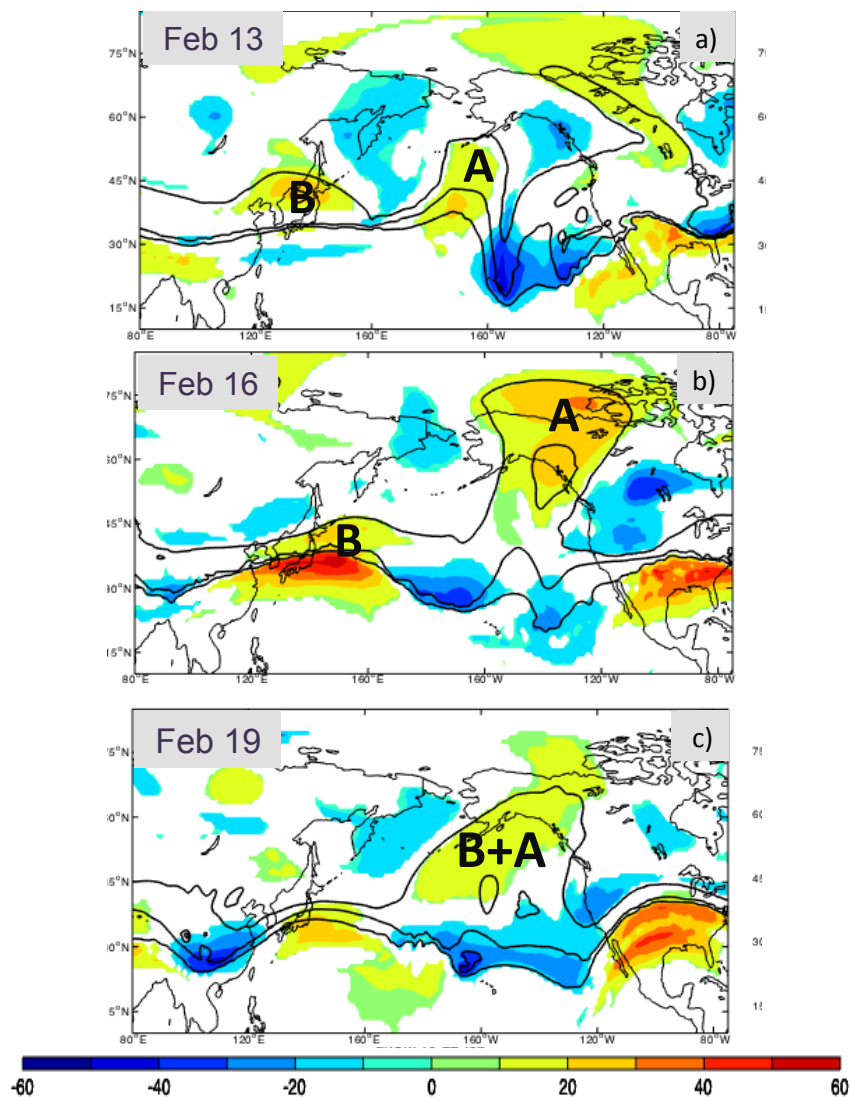
Figure 3.1: The fill shows the potential temperature anomalies on the 2PVU surface on a) 13 b) 16 and c) 19 February 2006. Jet retraction began 15-16 February (Jaffe et al., 2011). The potential temperature anomalies were calculated with respect to the 1979-2015 mean for each day. The contours show the total 315, 330 and 345 K potential temperature surfaces on the 2PVU surface at each time. Anticyclonic anomalies A and B are labeled.
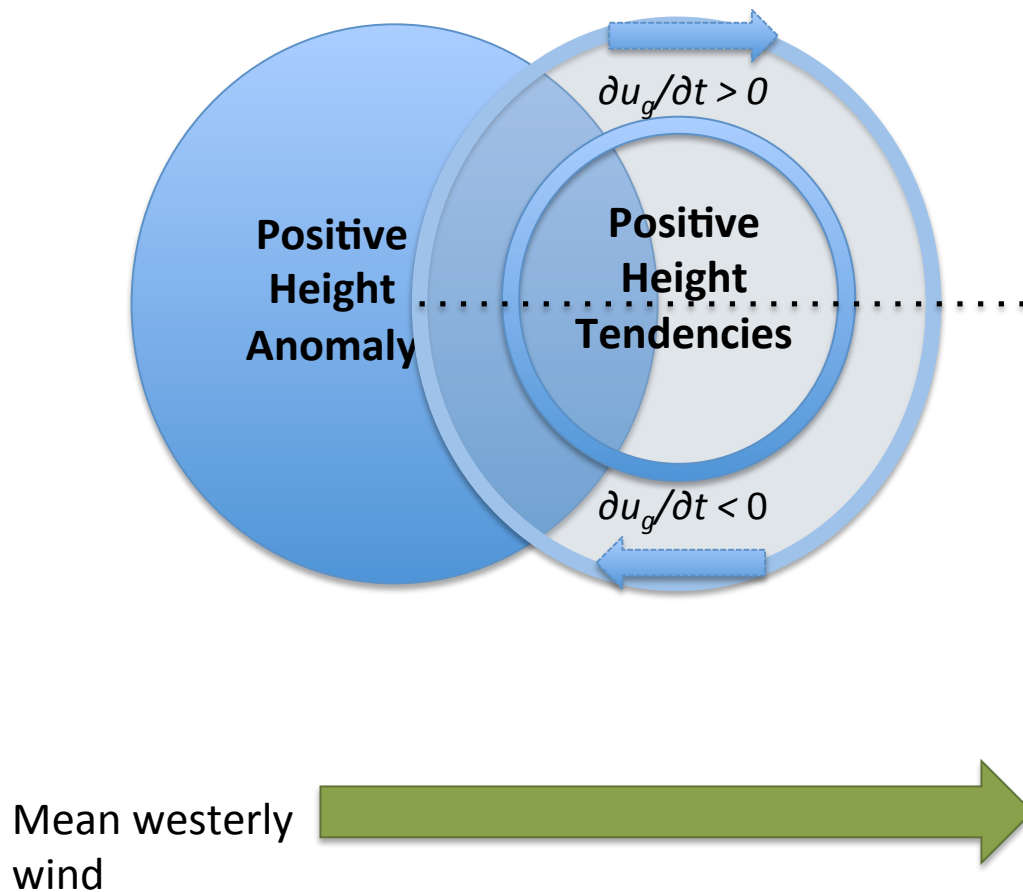
Figure 3.2: Schematic demonstrating the distribution of the local change in the geostrophic zonal wind around a positive height anomaly. Where height tendencies increase with latitude, the zonal wind will weaken, and where height tendencies decrease with latitude, the zonal wind will strengthen (blue arrows). Adding the blue arrows to a mean westerly wind on the ridge's southern edge indicates the effect of a ridge north of the jet, and its ability to weaken the zonal jet.
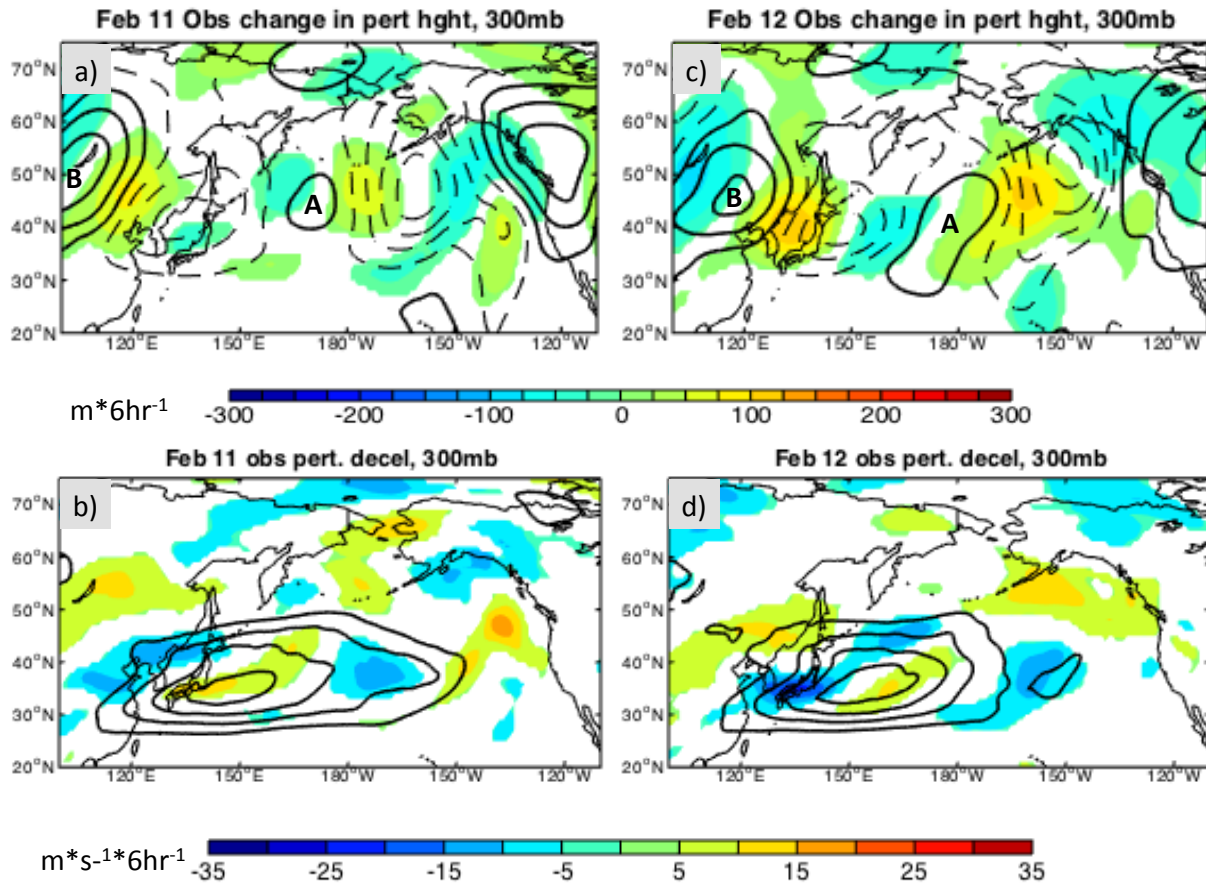
Figure 3.3: In the top panels the fill is the 300hPa height tendency field on a) 11 February and c) 12 February. Units of height tendencies are meters per six hours, with values less than a magnitude of 15 m (6hr)$^{-1}$ whited out. In contours are the 300hPa height anomalies, calculated with respect to the 11-15 February time mean (same anomaly definition as PTD in part one of this paper). Contours start at +/-50 m every 100m, solid positive and negative dashed. Anticyclonic anomalies A and B are labeled. In the bottom panels the fill shows the corresponding change in the geostrophic zonal wind calculated from the height tendency fields on b) 11 February and d) 12 February. Units of zonal wind change are m s^{-1} (6hr)$^{-1}$, and values less than a magnitude of 4 are whited out. The contours show the geostrophic wind contoured every 10 m s^{-1} starting at 30 m s^{-1}.

a)

c)

A

B

Feb 13 obs pert. decel, 300mb

$m*6hr^{-1}$

b)

Feb 14 obs pert. decel, 300mb

d)

-35   -25   -15   -5   5   15   25   35
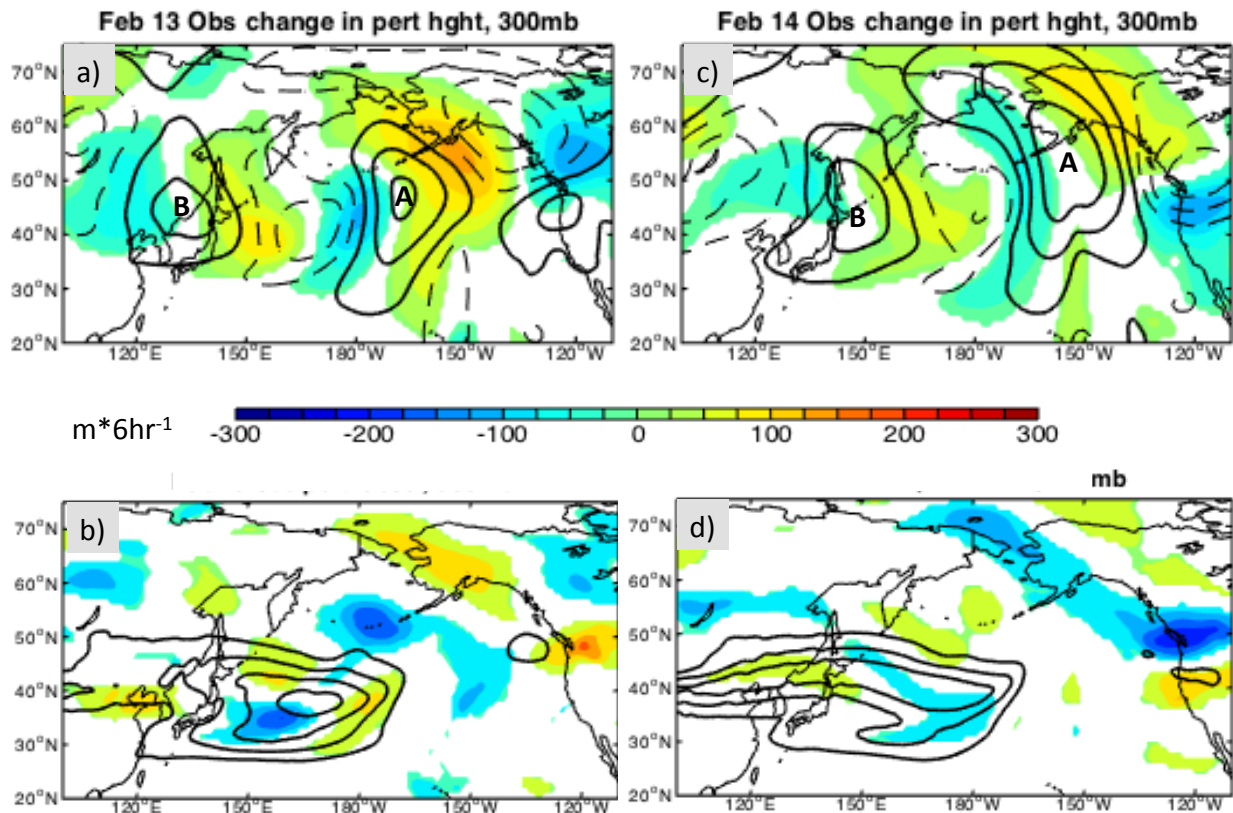
Figure 3.5: The fill shows the 11-15 February change in zonal wind in m s^{-1}. The contours show the 11-15 February mean geostrophic zonal wind, contoured starting at 30 m s^{-1} every 10 m s^{-1}. The green box indicates the region over which the retraction is diagnosed.
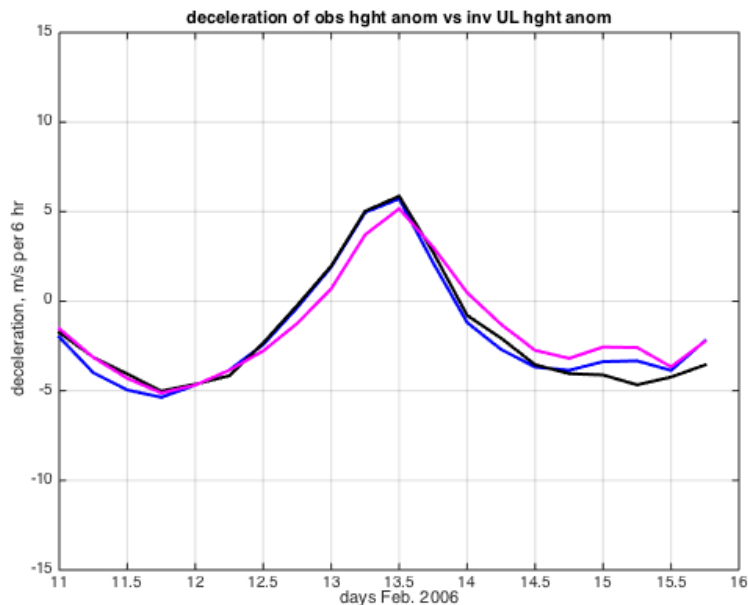
a)
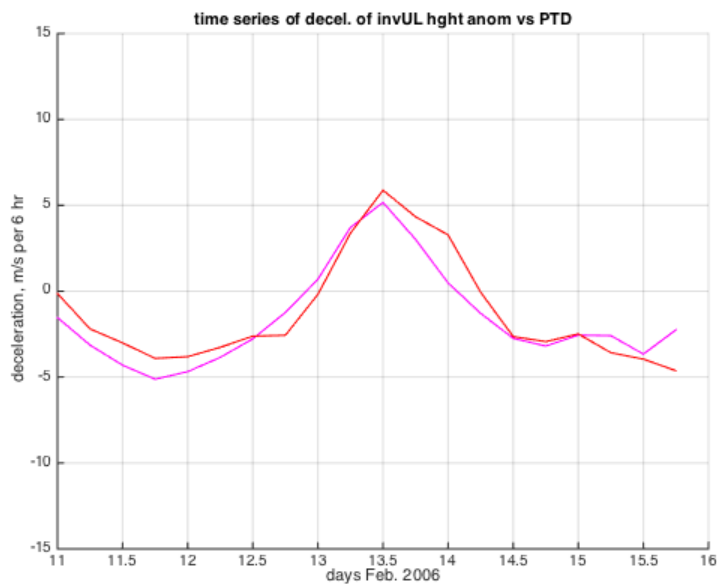
b)
Figure 3.6: Time series tracking zonal wind change (units m s^{-1} (6 hr)$^{-1}$ averaged from 170-200°W, 30-40°N, from 11-15 February, using six-hourly data. a) shows zonal wind tendency using the total height field (black line), height anomaly field (blue line) and the inverted height anomaly field associated with 50-500hPa perturbation QGPV (pink line). b) The pink line is as in a), and the red line shows the zonal wind tendency explained using the height tendencies from PTD (Eqn 3.6). The close correspondence between the time series provides confidence in the ability of the PTD methodology to explain the majority of the observed jet retraction.
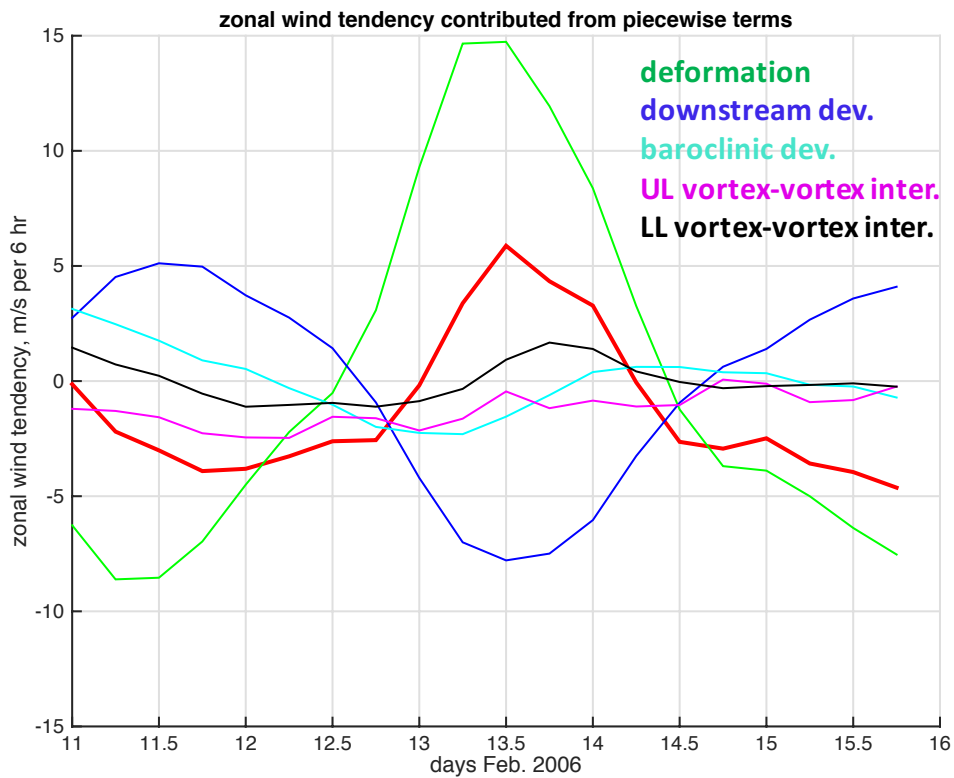
Figure 3.7: Time series of the individual PTD components' contribution to the zonal wind tendency using Eqn 3.6 from 11-15 February. The red line is the sum of all terms, the green line is Term A, dark blue line Term B, light blue line Term C, pink line Term D, and black line Term E, from Eqn 3.6.

Height Field	Integrated Zonal Wind Tendency (m s^{-1})
Total Geopotential Height	-36.7071
Geopotential Height Anomalies	-37.0795
Upper Level QGPV Height Anomaly	-31.8388
Total PTD	**-25.1002**
Term A: Deformation/Superposition	-0.0079
Term B: Downstream Development	-0.0186
Term C: Baroclinic Development	-0.0100
Term D: Vortex-vortex UL	-24.8444
Term E: Vortex-vortex LL	-0.2193

Table 3.1: Integrated tendency of the zonal wind from 00z 11 February – 18z 15 February 2006 using various height tendency fields.
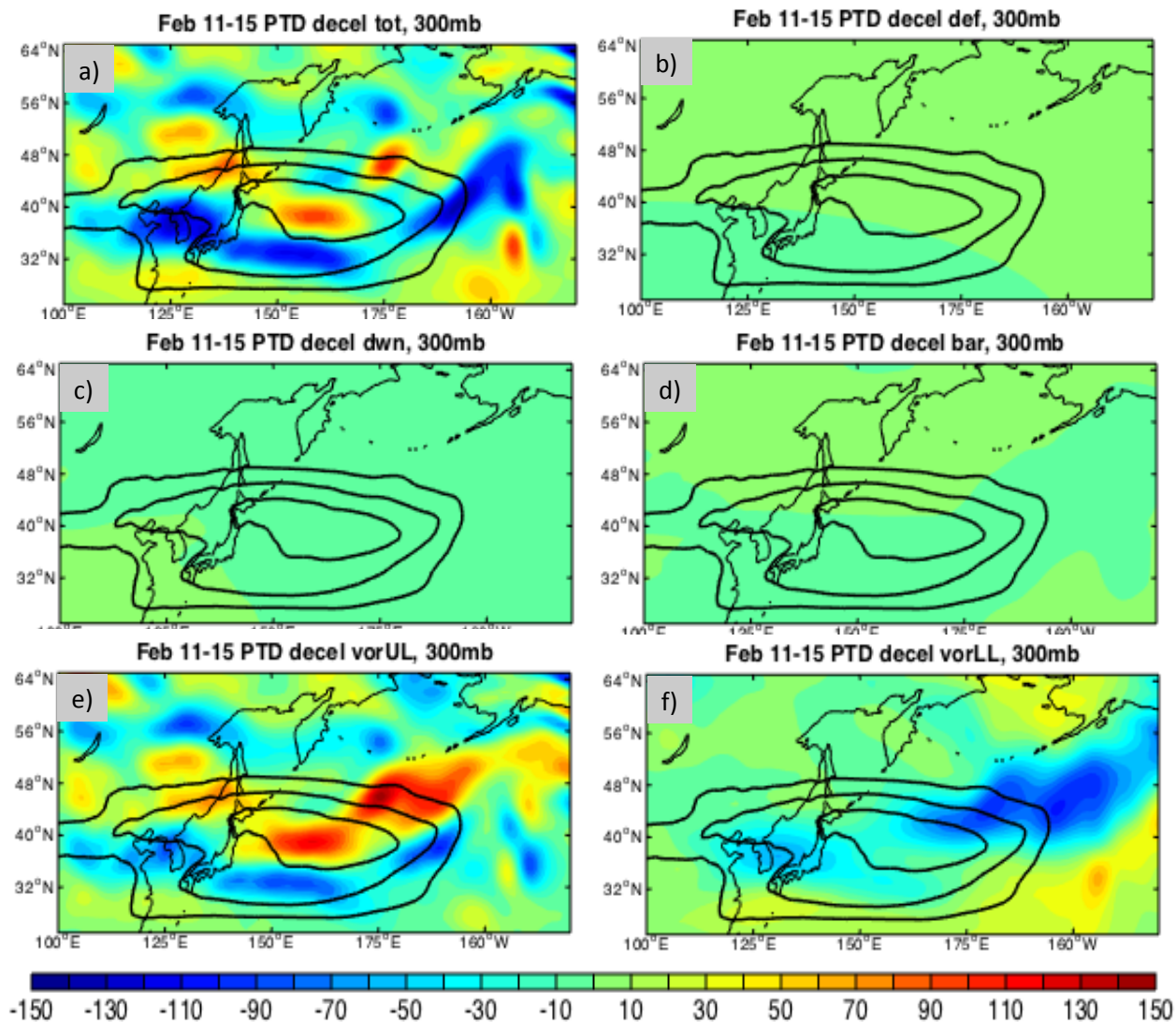
Figure 3.8: The color shading shows the integrated zonal wind tendency from 00z 11 February – 18z 15 February 2006 from terms in Eqn (3.6) in ms^{-1}. a) shows the sum of terms A-E, b) Term A (advection by mean flow, deformation, superposition), c) Term B (downstream development), d) Term C (baroclinic development), e) Term D (upper-level vortex-vortex interactions), and f) Term E (low-level vortex-vortex interactions). The contours in each plot are the same and show the 11-15 February mean geostrophic wind, contoured starting at 30 m s^{-1} at intervals of 10 m s^{-1}.
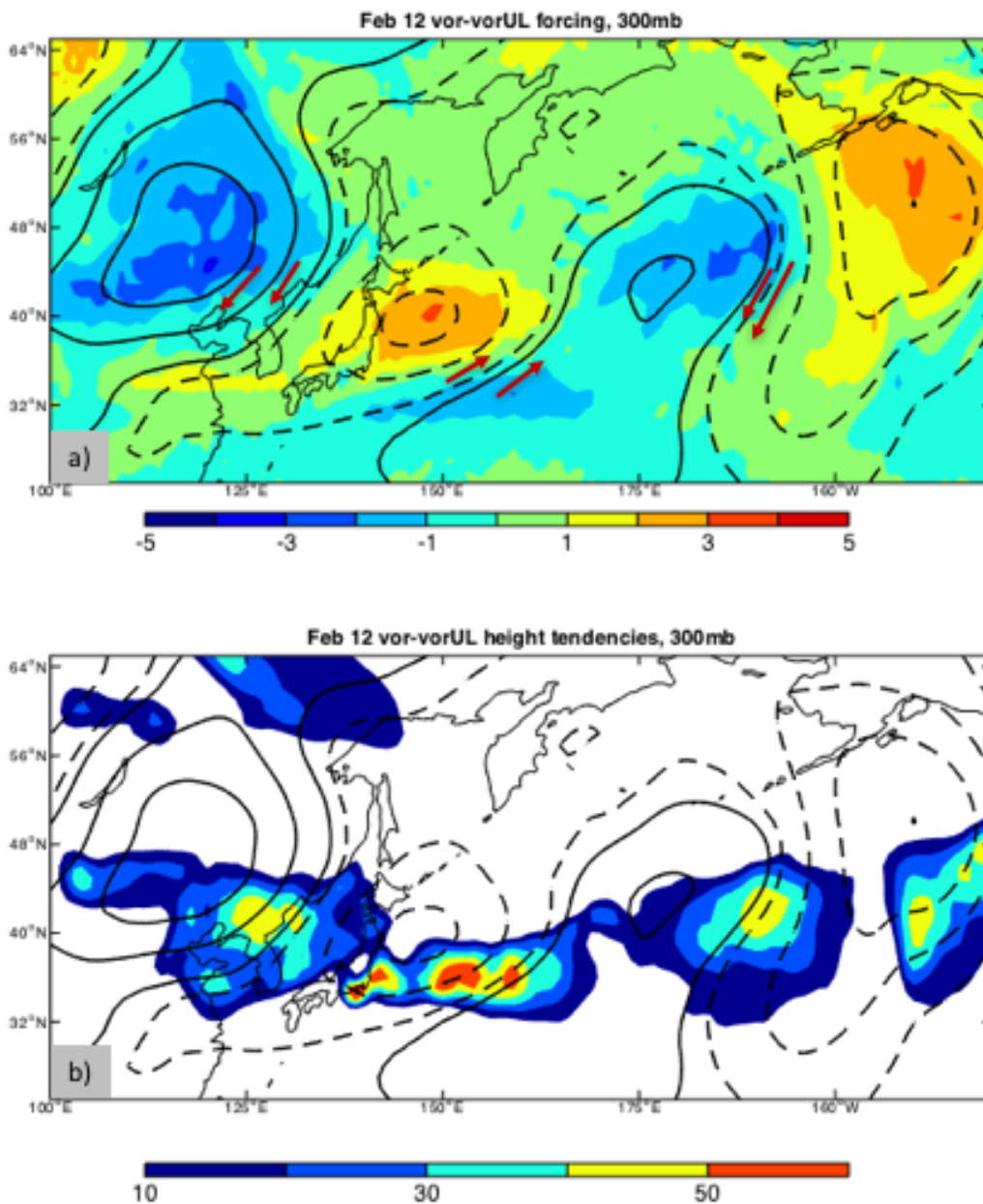
Figure 3.9: a) The color shading shows the 12 February average q'_u field in units of 10^{-4} s^{-1}. The black contours show the 12 February average ϕ'_u field, with positive (negative) values in solid (dashed) lines contoured starting at +/- 20 m every 100 m. Red arrows denote v'_{gu}. b) The color shading shows the 12 February height tendencies associated with Term D and the forcing shown in (a). Height tendencies are in units m (6hr)$^{-1}$, with positive values about 10 shown. The black contours are as in (a).
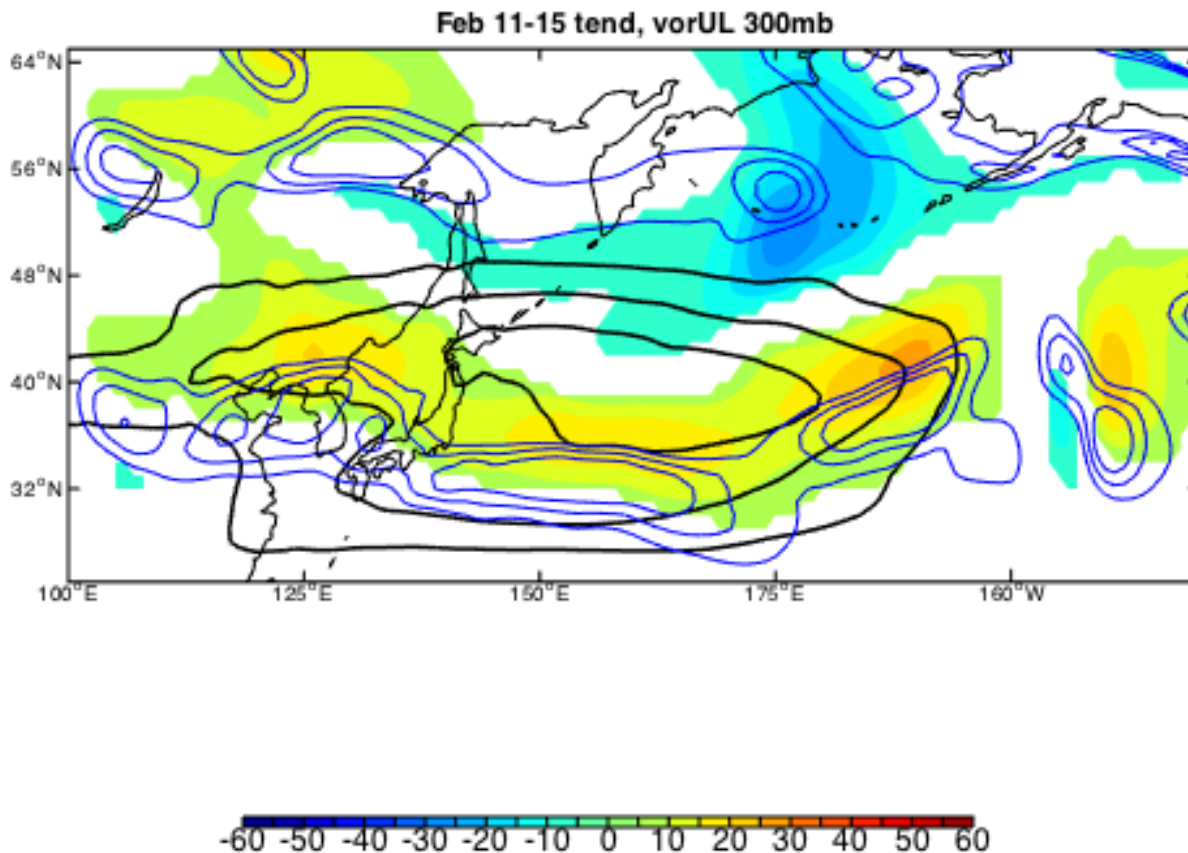
Figure 3.10: The color shading shows the average height tendencies associated with Term D, with values less than 5 m $(6hr)^{-1}$ whited out. The black contours show the 11-15 February zonal wind isotachs starting at 30 m s^{-1} every 10 m s^{-1}. The blue contours indicate the zonal wind tendency associated with Term D, calculated using the height tendencies in the color shading. The zonal wind tendency is contoured every 10 m s$^{-1}(6hr)^{-1}$, starting at -10 in intervals of 10.

300 hPa Eddy Vorticity Flux Convergence 11-15 February
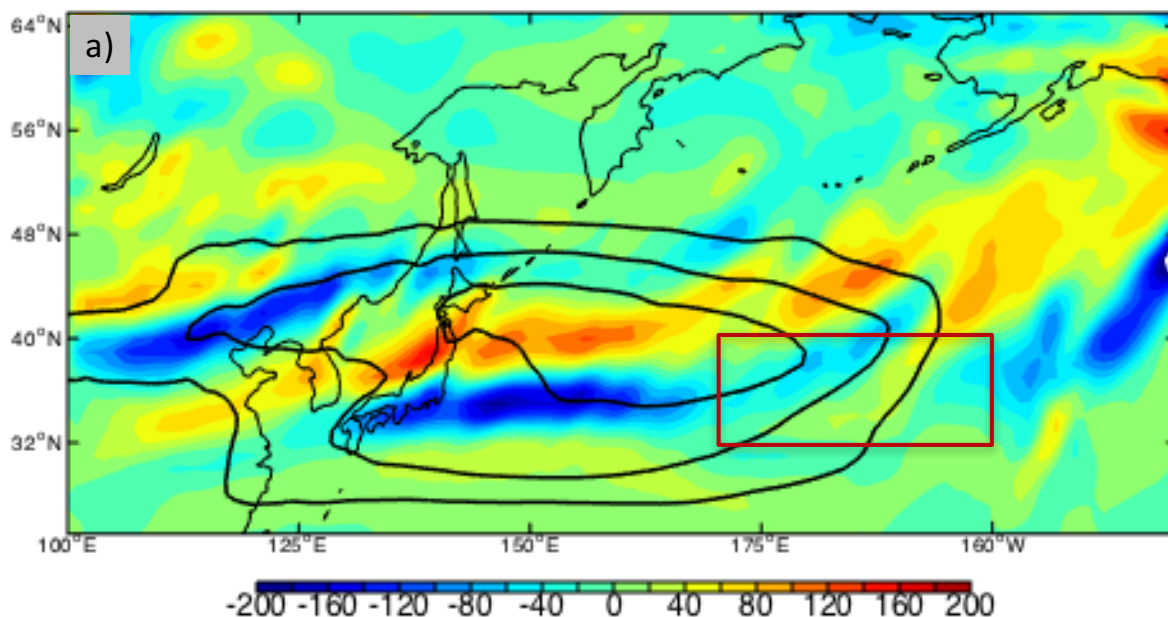
300 hPa Deceleration (fill) and Convergence (red line) 11-15 February
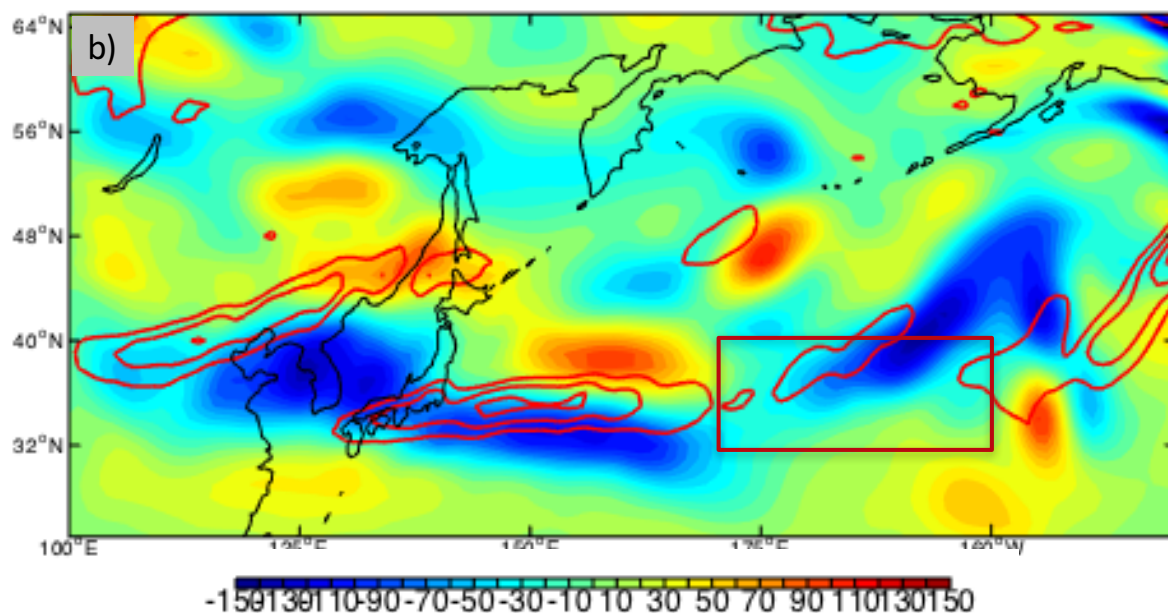
Figure 3.11: a) Meridional eddy vorticity flux convergence of upper-level perturbation QGPV integrated from 00z 11 February – 18z 15 February is in the fill. Units are $10^{-9}\,m^2\,s^{-1}$. The contours are the 11-15 February mean geostrophic wind, contoured starting at 30 m s^{-1} every 10 m s^{-1}. The red box shows the region used to track retractions.
b) The color shading shows the deceleration from Eqn (6) in units m s^{-1}. The meridional flux divergence is shown in the red contours, for negative values only (ie convergence) starting at 20 * $10^{-9}\,m^2\,s^{-1}$ at intervals of 60 * $10^{-9}\,m^2\,s^{-1}$.

300mb QGPV Feb11

a)

300mb QGPV Feb15

b)
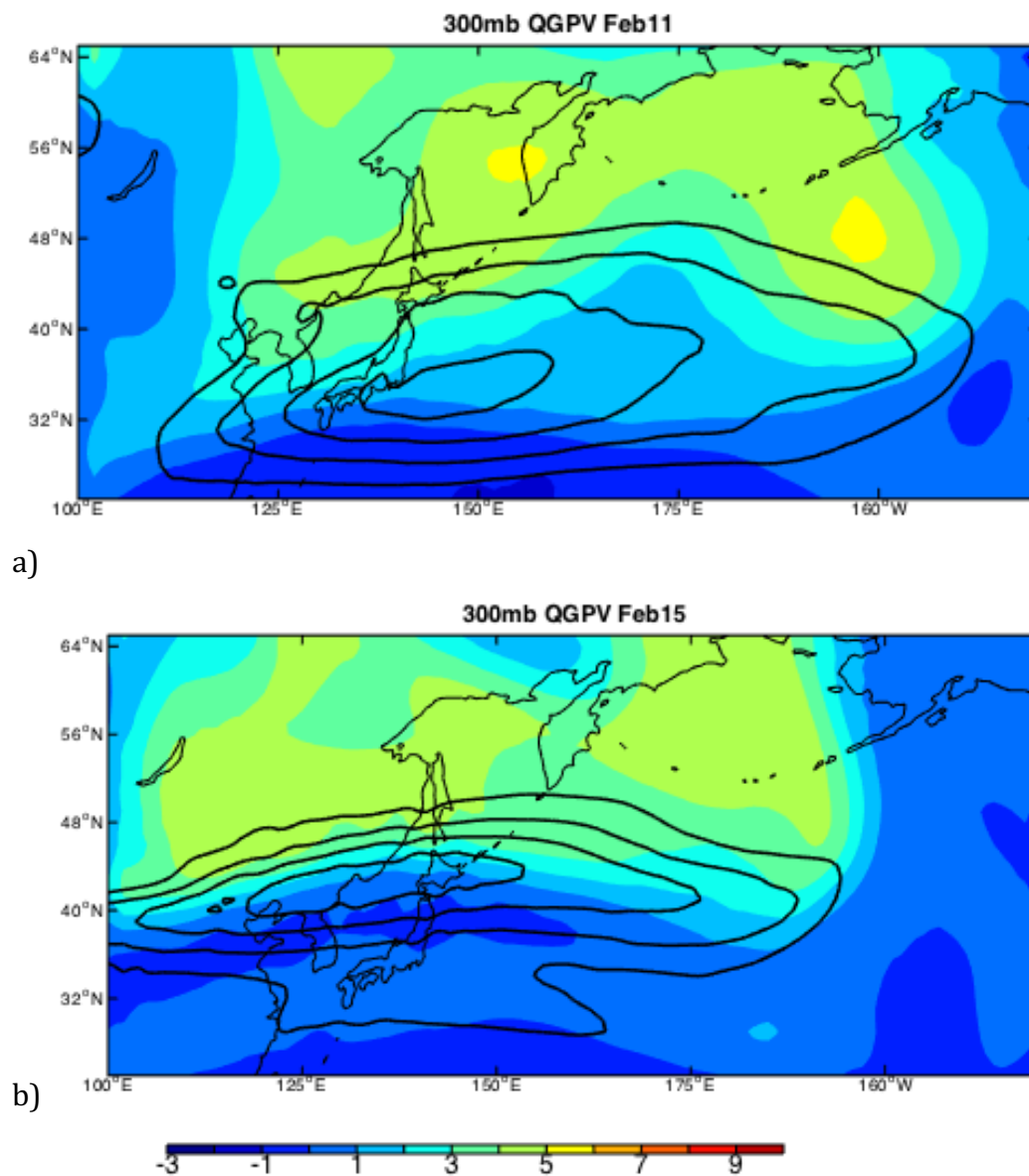
Figure 3.12: The color shading shows the daily mean QGPV and in contours is the zonal geostrophic wind on a) 11 February and b) 15 February 2006. Units of QGPV are 10^{-4} s^{-1}. Contours start at 30 m s^{-1} at intervals of 10 m s^{-1}.

CHAPTER 4: 2017 RETRACTION CASE

In mid-February 2017 a jet retraction was associated with significant Hawaiian flooding and cooler-than-average temperatures over western North America. This chapter will examine what, if any, dynamic and synoptic similarities exist between the 2006 and 2017 cases. First, the expanded PTD methodology introduced in Chapter 3 is applied to the 2017 retraction to determine whether vortex-vortex interactions account for the observed initial retraction in this case. Thereafter, traditional PTD is used to investigate the lifecycle of an LC1-breaking wave associated with retraction, to determine if there are similarities with the lifecycle of the 2006 Feature A diagnosed in Chapter 2. This chapter will conclude with a discussion of the similarities and differences between the 2006 and 2017 case, and cursory examination of other retractions.

4.1 Synoptic Overview of 2017 Case

Tropopause maps will be used to investigate the synoptic evolution that coincided with the onset of a jet retraction on 17 February 2017. Two days before the jet began to retract (15 February), the potential temperature gradient on the dynamic tropopause (Fig. 4.1a) was quite strong and zonal across the north Pacific basin to 140°W, indicating a robust, extended jet. A high-amplitude ridge was in the process of overturning in the jet exit region over western North America, breaking between the 330-345K isentropic layer. Upstream over China, a shortwave, cyclonic anomaly was observed, and was associated with a diversion of the 330 and 345K isentropic surfaces to the south. Finally, a wave train beginning with an anticyclonic feature at 75°N, 100°E, a downstream trough, ridge, and finally, a cyclonic feature located just north of the jet at 150°E, 35°N, was observed over eastern Russia. Over the next two days, 16-17 February, the downstream development of a potent trough was observed near 160°E, 35°N, first disrupting

the zonal jet and diverting it southward around the base of the trough (Fig. 4.1b-c). At this time, a positively-tilted anticyclonic feature was present upstream of the trough as on 15 February, also part of the aforementioned wave train emanating from higher latitudes over Siberia.

The trough amplified and propagated eastward the next day, 18 February, while just upstream an anticyclonic anomaly emerged between the 315-330K layer (Fig. 4.1d). The 315K surface is diverted northward around the northern edge of the anticyclonic anomaly, weakening the meridional potential temperature gradient and, correspondingly, the zonal jet. The ridge and trough both persisted over the next few days, the ridge amplifying and the trough decaying (Fig. 4.2a-b). By 20 February, the two anomalies were associated with substantial deformation at the date line, and across the north Pacific basin the jet had weakened, evidenced by the weakened meridional potential temperature gradient compared to 15 February (Fig 4.2c). Thereafter, a second anticyclonic anomaly, 'A', developed in the central Pacific amplified from 20-24 February and superposed with the first ridge on February 22. The development of the secondary anticyclone seemed to coincide with a sprawling and potent anticyclonic anomaly, 'B', that propagated over Eurasia and reached the jet entrance region on 21 February (Fig. 4.2c).

The eastward movement of Feature 'B' from over Eurasia to the west Pacific on the poleward side of the jet from 20-23 February, and subsequent development of a high-amplitude LC1-lifecycle ridge downstream ('A'), are strikingly similar to Features A and B in the 2006 case diagnosed in Chapter 3. From the 23-24 February the downstream anticyclone, 'A', continued to amplify and overturned anticyclonically at 160°W within the 315-330K isentropic layer on 24 February (Fig. 4.2f). Meanwhile, 'B' maintained strength and steadily moved eastward from 21-24 February, with the 315 K isentrope confined to its northern edge. The potential temperature gradient was split, with the 315K surface diverted far northward, while the

330K isentropic surface was cut off in the eastern Pacific near 60°N and diverted southward in the subtropics near Hawaii. The 345 K isentropic surface was similarly diverted southward around a cyclonic anomaly that had persisted between 180-160°W from 19 – 24 February (Fig 4.2).

In the next section, zonal wind tendencies will be diagnosed from 17-21 February, coincident with the transition of the jet from extended to retracted. Then, given the similarities between the two LC1 breaking waves associated with retraction in both the 2006 and 2017 cases, traditional PTD is applied to investigated the lifecycle of Feature 'A' from 20-24 February 2017.

4.2 Zonal Wind Tendency Analysis

To investigate the processes facilitating the initial retraction of the jet, the expanded PTD approach to diagnosing zonal wind tendencies was applied to the period 17-21 February 2017. This is the period when the zonal jet is first disrupted and coincides with a similar movement through PC-space as for the 11-15 February 2006 period diagnosed in Chapter 3. The inversion partitioning used for this case is the same described in Chapter 2, except the basic state used is the 17-21 February 2017 time mean. Figure 4.3 shows the deceleration of the geostrophic zonal wind, with the mean position of the jet, averaged from 17-21 February 2017. The jet extended across the Pacific, with its exit region located over North America. Two wind speed maxima are observed, one in the west Pacific and one near 140°W. Strong deceleration is located within the center of the jet near the date line, marking where the zonal wind weakened over this five-day period (Figs.4.1-4.2). The total integrated change in the observed total geostrophic wind speed in the box shown in Fig. 4.3 is about -29 m s^{-1}, and a similar local deceleration is captured using the height anomalies taken with respect to the 17-21 February mean (Table 4.1).

The net deceleration produced by the QG piecewise height tendency terms in the boxed location is very similar to observations. The time series of the instantaneous deceleration occurring within the box is shown in Figure 4.4. The zonal wind weakened consistently from 12z 17 February to 18z 19 February, strengthened for one day, and then experienced a second period of deceleration. The sum of the QG terms exhibits some differences in the timing of deceleration, but overall matches the observed variations in the zonal wind quite well. Figure 4.5 shows the individual components of the QG height tendencies (Eqn 4.6), revealing that, similar to the 2006 case, the advection/deformation term dominates the instantaneous zonal wind changes. Upper-level vortex-vortex interactions consistently promoted retraction and accounted for almost 80% of the total deceleration captured by PTD. The remaining 20% is associated with low-level vortex-vortex interactions, a stronger contribution than found in the 2006 case. Another key difference is the extremely weak contribution at any point from downstream development, which was observed to strongly oppose the tendency of the advection/deformation term in the previous case.

Figure 4.6 shows the forcing and height tendency response for the upper-level vortex-vortex interactions on 17 February. At this time the potent trough observed in the tropopause maps (Fig. 4.1c) was located near the date line and was strongest around 35°N, and a streamer of high-QGPV extended to the west from the southern portion of the trough (Fig. 4.6a). A potent anticyclonic anomaly was located northwest of the trough, and both anomalies were positively tilted. An anticyclone was located in the subtropics to the southeast of the trough as well. Negative q_u' advection occurred on the upstream, southern side of the trough, where northeasterly flow cut from low-QGPV associated with the upstream anticyclone, to high-QGPV associated with the trough and its PV streamer. Accordingly, this location was a region of

positive height tendencies (Fig. 4.6b). An even stronger region of positive height tendencies associated with Term D was observed downstream of the trough, where southwesterly flow cuts across low q_u' associated with the subtropical anticyclone. The subsequent negative q_u' advection related to the southward advection of negative q_u' near 150°E, and northward advection of negative q_u' near 180°W, led to the development of a zonally-elongated band of positive height tendencies from 25-35°N. The sharp meridional gradient observed in the height tendency field corresponded to a strong forcing to weaken the zonal wind in a broad area encompassing the jet exit region and southern jet core, leading to retraction (Fig 4.7).

4.3 Lifecycle Analysis

The initial deceleration of the jet, which was related to a positively-tilted trough that perturbed the jet southward (Fig. 4.2a-d), has been diagnosed using the expanded PTD methodology from 17-21 February. In the days following the initial retraction, a high-amplitude ridge developed from 21-24 February, labeled 'A' in Fig. 4.2. 'A' has a lifecycle that seems similar to Feature A in the 2006 case, particularly with both features undergoing an LC1-lifecycle. To determine if the LC1-lifecycle corresponds to similar terms in PTD contributing to development, Feature 'A' will be investigated using traditional PTD.

The same QG inversion methodology and partitioning scheme described in Chapter 2 is applied to diagnose the lifecycle of the high-amplitude ridge that developed from 20-24 February 2017 (Figure 4.2 labeled 'A'). The basic state is defined as the 20-24 February time average, and anomalies are calculated with respect to this five-day period. The mean 300 hPa geopotential height from 20-24 February is shown in Figure 4.8. In the mean is a deformation region with flow partly diverted northward around a preexisting ridge centered near 160°W and partly diverted southward around a subtropical trough to its south. The jet is already rather weak, but

undergoes even further retraction over the five-day period. Comparing the mean state to the 2006 case, the presence of a high-amplitude deformation region, into which the diagnosed ridge propagated, is rather similar. In this case, the deformation region is farther upstream and the jet is weaker, but structurally the transition from zonal to meridional flow bears a resemblance.

The time series of the maximum height value of Feature 'A' is shown in Figure 4.9. Recall that the location of the height maximum moves with 'A', and is not a fixed location as in zonal wind tendency diagnosis. Two periods of intensification, both lasting about one day, are observed when the maximum height anomaly increases rapidly with time. From 12z 21 February – 00z 23 February, in between the two periods of rapid development, the height anomaly maintained its strength but did not amplify substantially. Most of the observed height anomaly observed in the ERA-Interim height field, ϕ_a', is related to upper level QGPV, evidenced by the strong correspondence between the maximum height anomaly values associated with ϕ_u' and ϕ_a'. The time series of the ϕ_l' field indicates a weak, low-level trough was located beneath the amplifying 300 hPa anticyclone until 23 February, after which time a low-level ridge develops beneath the upper-level ridge. This transition in the ϕ_l' field with time indicates a change in the vertical structure near the amplifying ridge from initially baroclinic to equivalent barotropic, similar to what was observed in the 2006 case. The development of the ϕ_u' anomaly accounts for the vast majority of the total growth observed in the ϕ_a' anomaly, so the growth of ϕ_u' will be diagnosed using Eqn 2.6.

Time series of the height tendencies at the ϕ_{tot}' height anomaly maximum calculated using the sum of the piecewise terms (Eqn 2.6) and using the finite-difference calculated and ϕ_u', (Eqn 2.8) are shown in Figure 4.10. The time series are in rather good agreement and reflect the two periods of rapid development when strong, positive height tendencies are observed. The

period of weaker development and weaker height tendencies on 21 February is observed in both time series. The sum of the piecewise terms overestimates the early amplification of the ridge, which is related to a very large contribution to growth from the deformation/superposition term. Nonetheless the piecewise terms capture the temporal evolution of the observed development, even if at some points the magnitude is overestimated.

The contributions to development from the components of the QG height tendencies are shown in Figure 4.11. The deformation/superposition term contributed heavily to the height tendencies and development of Feature 'A'. Indeed, the total height tendency evolution reflects this term's oscillation between initially promoting development, negating it on 22 February, and promoting growth thereafter. The downstream development opposes development early in the period, and continues to oscillating inversely with the deformation/superposition term throughout the five-day period. When the deformation/superposition term opposed development in the middle of the period, the cumulative effect of downstream development, low-level vortex-vortex interactions, and baroclinic development prevented the ridge from decaying. Thereafter, the baroclinic development and upper-level vortex-vortex interactions acted in concert with deformation/superposition to amplify the ridge substantially by 24 February. As a result, the ridge's wavelength increased at the same time it reached a region of weak background QGPV gradient. An increase in phase speed, and decrease in background wind, coincided with A becoming stationary and overturning in place (Fig. 4.2f).

The strong and well-timed contribution to development of Feature A by Term E, $-\boldsymbol{v}'_{gl} \cdot \nabla q'_u$, representing non-linear advection by the low-level circulation, merits further investigation. Figure 4.12 shows the 12z-18z 21 February mean forcing for this term and the height tendency response overlaid with Feature A. At this time a low-level cyclone is observed upstream of

Feature A, and the cyclonic circulation produced a strong footprint at 300 hPa (Figure 4.11a).

Southwesterly flow on the cyclone's eastern side cut across the negative q'_u anomaly associated

with Feature A, advecting low q'_u northeastward. Feature A was located within a region of

strong deformation in the ϕ'_l field at this time, with the flow turning southeastward

anticyclonically to the east of A, and turning northwestward cyclonically to the west of A. As a

result of the deformative low-level wind field and position of A, Term E was associated with

negative q'_u advection and positive height tendencies in a broad region that was particularly

strong northwest of A's maximum. Term E provides just one component of the low-level

QGPV's influence on the upper-level circulation, and in this case a persistent contribution to

growth from the baroclinic development term was also observed for much of the five-day period

(light blue line Fig. 4.10). The low-level circulation, particularly the low-level cyclone upstream

of A, was able to influence both the anomalous QGPV and the background state QGPV in a way

that systematically promoted development. While a contribution to growth from baroclinic

development is rather common, the behavior of the low-level vortex-vortex interactions is rather

unique to this case.

Feature A reached the deformation region in the background state by the 23$^{\text{rd}}$ of

February, coinciding with a contribution to development from the deformation/superposition

term at this time. Figure 4.13a shows the 00z – 06z 23 February q'_u and the background

geopotential height, from which the mean geostrophic wind can be inferred. Feature A is

situated just slightly upstream of the crest of the ridge in the background state, and there is

southerly flow south of A, paired with westerly flow west of A. The height tendency response

from the deformation/superposition term is mostly downstream of A, and at this time overlaps

with A's height maximum. As such, the mean state deformation rearranged q'_u so that A

becomes more consolidated and its circulation amplified.

4.4 Discussion and Comparison with 2006 case

A second retraction that occurred in February 2017 was investigated in this chapter, and

several similarities and equally intriguing differences between the two cases have been

highlighted. In contrast to the synoptic evolution of the 2006 retraction, the event in 2017 was

initiated by a cyclonic disturbance that diverted the jet southward, versus Feature A in 2006, an

anticyclonic disturbance that first perturbed the jet northward. The subsequent development of

several high-amplitude anticyclonic anomalies along the poleward side of the jet was observed in

both cases, as was anticyclonic wave breaking within the 315-330 K isentropic layer in the east-

central Pacific.

Through expanded PTD, the processes contributing to zonal wind tendencies were

quantified for the initial perturbation of the jet in 2017. Upper-level vortex-vortex interactions

facilitated the initial retraction of the jet from 17-21 February 2017, in a manner similar to the

2006 case. The configuration of the upper-level QGPV anomalies, particularly the positive tilt

and dominance of negative QGPV anomalies north of the jet axis led to an situation in which

anomalous northerly flow between a ridge and a downstream trough advected *negative* QGPV

southward towards the jet. At the same time, southerly flow east of a trough advected negative

QGPV northward, producing a continuous region of negative QGPV advection and height rises.

A strikingly similar wave train configuration and impact on the zonal jet was found in both cases

(Fig. 3.9a compared to Fig. 4.6a).

The lifecycle of an LC1 breaking wave that developed during the 2017 retraction was

diagnosed using PTD, and it was found that the ridge's evolution was heavily governed by

deformation, as in the 2006 case. Some differences in the evolution between the two ridges are apparent, however, particularly the strong contribution from low-level vortex-vortex interactions in the 2017 case. This contribution to development arose from the fortuitous positioning of Feature A within a deformation region in the ϕ_i' height field, and the brief consolidation of A's circulation by the deformation region. The timing of the contributions to development from the QG terms led to rapid, steady growth in 2006, in contrast to the wavering, sporadic growth observed in the 2017 case. In the 2006 case, terms promoted growth simultaneously, while in 2017 deformation and the other terms were out of phase, leading to intermittent periods of growth.

Overall the results from these two cases suggests that some underlying physical similarities may characterize retractions of the north Pacific jet, particularly preexisting, large-scale deformation. It has been shown that retraction was initiated through regions of zonally-elongated, negative QGPV advection along the jet axis and jet exit region. The influence of non-linear advection on the low-frequency circulation is consistent with Hoskins et al. (1983), who showed how QGPV flux convergence can destroy or strengthen the background QGPV gradient and lead to changes in the zonal wind. One advantage to the approach employed here is that deceleration can be investigated instantaneously or in an aggregate sense, versus the time-mean perspective required by other diagnostics. The synoptic context in which non-linear vortex-vortex interactions act to promote retraction has been shown by virtue of considering both the transient and persistent influence of various QG processes on the zonal wind. New insight linking the tilt and position of a Rossby wave train with respect to the jet suggests there may a link between a forcing to retract the jet, nonlinear QGPV advection, and positively-tilted height anomalies.
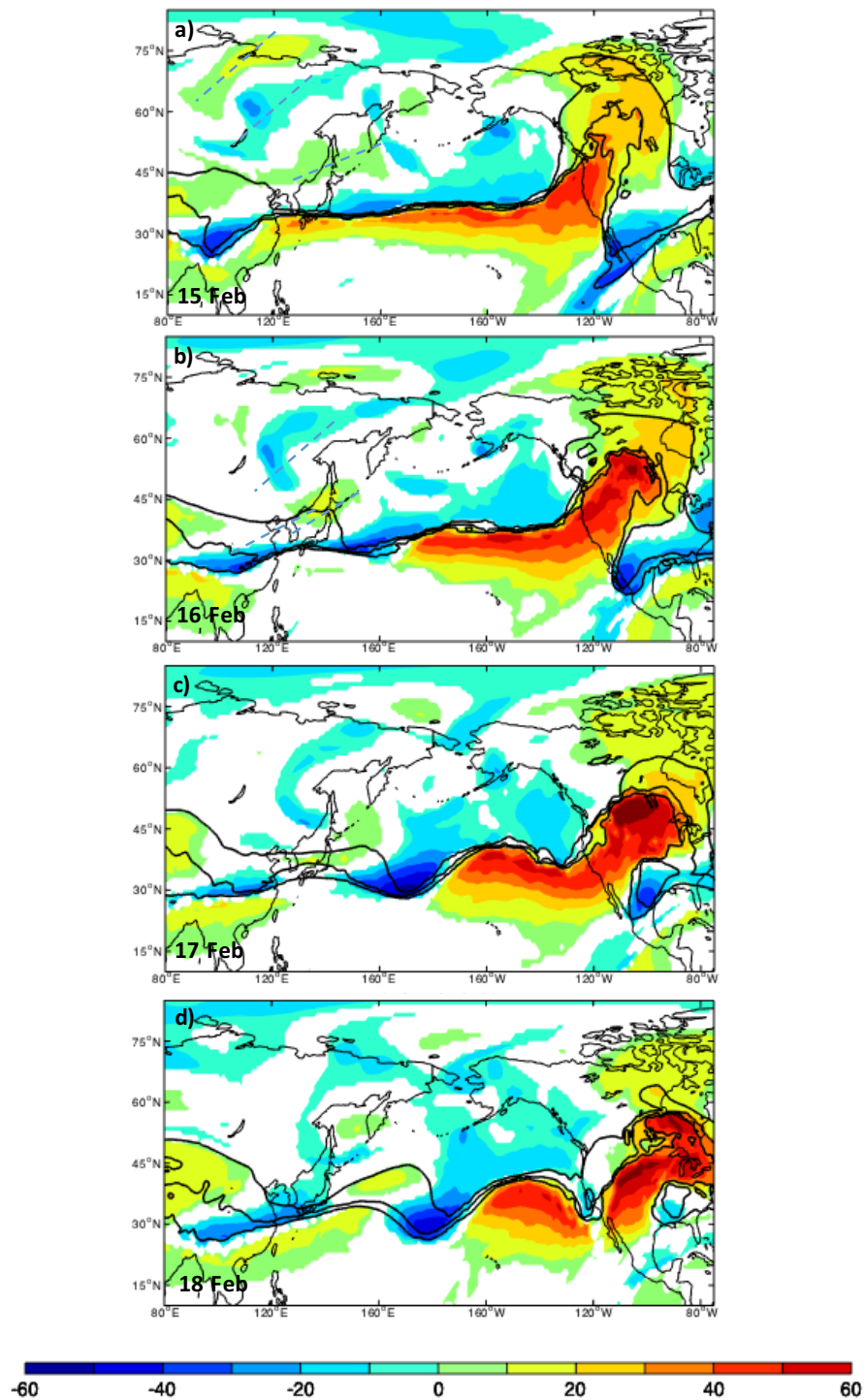
Figure 4.1: The color shading shows the potential temperature anomalies on the dynamic tropopause in Kelvin, with the 315, 330 and 345 K isentropic surfaces shown in black contours, for a) 15 February, b) 16 February, c) 17 February, and d) 18 February, 2017. Potential temperature anomalies of a magnitude less than 8 K are whited out. Light dashed lines in (a) and (b) indicate the tilt of a wave train originating over Siberia.
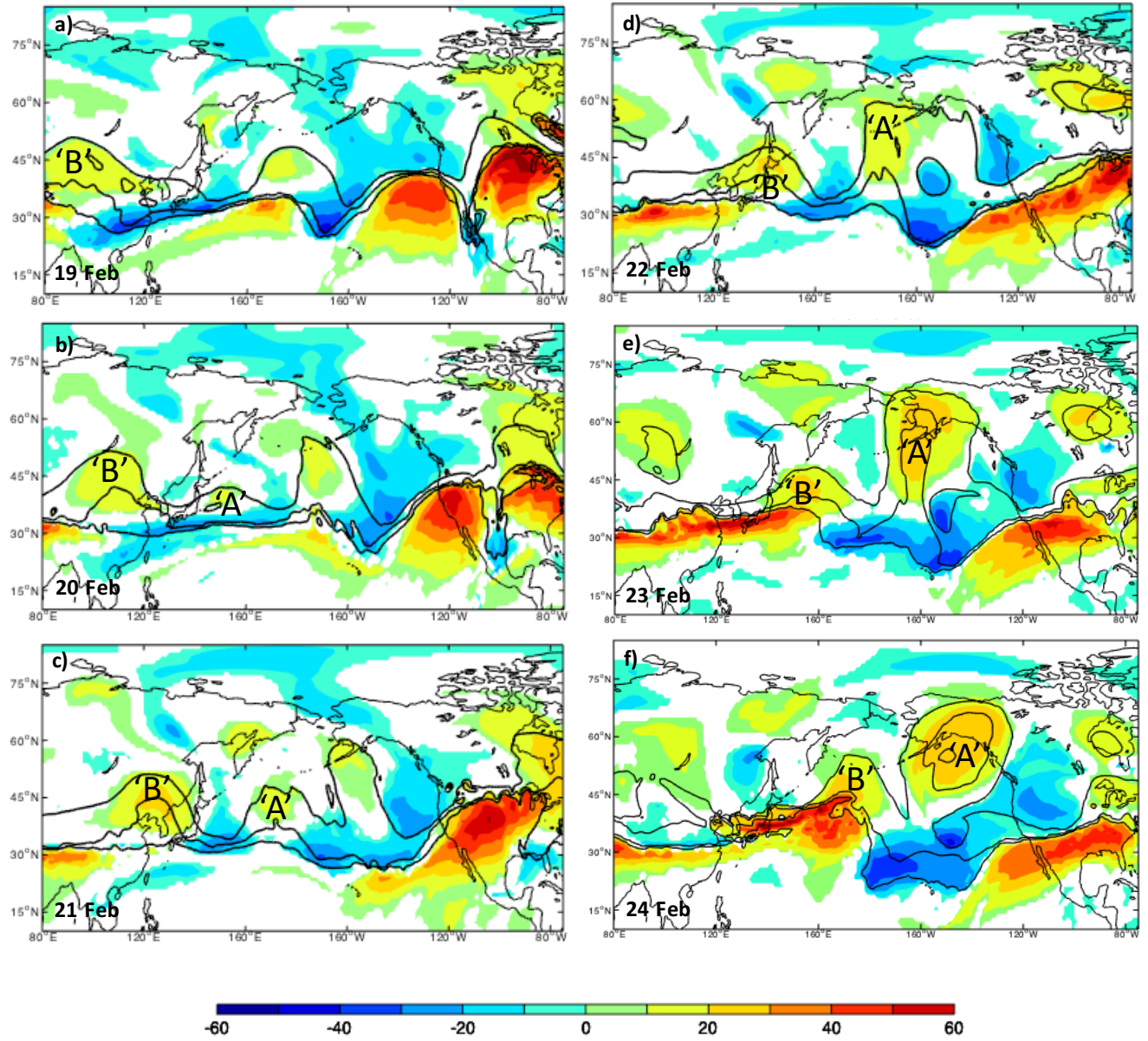
Figure 4.2: As in Fig. 4.1 but for a) 19 February, b) 20 February, c) 21 February, d) 22 February e) 23 Febuary and f) 24 February 2017. Two anticyclonic anomalies, 'A' and 'B' are labeled.
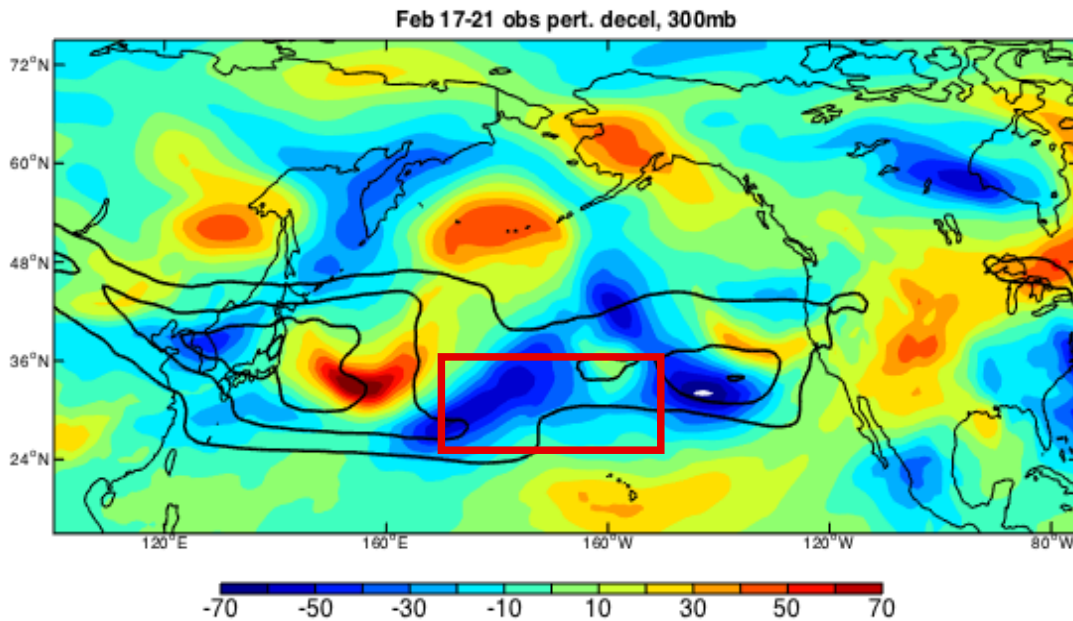
Figure 4.3: The color shading shows the February 17-21 2017 average zonal wind tendency of the 300 hPa zonal geostrophic wind in m s^{-1}, and the black contours show the average geostrophic zonal wind starting at 30 m s^{-1} every 10 m s^{-1}. The red box indicates the region over which retraction is investigated.

Height Field	Integrated Zonal Wind Tendency (m s^{-1})
Total Geopotential Height	-29.3010
Geopotential Height Anomalies	-28.8159
Upper Level QGPV Height Anomaly	-27.3436
Total PTD	**-28.0679**
Term A: Deformation/Superposition	-0.0031
Term B: Downstream Development	0.0455
Term C: Baroclinic Development	0.0172
Term D: Vortex-vortex UL	-22.4375
Term E: Vortex-vortex LL	-5.6900

Table 4.1: Integrated change in the zonal wind within boxed region in Fig. 4.3 from 00z 17 February – 18z 21 February 2017 using various height tendency fields.
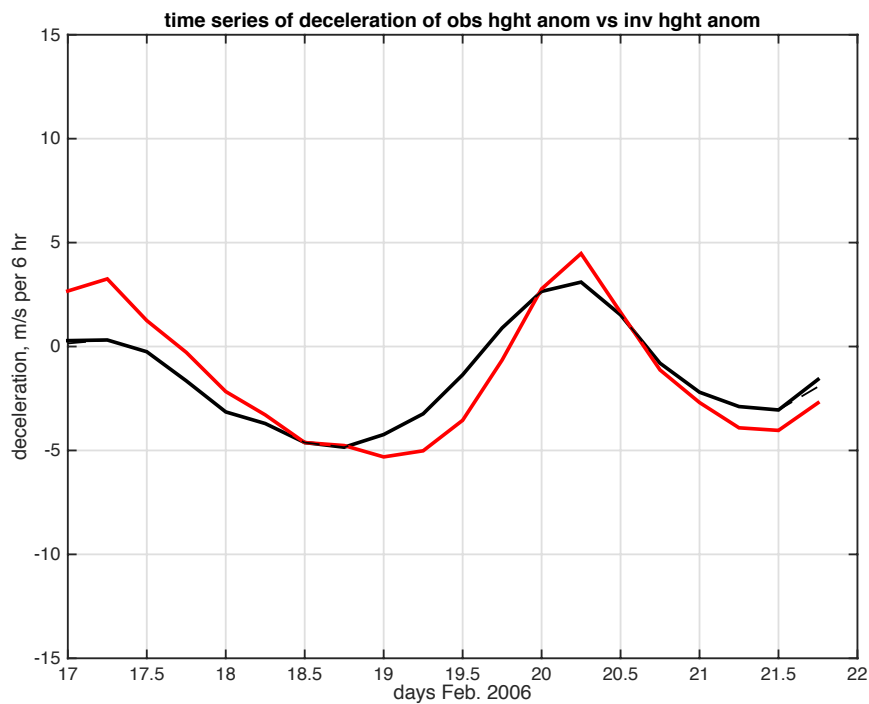
Figure 4.4: Time series of the zonal wind tendency with the box 25 – 35°N, 170 – 200°E, from 17-21 February 2017. The zonal wind change was calculated using the total height field (black line) and the sum of the QG height tendencies (red line, Eqn 3.6), in units of m s^{-1} (6hr)$^{-1}$.
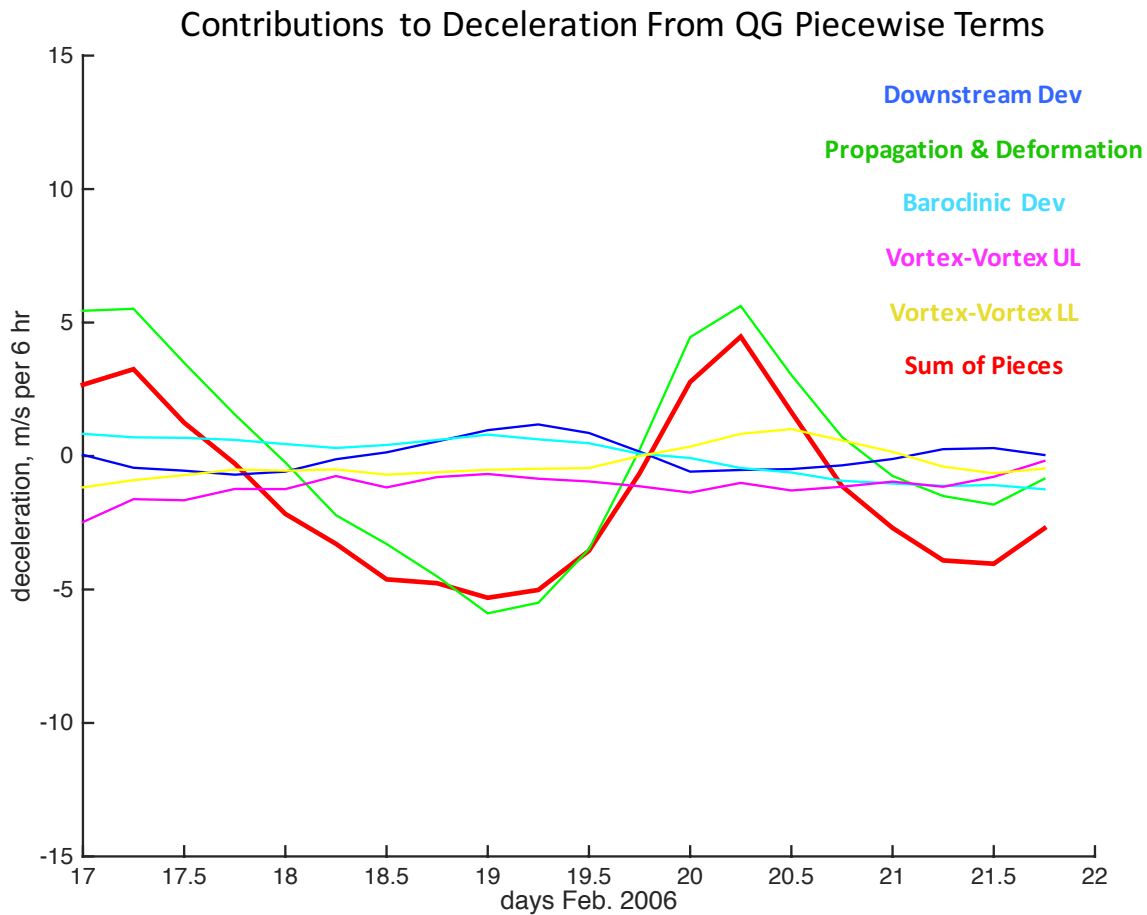
Figure 4.5: As in Figure 4.4 but for the wind tendency associated with the components in Eqn 3.6. The sum is the red line, Term A is in green, Term B in dark blue, Term C in light blue, Term D in magenta, and Term E in yellow.
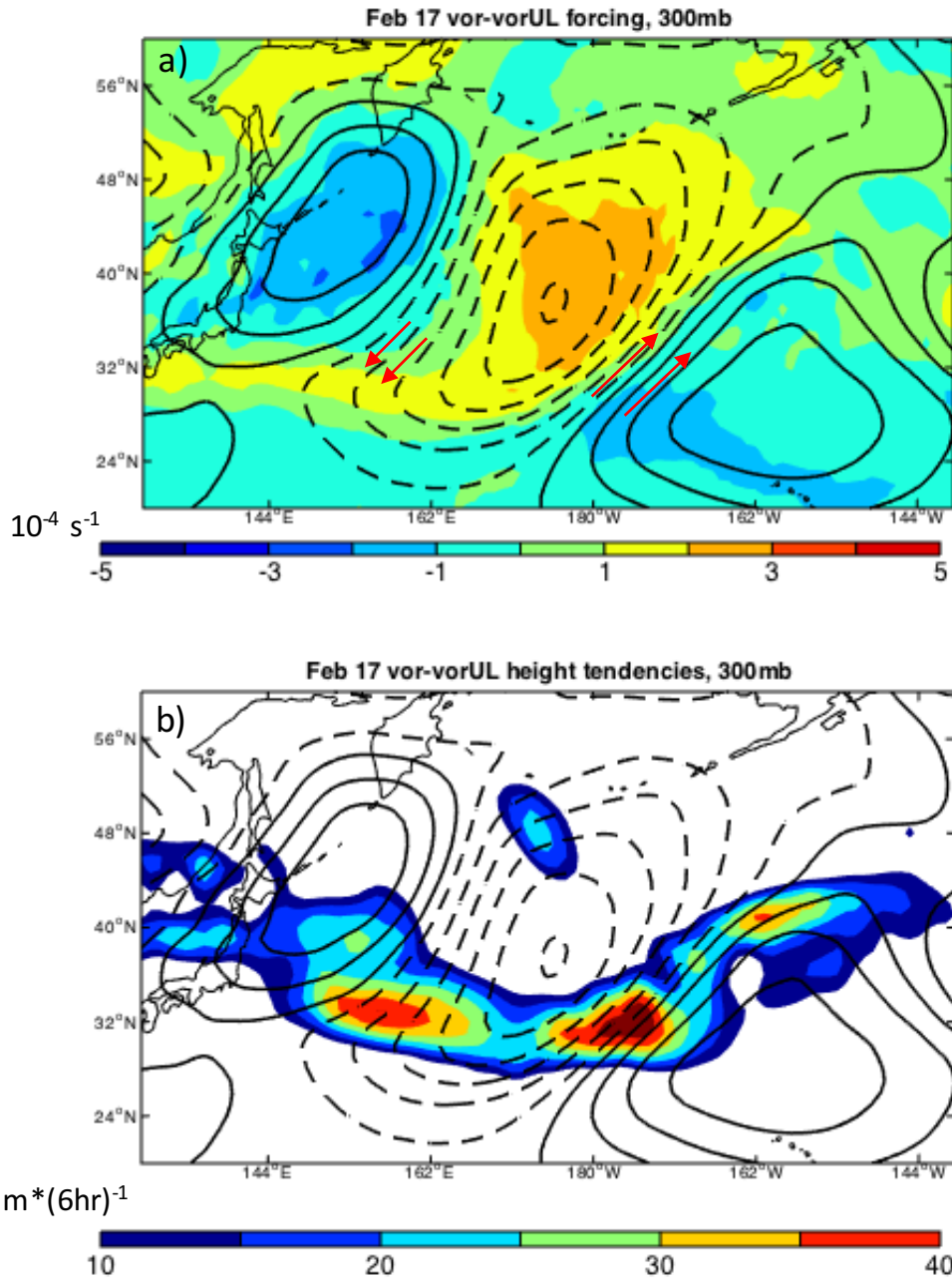
Figure 4.6: The color shading shows the 17 February 2017 average q'_u field in units of 10^{-4} s^{-1}. The black contours show the 17 February average ϕ'_u field, with positive (negative) values in solid (dashed) lines contoured starting at +/- 20 m every 50 m. b) The color shading shows the 17 February height tendencies associated with Term D and the forcing shown in (a). Height tendencies are in units m*(6hr)$^{-1}$, with positive values above 10 shown. The black contours are as in (a).

Feb 17 vor-vorUL decel, 300mb
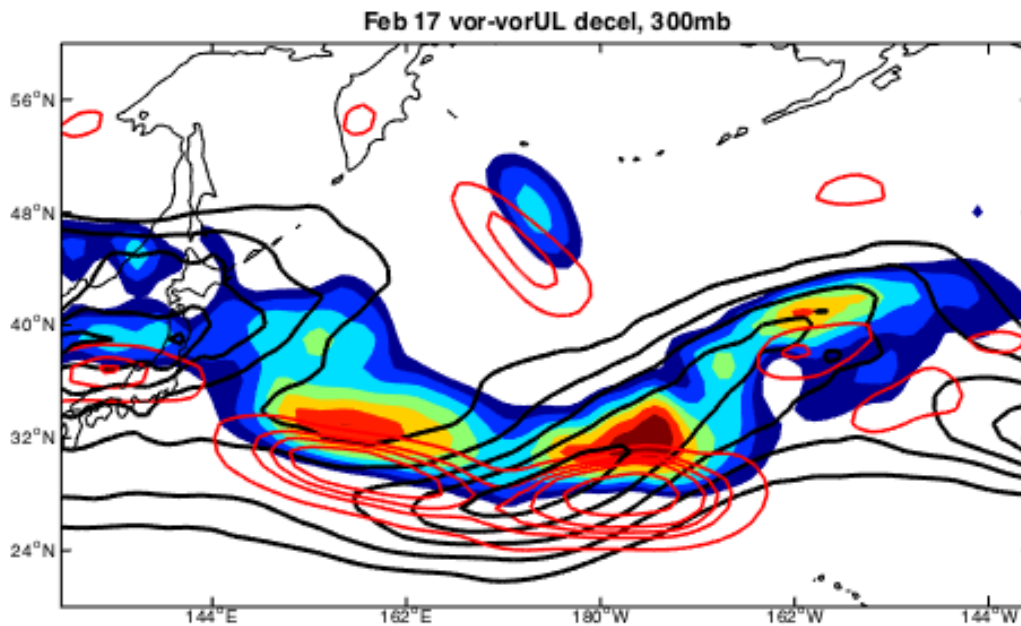
Figure 4.7: The color shading shows the 17 February mean height tendencies associated with Term D and the forcing shown in (Fig 4.6a). Height tendencies are in units $m*(6hr)^{-1}$, with positive values above 10 shown. The 17 February mean zonal isotachs starting at 30 m s^{-1} every 10 m s^{-1} are in the black contours. The 17 February 2017 mean change in wind speed associated with Term D (upper-level vortex-vortex interactions) is shown in the red contours, starting at -2 m s^{-1} every 2 m s^{-1}.
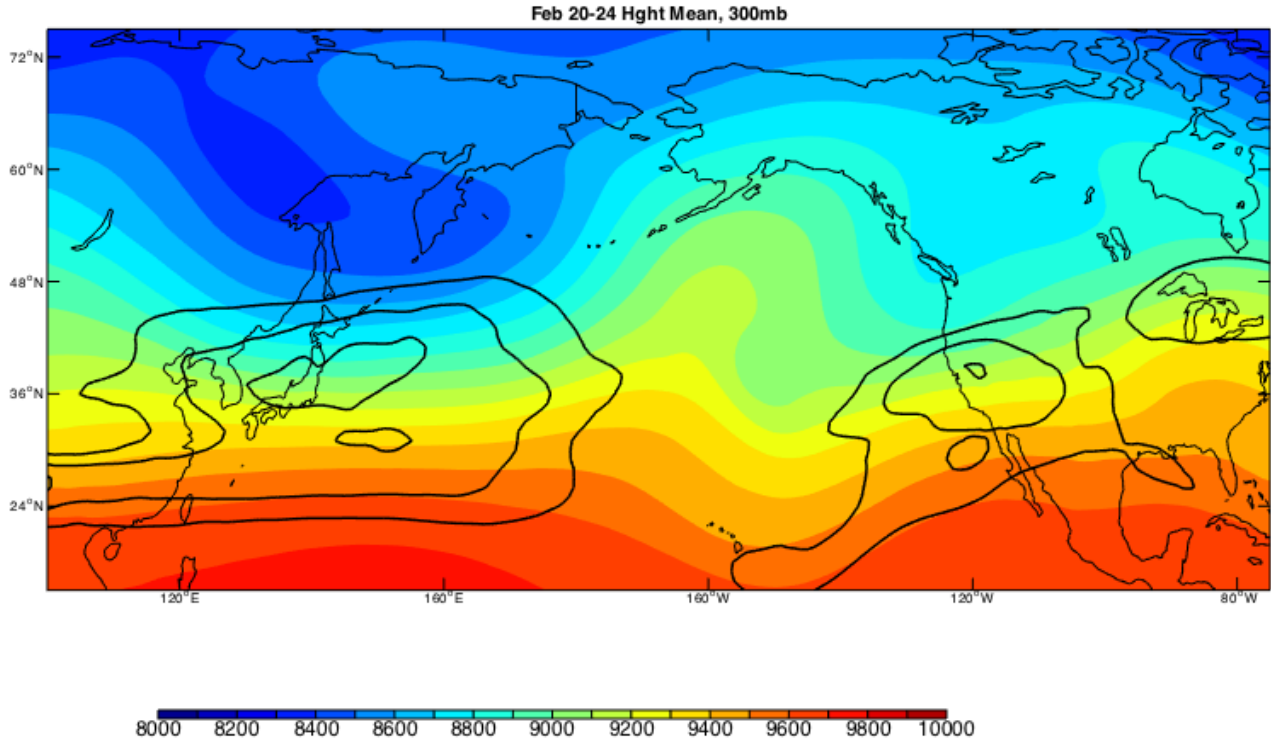
Figure 4.8: The color shading shows the 17-21 mean 300 hPa geopotential height, and the black contours show the 17-21 mean 300 hPa geostrophic isotachs starting at 30 m s^{-1} every 10 m s^{-1}.
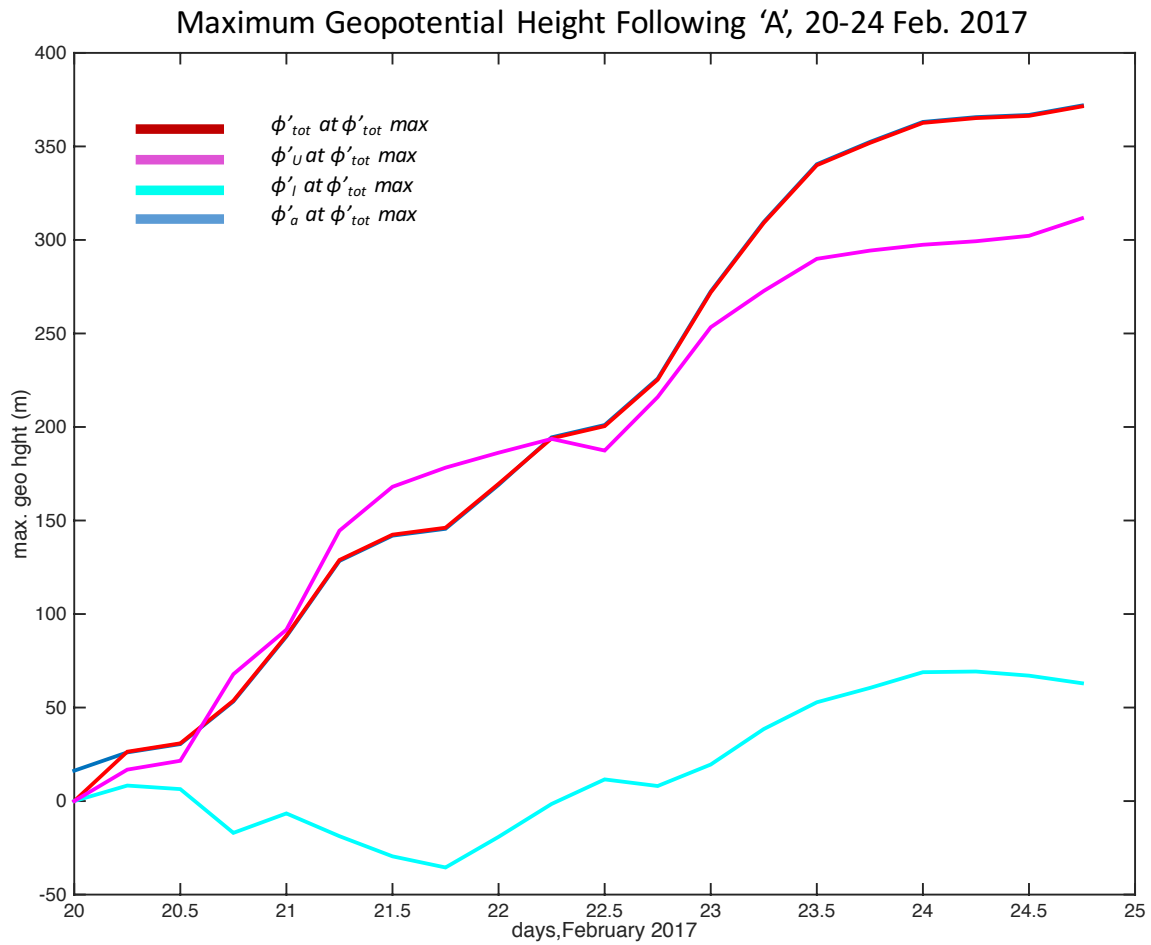
Figure 4.9: Time series of ϕ'_u (magenta), ϕ'_l (light blue), ϕ'_a (red) and ϕ'_{tot} (dark blue) following the height maximum associated with Feature 'A', from 20-24 February 2017.
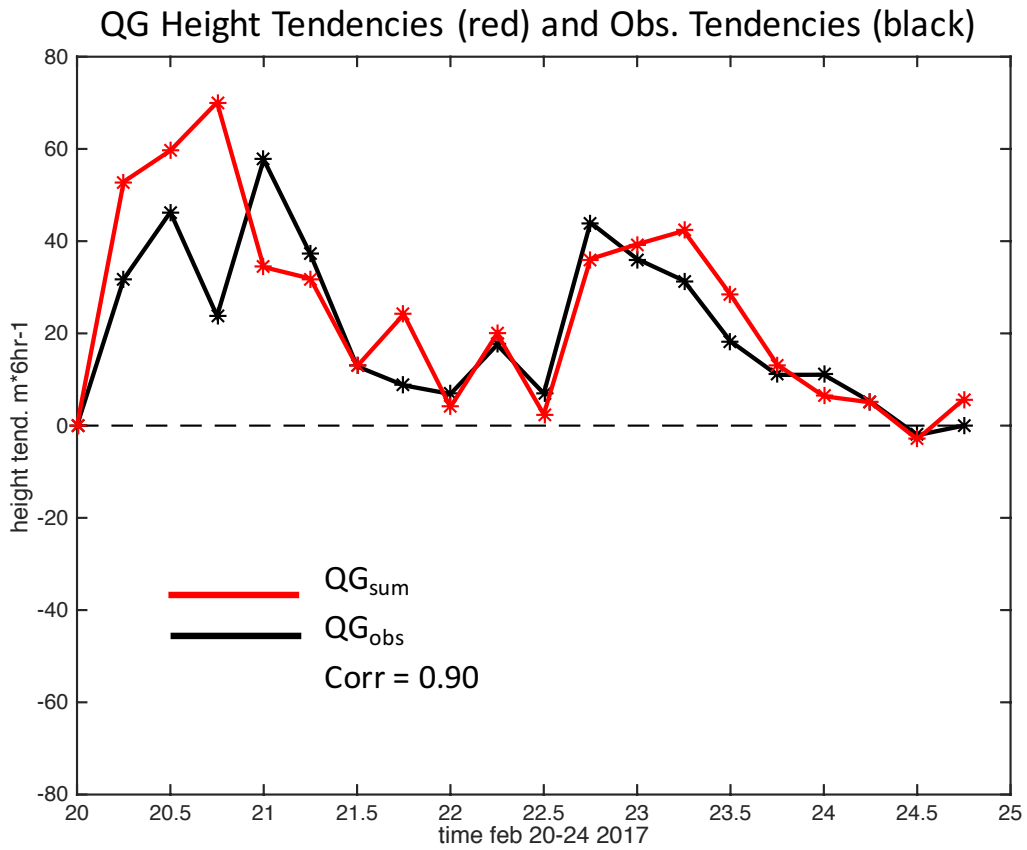
Figure 4.10: Time series of height tendencies following Feature 'A' calculated using the sum of the QG, piecewise terms (Eqn 2.6, red line) and using the centered finite difference of the ϕ'_u field (Eqn 2.8), from 20-24 February 2017.
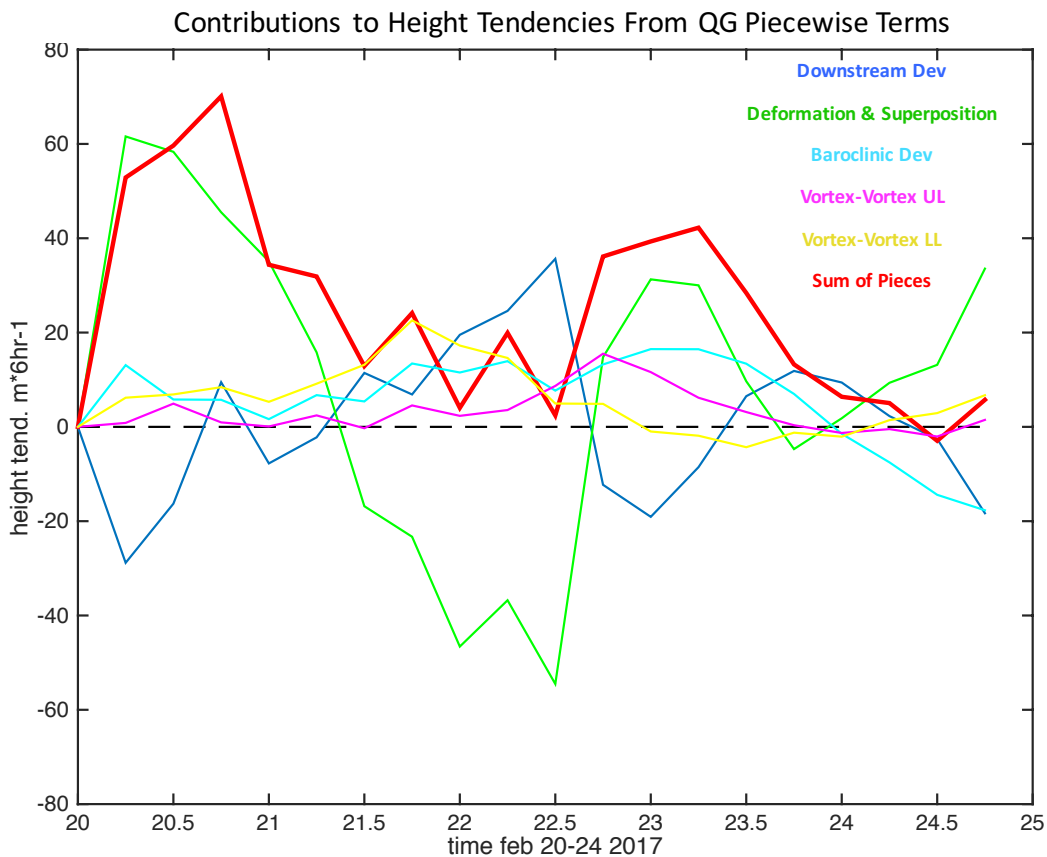
Figure 4.11: Time series of the piecewise terms in Eqn 2.6 from 20-24 February 2017. Term A (deformation/superposition) is in green, Term B (downstream development) is in dark blue, Term C (baroclinic development) is in light blue, Term D (upper-level vortex-vortex interactions) is in magenta, Term E (lower-level vortex-vortex interactions) is in yellow, and the sum of all terms is in red.
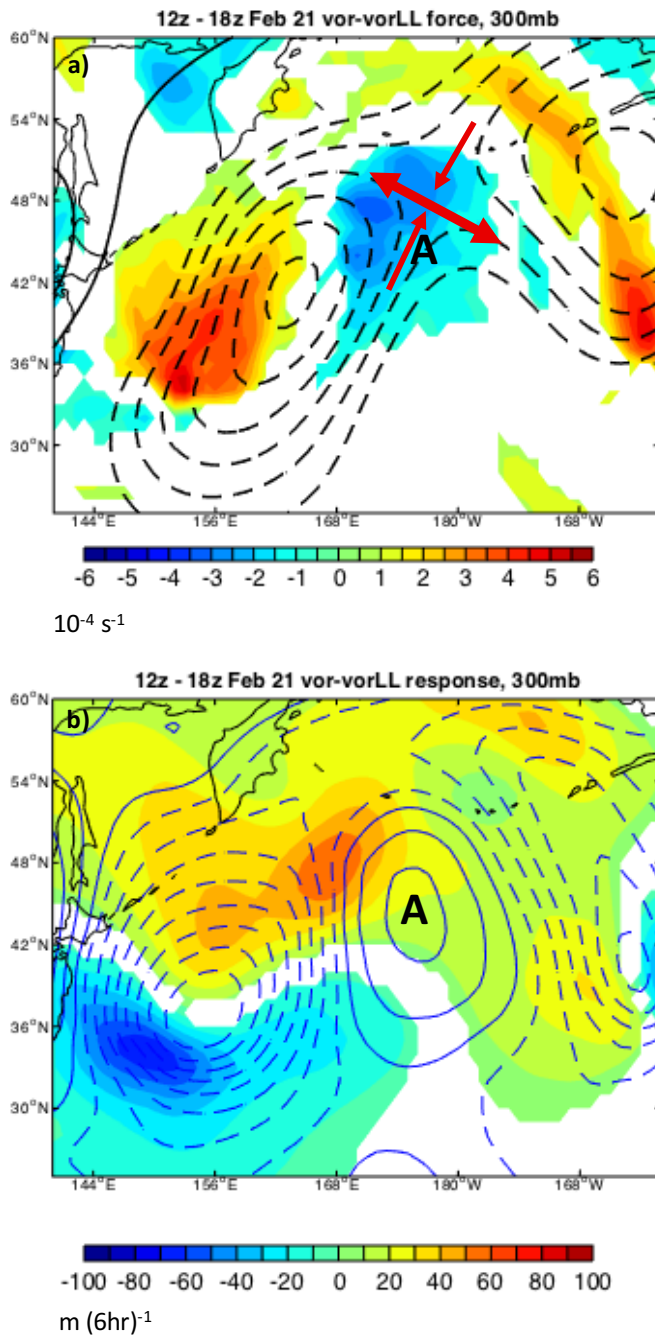
Figure 4.12: a) the color shading shows q'_u averaged from 12z-18z 21 February 2017, and the black contours show the ϕ'_l height field at 300 hPa, with solid(dashed) lines indicating positive(negative) values contoured starting at 10 m every 10 m. b) The color shading shows the height tendency field associated with Term E, in m (6hr)$^{-1}$. Values of +/- 5 m (6hr)$^{-1}$ whited out. The blue solid (dashed) contours show the positive (negative) ϕ'_{tot} height field at 300 hPa, starting at 20 m at an interval of 50 m. Feature 'A' is labeled.
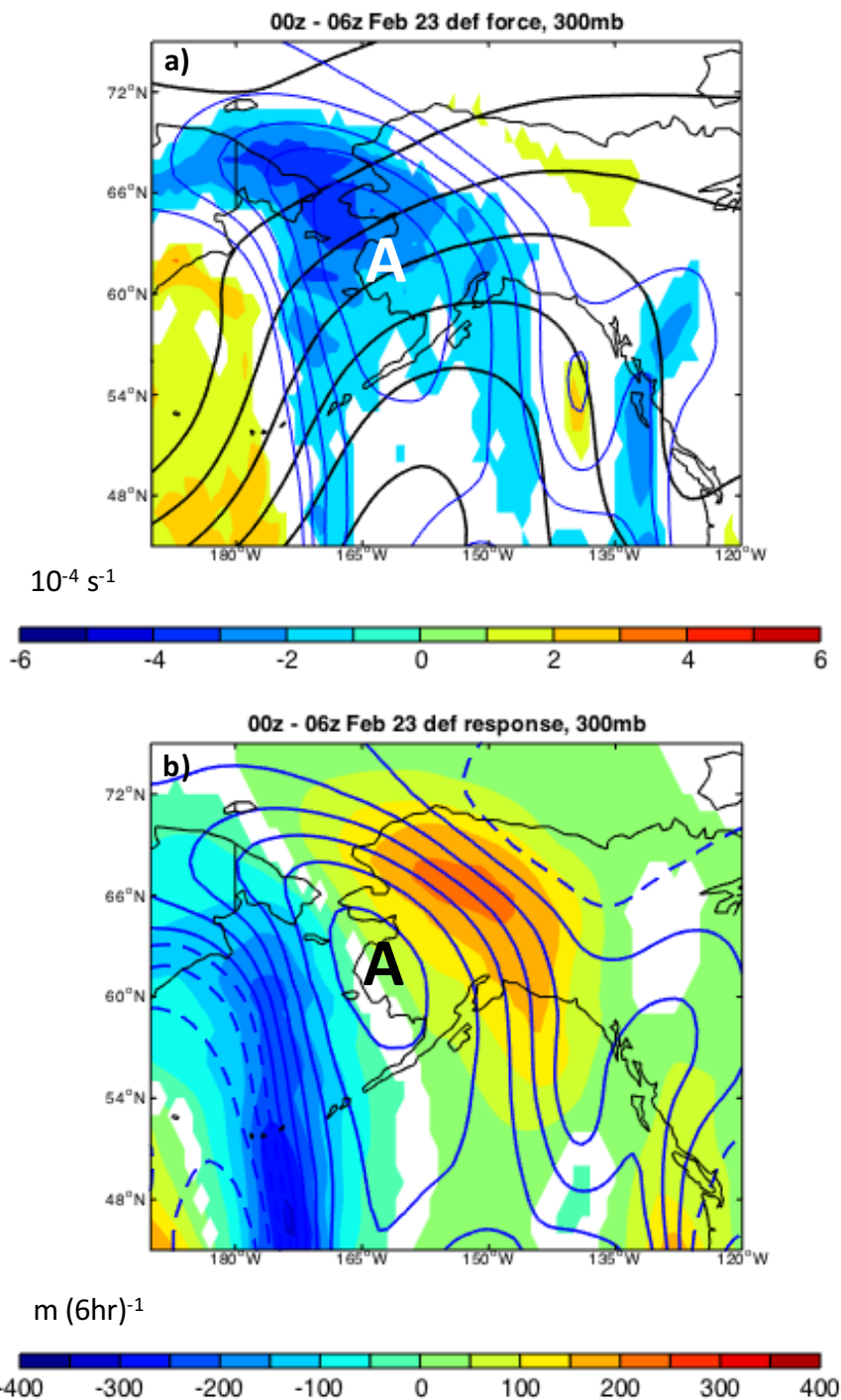
Figure 4.13: a) The color shading is as in Fig. 4.12a, but averaged from 00z – 06z 23 February 2017. The black contours show the 20-24 February mean geopotential height at 300 hPa, which can be used to approximate the background geostrophic wind. The blue contours show the ϕ'_{tot} field starting at +/- 20 m at an interval of 50 m. b) The blue contours as are in (a), and the color shading shows the height tendency values associated with Term A, deformation/superposition, averaged from 00z – 06z 23 February 2017.

CHAPTER 5: APPLYING A LINEAR INVERSE MODEL TO DIAGNOSE JET RETRACTIONS

The previous chapters have undertaken detailed case studies to identify the key

dynamical processes related to the onset of jet retractions. The role of the nonlinear advection of

low PV facilitated retraction in the two cases presented, while the height anomalies that

amplified during retraction were heavily influenced by mean state deformation. To complement

the enhanced dynamical understanding attained through synoptic diagnosis, a linear inverse

model (LIM) will be used to determine what aspects of the circulation are associated with the

most rapid growth into a retracted state. A LIM is an empirical model that describes the

dynamics of a system from its lagged covariance statistics. With a LIM it is possible to

determine the 'optimal initial conditions' that most rapidly evolve into a prescribed final state,

such as a jet retraction. In this way the features routinely observed in synoptic analysis can be

compared to the optimal initial structures identified by the LIM, to distinguish features that

might commonly precede retraction, from those that are more specific to a particular case.

Another advantage to LIM is that initial optimal structures can be determined for a variety of

lead times that extends beyond the numerical weather prediction limit of two weeks, suggesting a

LIM might be a way to fill the so-called 'forecast gap' of the 2-4 week range.

5.1. Introduction

Atmospheric blocking represents periods during which the mean jet is diverted around

the circulation of a persistent, large-scale anticyclone, often accompanied by cyclones to the

south (Rex block) or flanking it on either side (omega block). Owing to their upstream and

downstream influences on the circulation, blocks dramatically modify the precipitation and

temperature distribution experienced regionally (Rothlisberger et al. 2016). Consensus has not

been reached regarding the details of common blocking initiation and maintenance mechanisms, although many theories are rooted in explaining how the flux of negative PV into one region for a prolonged period of time can occur. In addition to remaining a stubbornly elusive phenomenon to understand dynamically, predicting the onset of midlatitude blocking is a well-known forecast challenge (Legras and Ghil (1985); Tibaldi et al. 1994; Colucci and Baumhefner 1998; Matsueda et al. 2011).

Renwick and Wallace (1996) showed that the 500hPa geopotential height pattern associated with greatest root-mean-square error in the ECMWF model, in the north Pacific sector, was a midlatitude block (Figure 5.1). Matsueda et al. (2011) compared the skill of the Canadian Meteorological Center (CMC), Japan Meteorological Agency (JMA), and National Centers for Environmental Prediction (NCEP), forecasts of a block that developed over the Rocky Mountains in December 2005. They initialized all models five days prior to blocking onset, and found that the NCEP model failed to accurately forecast the location of the block. In contrast, the CMC and JMA models were able to predict the blocking location. They found that the NCEP model's blocking forecast was sensitive to the evolution of a cutoff cyclone located in the central north Pacific, which was generating uncertainty in the ensemble members. Gaining better understanding of these deficiencies in model forecasts of the breakdown of the westerlies into blocked flow is an important aim of ongoing research. One issue, however is that operational numerical weather prediction models have an untenable number of degrees of freedom, complicating the task of pinpointing the source of model error.

Penland and Sardeshmukh (1995) introduced a framework for linear inverse modeling (LIM), in which the dynamics of a stable, linear system forced by stochastic white noise are inferred through the statistics of the system. The dynamics of the system are determined using

the lagged covariance of the system at one well-chosen lag; then, new forecasts at any time range can be made. Penland and Sardeshmukh (1995) found that, despite the requirement that the dynamics of the system be damped in the long-term, monthly-mean tropical sea surface temperature anomalies could grow via modal interference for as long as 15 months. Vimont (2012) used an SST-based LIM and optimized growth into the pattern associated with the Atlantic Meridional Mode (AMM), to test various theories regarding AMM initiation and showed that the AMM resembled the second fastest growing 'energy' or L2 norm.

Winkler et al. (2001) developed a LIM to forecast low-frequency (10-30 day) midlatitude variability using a system composed of only tropical heating and midlatitude stream function at 750 and 200 hPa. Their LIM was competitive with the skill of the NCEP Medium-Range Forecast model at the two-week forecast range for the December-February winters from 1996-1997 – 1999-2000. In addition to optimizing growth in a given pattern of interest, it is possible to remove specific interactions in the LIM, for instance, the impact of tropical heating on the midlatitude stream function, and investigate how removing that interaction modifies the evolution of the system. Using a LIM also has the advantage of reducing the NWP problem to a manageable number of possible sources of error, without sacrificing too much prediction skill, while remaining computationally inexpensive. Given the previously demonstrated efficacy of using a LIM to forecast midlatitude circulation patterns, a LIM is employed in this chapter to determine the circulation features that most rapidly grow into a retracted state.

5.2 Methodology

This study uses output from the National Centers for Environmental Predication National Center on Atmospheric Research (NCEP-NCAR) Reanalysis I dataset at 2x2° spatial resolution from December 1979 – February 2014. 200 and 850 hPa streamfunction anomalies were

calculated from 7-day running mean wind anomalies. For the blocking criteria that will be discussed in section 5.3, streamfunction anomalies were standardized with respect to the 1979-2014 standard deviation at each grid point. Outgoing longwave radiation was attained from the daily interpolated OLR from NCEP/NCAR.

5.2.1 Constructing the Linear Inverse Model

A linear inverse model (LIM) is an empirical model that infers the dynamics of a system from its lagged covariance statistics. Linear relationships, as well as a linear approximation to nonlinear dynamics, are captured in the covariance. First, a state vector x representing the system is defined as the deviation with respect to a climatological average $x = X - \bar{x}$, and the evolution of the state vector can be expressed as follows:

$$\frac{dx}{dt} = Bx + N(x) \qquad (5.1)$$

Where $\mathbf{B}$ is the linearized component of the dynamical equations and $\mathbf{N}(\mathbf{x})$ represents the nonlinear component. It is often possible to approximate the nonlinear terms as a second order linear process plus 'noise':

$$\frac{dx}{dt} = Lx + F_s \qquad (5.2)$$

where $\mathbf{L}$ includes linear dynamics *and* a linear approximation of nonlinearities, and $\mathbf{F_s}$ represents stochastic noise forcing. Solving the homogeneous system yields

$$x(t + \tau) = \exp(L\tau)\,x(t) = G(\tau)x(t) \qquad (5.3)$$

Where $\mathbf{G}$ is the Green's function that can be estimated using the instantaneous and lagged covariance matrices of the state vector. $\mathbf{G}$ can be estimated using the covariance matrices of the system at zero and τ_o lags (Eqn. 5.4). The choice of τ_o is a crucial step in constructing an effective model, as it determines the timescale over which dynamical relationships within the model will be captured.

$$G(\tau_o) = C_{\tau_o} C_o^{-1} \qquad (5.4)$$

$$L = ln(G)/\tau_o \qquad (5.5)$$

From there, the dynamical system operator L is derived from the Green's function by taking the matrix logarithm of G divided by τ_o (Eqn 5.5). The dynamical operator L is determined using a fixed lagged covariance matrix via τ_o, but that same operator can be used to determine optimal growth structures at varying lag, denoted by τ, within the limits of when the model remains sufficiently represented as linear, stable system. This is done by computing a new Green's function using L, once L has been determined using τ_o. The τ_o chosen in the present study is seven days, and tests for the validity of this choice are presented in the following sub-section.

The state vector for the LIM used in the present study is defined as

$$x = [\text{OLR} \quad \Psi_{850} \quad \Psi_{200}] \qquad (5.6)$$

where OLR represents anomalous outgoing longwave radiation from 20°S to 20°N, Ψ_{850} and Ψ_{200} represent 850hPa/200hPa midlatitude stream function anomalies from 20-90°N. All variables are included from 0-360° longitude, and have been temporally smoothed with a 7-day running mean boxcar filter. Empirical orthogonal function analysis (EOF) is applied to the anomaly fields individually to reduce the dimensions of the state vector. Enough 200hPa and 850hPa stream function EOFs are retained in each field to account for 80% of the total variance. The 20 leading OLR anomalies are retained, explaining 60% of the total tropical OLR variance; each additional EOF contributed less than 1% to the total variance, suggesting they are less crucial in understanding large-scale OLR variability.

5.2.2 Testing the LIM

To determine whether the dynamics of the system as represented by L are independent of τ_o, which would be the case for a perfectly linear system, the τ test after Penland and

Sardeshmukh (1995) was performed. The dynamical operator L is calculated using a range of lags, and the Euclidean norms of L and its submatrices were then computed. Penland and Sardeshmukh (1995) first demonstrated that when the norms of the submatrices are constant with varying lag τ_o, the dynamics of the system as represented by L are independent of the τ_o chosen to define it. The norm of L and its submatrices in this model are shown in Figure 5.2 for a range of lags. It is confirmed that for a τ_o from 2-8 days the dynamics are not sensitive to the lag chosen, while a lag of 9 days leads to a dramatic change in the dynamics. For the τ_o of seven days that we employ, it is concluded that the assumption of linearity holds sufficiently well.

An additional test may be used to verify that L is independent of τ_o wherein the G computed for various lags is compared. Winkler et al. (2001) demonstrated how it is possible to compare the autocovariance determined by the LIM using τ_o (i.e., $[(G(\tau_o)]^\tau /\tau_o * C(0)$) with that predicted by multiple linear regression $[G(\tau)C(0)]$. The trace of these two autocovariance formulations is shown in Figure 5.3 for a range of τ from 0 to 20 days. The trace has been normalized to a value of one at zero lag as in Winkler et al 2001. If the system is truly linear, the two autocovariance functions should be similar, and it is found that for this LIM and lag chosen, the two are indeed similar for both tropical OLR and midlatitude stream function. Based on these two tests, the choice of τ_o as seven days is within the range for which the dynamics of the system are deemed sufficiently linear.

The approximation of the system using Eqn (5.2) is based upon a presumed balance between the impacts of the dynamics of the system and stochastic white noise on the overall variance in the system. Assuming stationary statistics (ie, that the covariance of the system is constant in time), the fluctuation-dissipation relationship indicates that dynamics of the system will reduce variance with time, while the tendency of stochastic noise is to enhance the variance

with time (Eqn 5.7). To test that the variance of the system behaves according to this

assumption, the noise covariance matrix, **Q**, is determined via using L derived from a τ_o of seven

days (Eqn 5.7). The eigenvalues of **Q** must be positive to coincide with growth of the

covariance of the system against the long-term damping caused by the dynamics. In this case,

two of the eigenvalues of **Q** are negative. However, whether these eigenvalues have first-order

effects on the covariance of the system can be determined by recomputing C_0 using a modified **Q**

that has the negative eigenvalues removed. Performing this calculation shows that the two

negative eigenvalues of **Q** do not change greatly the eigenvalues of C_0, or the percent variance

explained by the leading eigenvalues. This test indicates that the impact of the negative

eigenvalues of **Q** upon the system overall is not a first-order influence. While there is indeed

some reduction in the amplitude and variance explained by the first EOF, it is still extremely

distinct from the other modes and maintains a similar variance of the total system, even with a

modified **Q** (Figure 5.4).

$$\frac{DC0}{Dt} = 0 = LC_o - C_oL' + Q \qquad\qquad 5.7$$

One final test to confirm the LIM is an appropriate model to use for the dynamical system

defined in the state vector, is to evaluate if error in the model evolves in a manner consistent with

theory. Figure 5.5 shows the observed error in the LIM as a function of forecast lead time,

which is compared with the error predicted by theory, persistence, and a first-order

autoregressive (AR(1)) process. While the observed error in the LIM is higher than theory

predicts, it is lower than both persistence and AR(1) by a substantial amount. It is thus

determined that the error growth in the model is consistent with theory, the assumption of stable,

linear dynamics as determined by the tau-test is a suitable approximation to the dynamics of the

system as captured by the state vector and the lagged covariance statistics. The requirements for

successful implementation of the LIM as outlined by Penland and Sardeshmukh (1995) are thus

met.

5.3 Defining a retraction norm

While in the long-term the empirical normal models (ENMs) of L are damped, so that

without any external noise forcing the energy of the system eventually decays, a limited period

of transient growth is possible in the short-term if the normal modes of L are not orthogonal. In

other words, interactions between the ENMs in the short term can lead to a finite period of

growth of the system without forcing from white noise (Penland and Sardeshmukh 1995). The

growth $\mu(\tau)$ over any interval may be calculated via:

$$\mu(\tau) = \frac{\{x(\tau)'Nx(\tau)\}}{\{x(0)'Fx(0)\}} = \frac{\{x(0)' \cdot G(\tau)'NG(\tau)x(0)\}}{\{x(0)'Fx(0)\}} \qquad 5.7$$

Where **N** and **F** represent initial or final norm kernels that can be specified for a variety

of situations. Under the Euclidean, or 'L2' norm, **N** and **F** are the identity matrix, in which case

the growth of the system can be determined by solving the eigenvalue problem (Eqn 5.9; Farrell

1988; Penland and Sardeshmukh 1995; Tziperman and Iannou 2002; Vimont 2012). Otherwise

an initial or final norm may be specified, and in this study a final retraction norm will be

implemented (5.10).

$$(G(\tau)'G(\tau))v(\tau) = \mu(\tau)v(\tau) \qquad 5.9$$

$$(G(\tau)'NG(\tau))v(\tau) = \mu(\tau)Fv(\tau) \qquad 5.10$$

The eigenvector $v(\tau)$ corresponds to the initial condition that produces growth that is

equivalent to the growth captured by the eigenvalue $\mu(\tau)$ over the time interval τ. The

eigenvalue corresponding to the strongest growth over this time frame can thus be identified.

The corresponding structures of the eigenvector $v(\tau)$ can then be examined and are referred to as

the 'optimal' structures that produce the strongest growth under a particular norm (Farrell 1988;

Vimont 2012). In this way, a norm defined using a prescribed atmospheric pattern, such as one that is associated with jet retractions or blocks, can be used instead of the Euclidean norm. In the present study a final norm **N** is defined based upon the 200 and 850 hPa stream function pattern associated with jet retractions.

A wind-speed based criteria is employed to identify retractions during boreal winter (December – February) from 1979 - 2014. Using unstandardized 200 hPa stream function anomalies, the rotational component of the anomalous zonal wind was calculated as such: $u'_\psi = -d\psi'/dy$. Zonal wind anomalies were standardized with respect to the standard deviation at each grid point. The resultant standardized zonal wind anomalies were averaged in the same region as used by Jaffe et al. (2011) to track retractions, 25-40°N 180-200°E, and when the average wind speed anomalies in that region were less than 1.25 standard deviations below climatology for at least five days, a retraction event was identified. Using this criteria, a total of 27 independent events lasting a total of 382 days were identified, corresponding to 11.8% of all days being characterized by a retracted state.

The composite irrotational zonal wind and streamfunction anomalies at the day of retraction onset, Day 0, are shown in Fig. 5.6. In accordance with the retraction definition employed, the zonal wind is weaker than average along the jet axis from 140°E to 140°W, and this reduction in wind speed is associated with stronger than average zonal wind speeds to the north and south at 55°N and 10°N. The associated 200 hPa stream function anomalies are characterized by an anticyclone in the midlatitudes and an equally potent and sprawling cyclonic anomaly to its south in the subtropics. Figure 5.7a shows the climatological distribution of tropopause pressure for the entire analysis period. Where the meridional pressure gradient is strong, such as in the western Pacific, the tropopause slopes rapidly in altitude, reflecting the

climatological position of the north Pacific jet. In the east Pacific the gradient becomes more diffuse, indicating the typical location of the jet exit region. The composite tropopause pressure gradient at Day 0 is far more diffuse in the central Pacific than climatology, reflecting a westward confinement of the jet core as represented by the tropopause pressure gradient. Only a region over Japan in the western Pacific is characterized by a stronger tropopause pressure gradient and, presumably, stronger wind speeds.

Before using the retraction structure as a norm for the LIM, it is prudent to first investigate the 'observed' transition to retraction as represented in the NCEP/NCAR R1 dataset to determine what features are associated with retraction in reality. The composite evolution of 200 and 850 hPa midlatitude stream function and tropical OLR anomalies before, during and following retraction onset is shown in Figs 5.8-5.10. Ten days before retraction onset there is no significant pattern in the stream function fields, except a barely-distinguishable cyclonic feature at 200 hPa near 70°N, 80°E (Fig. 5.8a-b). Five days later a cyclonic 200 hPa feature over Siberia is still observed, now located farther to the east and more isotropic in shape (Fig. 5.8c). In the eastern Pacific a positive stream function anomaly at both 200 and 850 hPa is also observed at this time, and at 200 hPa two cyclonic features in the subtropics have also developed (Fig.5.8c-d). By the onset of retraction, the sprawling midlatitude anticyclone and subtropical trough have developed at 200 hPa, accompanied by the development of a strong, sprawling midlatitude anticyclone at 850 hPa (Fig. 5.8e-f). The vertical structure of the atmosphere at this time is equivalent barotropic.

Five days after retraction begins, the flow pattern in the central Pacific has amplified and remained relatively stationary, and at 200 hPa a trough and ridge have developed over North America, characteristic of the negative PNA pattern (Fig. 5.9a-b). A 200hPa anticyclone

centered over India has amplified as well. Ten days after retraction onset, the column-deep

midlatitude anticyclone persists, although it has weakened in magnitude at both levels. The

subtropical trough at 200 hPa remains stronger than the anticyclone, as it has throughout the

composite evolution (Fig. 5.9c-d). A trough-like feature over northwestern Canada remains,

while the anticyclone over the southeastern United States is no longer observed. Finally, 15 days

after retraction onset, only the remnants of the previously strong dipole-type block are observed

at 200 hPa, and at 850 hPa only a small anticyclonic anomaly remains (Fig. 5.9e-f).

The composite evolution of OLR, a proxy for tropical convection, over the same 25-day

time period is shown in Figure 5.10. Negative OLR anomalies indicate cloudiness and

convection, while positive OLR anomalies indicate clear skies and suppressed convection. Ten

days prior to retraction onset there is barely any OLR signal except a region of reduced OLR

collocated with the small 200 hPa trough observed over Siberia at this time (Fig. 5.10a/5.8a). At

Day - 5 this region of reduced OLR has grown spatially and is in the same location as the 200

hPa trough; meanwhile a region of enhanced OLR is observed near the Equator from 160-180°E.

A small region of reduced OLR is located in the subtropical central Pacific northwest of Hawaii,

located near the 200 hPa trough observed at this time (Fig. 5.10b/Fig. 5.8b). By the onset of

retraction many OLR features emerge, with enhanced OLR observed to the south of the

subtropical 200 hPa trough, and reduced OLR observed to the north of the trough (Fig. 5.10c). A

region of reduced OLR has developed over the Indian ocean as well. By Day + 5, the region of

reduced OLR strengthened and moved eastward, while a quasi-linear region of enhanced OLR is

observed in a northwest-southeast orientation from 20°N to 20°S and 120°E to 100°W (Fig.

5.10d). The region of reduced OLR over the tropical Indian ocean is more spatially expansive at

this time, but slightly weaker in magnitude. At Day + 10, the reduced OLR observed in the

subtropics persists and has not moved or weakened substantially, and is located east of the

subtropical trough observed at 200 hPa (Fig. 5.10e/Fib5.9b). In the tropics south of the reduced

OLR is a region of enhanced OLR, although it is weaker and less spatially expansive. Finally,

fifteen days following retraction onset only the enhanced tropical OLR is observed in the north

Pacific, while a region of reduced OLR lingers over northwestern Canada.

5.3.1   *Optimal Initial Structures Under a Retraction Norm*

The composite 200 and 850 hPa stream function patterns at Day 0 are used to define the

norm, **N**, towards which growth is optimized. Only the dipole of stream function in the central

Pacific was included in the norm, and any remaining structures were eliminated to ensure the

LIM only maximizes growth in the direction of the pattern directly associated with the weakened

zonal wind in the central Pacific. First, the 200/850hPa streamfunction patterns associated with

retraction are projected onto the spatial patterns of the EOFs of 200/850 hPa stream function in

the state vector. Then, the corresponding projections were divided by their norm. For the

present analysis, an optimization interval of ten days was used to identify the 'optimal' initial

structures that most rapidly amplify into the retraction pattern. A ten day optimization interval

was used because it coincides with the interval that experiences the most growth into the

retraction norm (Fig. 5.14). Figure 5.11 shows the 200 hPa initial and evolved structures

identified by the LIM under a retraction norm, using Eqns 5.7-5.8. Similar to the 200 hPa

composite evolution at Day -5, a preexisting midlatitude ridge in the eastern Pacific, and a trough

to its south, are present in the optimal. Over eastern Europe and Asia, an anticyclonic anomaly is

observed in the midlatitudes, which was not observed in the composite retraction evolution in

Fig. 5.8, *but* is in the location of Feature B discussed in the 2006 and 2017 case studies of

retractions. Furthermore, a negative PV anomaly was observed in the composite analysis of

Jaffe et al (2011) in a similar location as the anticyclonic feature identified in the optimal (Fig. 1.8b). The final evolved retraction pattern has many similarities to the Day+5 200 hPa stream function pattern (Fig. 5.11b/Fig. 5.9b).

Turning attention to the 850 hPa stream function evolution, the optimal initial structure is characterized by a weak anticyclone located in the central Pacific, which appears to simply amplify in place over the ten-day optimization interval (Fig. 5.12a). Upstream and downstream of the anticyclonic anomaly are weak cyclonic anomalies, with a particularly spatially expansive feature observed over Russia and China. A low-level trough over the far eastern Pacific/western North America is also present in the optimal. The two troughs at 850 hPa are both located beneath anticyclonic features at 200 hPa, indicating the optimal vertical structure of the flow over Russia, and over the midlatitude eastern Pacific, is baroclinic. The final evolved 850 hPa pattern is dominated, as in the composite Day +5 circulation, by a sprawling anticyclone in the midlatitude central Pacific, located beneath the anticyclone at 200 hPa (Fig. 5.12b). The optimal evolution to maximize growth into a retracted state thus represents a transition from a tilted, baroclinic structure to one that is equivalent barotropic. The optimal initial structure of tropical OLR is characterized by enhanced OLR in a zonally expansive region in the central Pacific, which amplifies over the ten-day period as evidenced by the final evolved structure (Fig. 5.13). A region of reduced OLR that developed over the Indian Ocean is observed in the final, evolved tropical OLR pattern as well.

The growth of the optimal initial structures into the final evolved patterns just discussed depends on the lag chosen to define the optimal patterns. Figure 5.14 shows the growth as a function of lag for a range from 1-20 days, revealing that there is some growth into the final pattern at all lags shown. Growth is maximized when an optimization interval of nine days is

employed. Thus the optimal initial structures previously discussed coincide with the timing of greatest growth into the retraction norm.

It is necessary to determine whether the optimal initial structures indeed correspond to a retracted state ten days later. Figure 5.15 shows the projection of stream function optimal initial structures onto the stream function principle components, versus the projection of the retraction norm onto the state vector ten days later. A positive relationship between the two projections indicates that days when the optimal is positive (promoting retraction), ten days later the data project positively onto retraction norm (meaning when the optimal is observed, ten days later a retracted state is often observed). The correlation between the optimal projection and norm projection at ten-day lag is 0.67, providing confidence in the LIM's ability to identify structures related to retraction in reality.

5.4 Discussion and Conclusions

The LIM composed of midlatitude stream function and tropical OLR anomalies developed in this chapter exhibits linear, stable dynamics and can be used to identify meaningful structures in the low-frequency Northern Hemisphere circulation. Specifically, using a retraction-based norm reveals optimal initial features that were identified using unfiltered observations in the two retraction cases investigated previously. The optimal initial 200 hPa stream function pattern has many similarities with the tropopause-level circulation anomalies observed and described in the two case studies examined in the previous chapters. In particular, the anticyclonic anomaly located on the north side of the jet over Eurasia is in a similar location as the upstream anticyclones, B and 'B', that were emphasized in the two case studies. At 200 hPa the optimal includes an anticyclone in the east Pacific with a cyclonic feature directly to its south, which resembles the composite Day $-$ 5 stream function field (Fig. 5.8b). This preexisting

ridge/trough couplet are associated with anomalous stretching deformation in the environment, which was shown to exert a strong impact on the circulation in the two cases investigated in Chapters 2 and 4. Further support for the role of the preexisting deformation in the eastern Pacific, and the upstream anticyclonic anomaly poleward of the jet axis, is thus attained from complementing case study analysis and piecewise tendency diagnosis with the LIM perspective to diagnose jet retractions.

From a completely different analytical perspective, based on statistical relationships used to infer dynamic relationships in the LIM, features similar to those emphasized in the two case studies presented in Chapters 2-4 are identified as important to retractions. Ongoing work will attempt to use the LIM as a forecast tool to predict the onset of retractions at the 2-4 week forecast range, as well as investigate which aspects of the system (tropical heating, midlatitude dynamics) most heavily influence the growth and overall evolution of retractions.
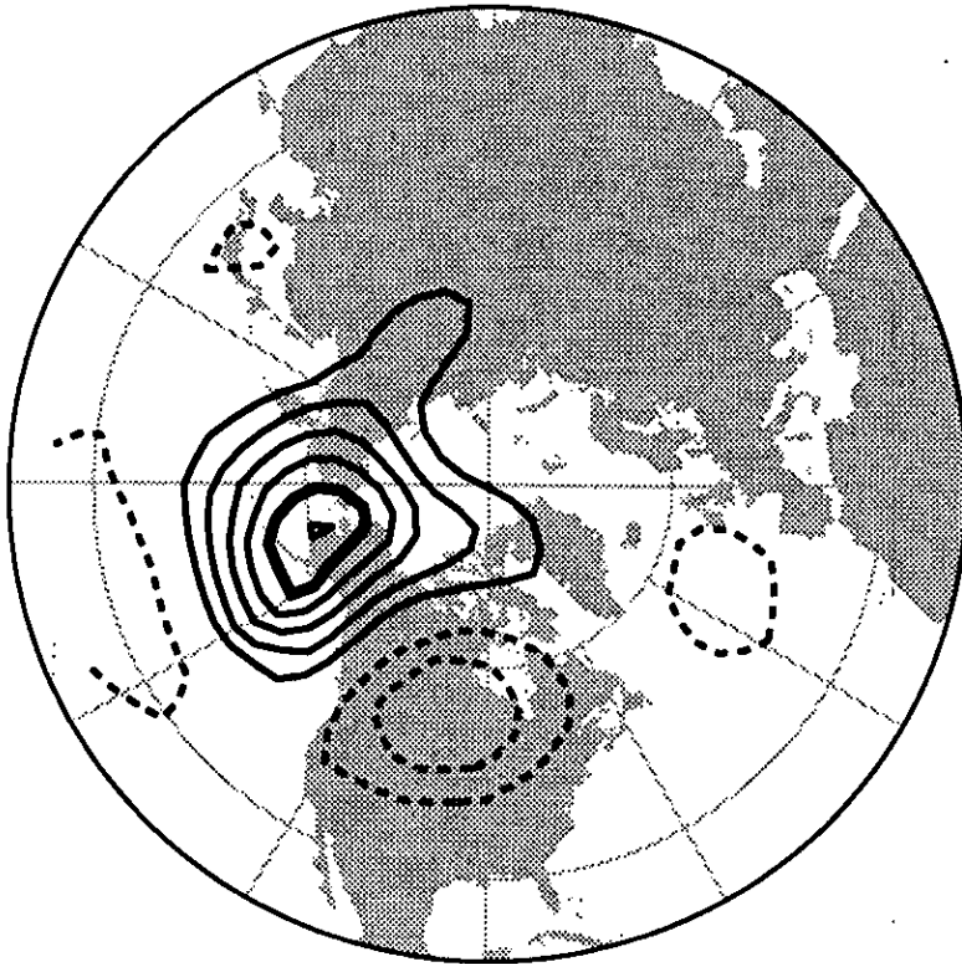
Fig. 5.1: Adopted from Renwick and Wallace 1996 (their Figure 1). Contours of the covariance between normalized ECMWF day-10 rms errors over the Pacific sector (90E – 90W) and verifying analysis height anomalies. Contours are in meters with a 10-m contour interval. Negative contours are dashed, the +50-m contour is thickened and the zero contour is suppressed.
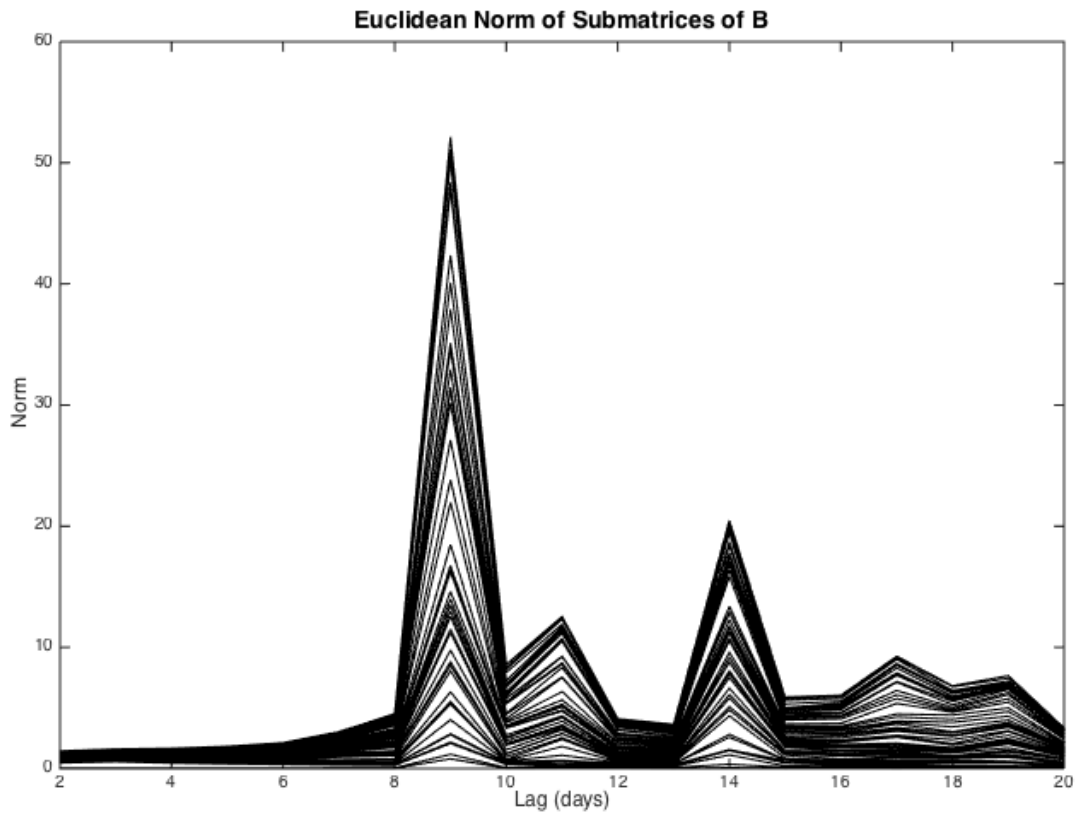
Figure 5.2: Tau-test for the linear inverse model as in Penland and Sardeshmukh (1995). Values of the norm of the submatrices of the dynamical operator L are plotted against the $l\tau_o$ used to compute the lagged covariance matrix.
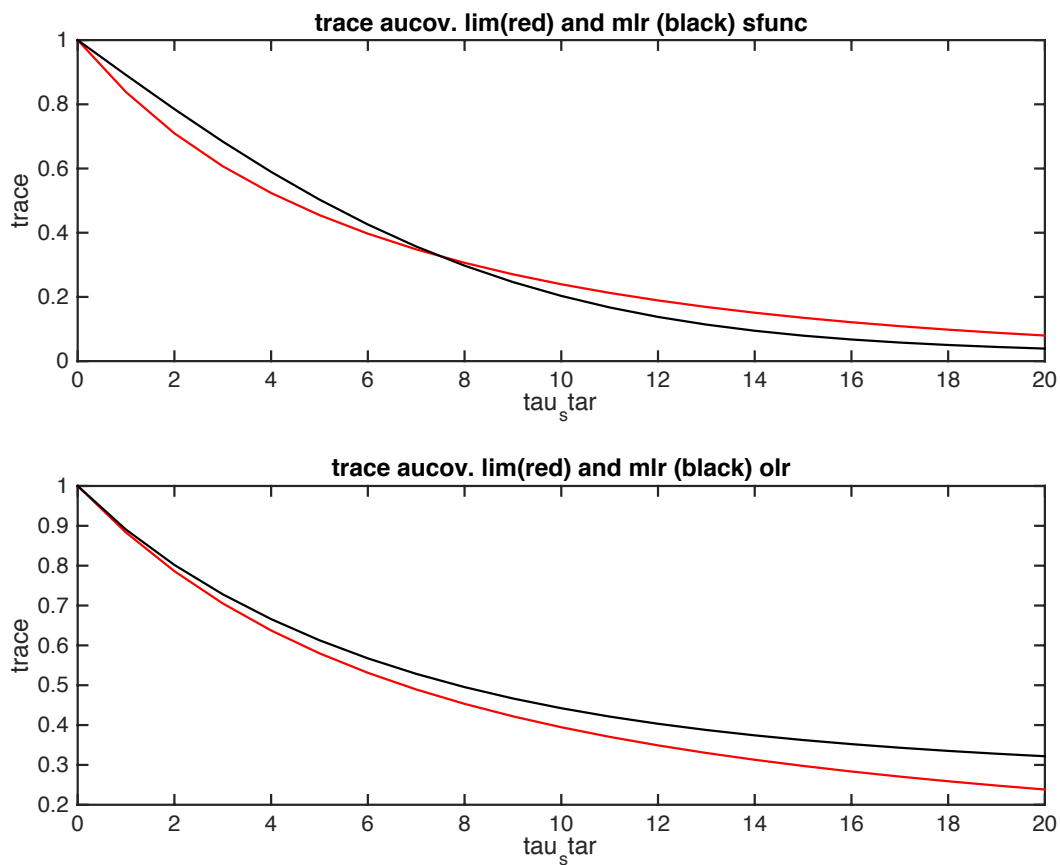
Figure 5.3: Trace of the autocovariance of the system as a function of lag, predicted by the LIM (red lines) and by multiple linear regression (black lines) for a) midlatitude stream function and b) tropical OLR.
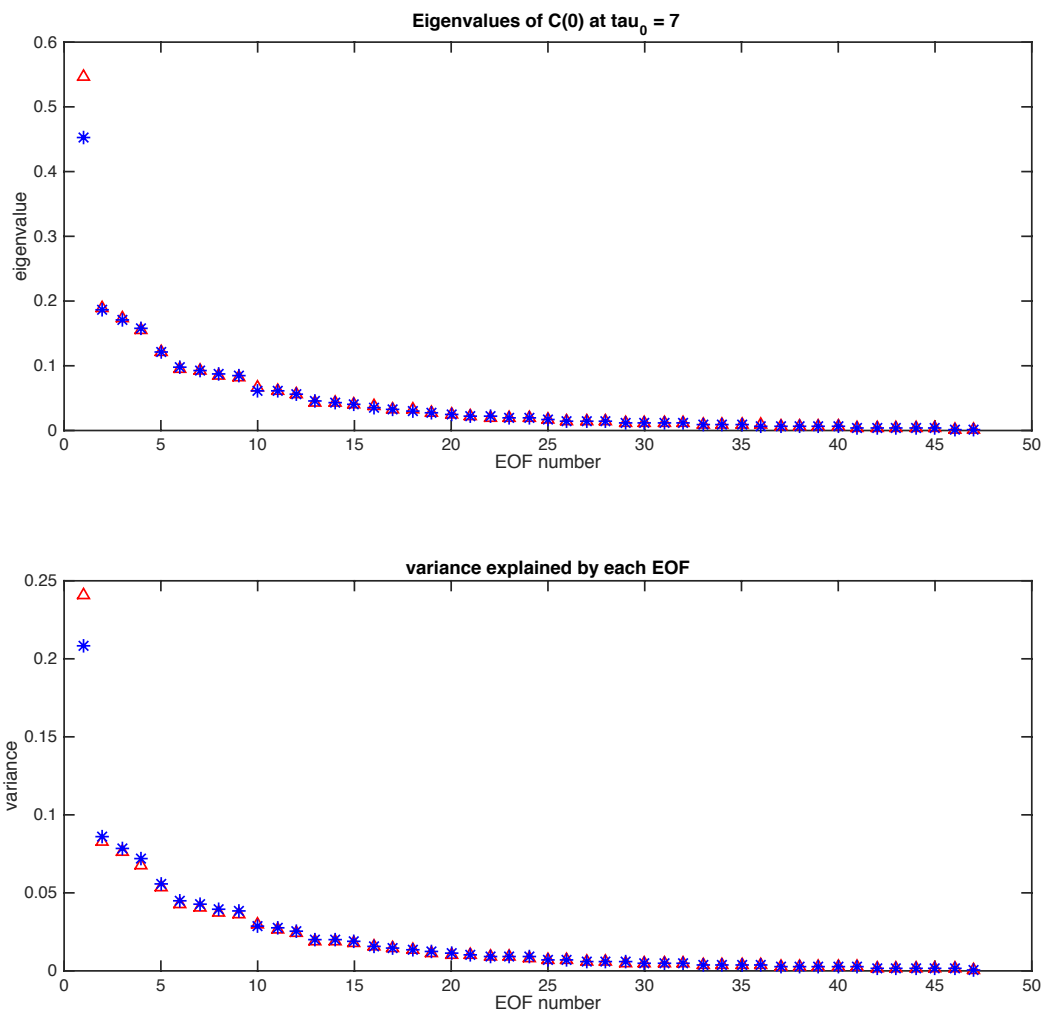
Figure 5.4: The top panel shows the eigenvalues of **C0** computed using the total noise covariance matrix, **Q**, (red triangles), and using a modified noise covariance matrix that has the two negative eigenvalues of **Q** removed (blue stars). The bottom panel shows the corresponding fraction of the variance explained by each EOF of **C0** using the total (red triangles) and modified (blue stars) **Q**.
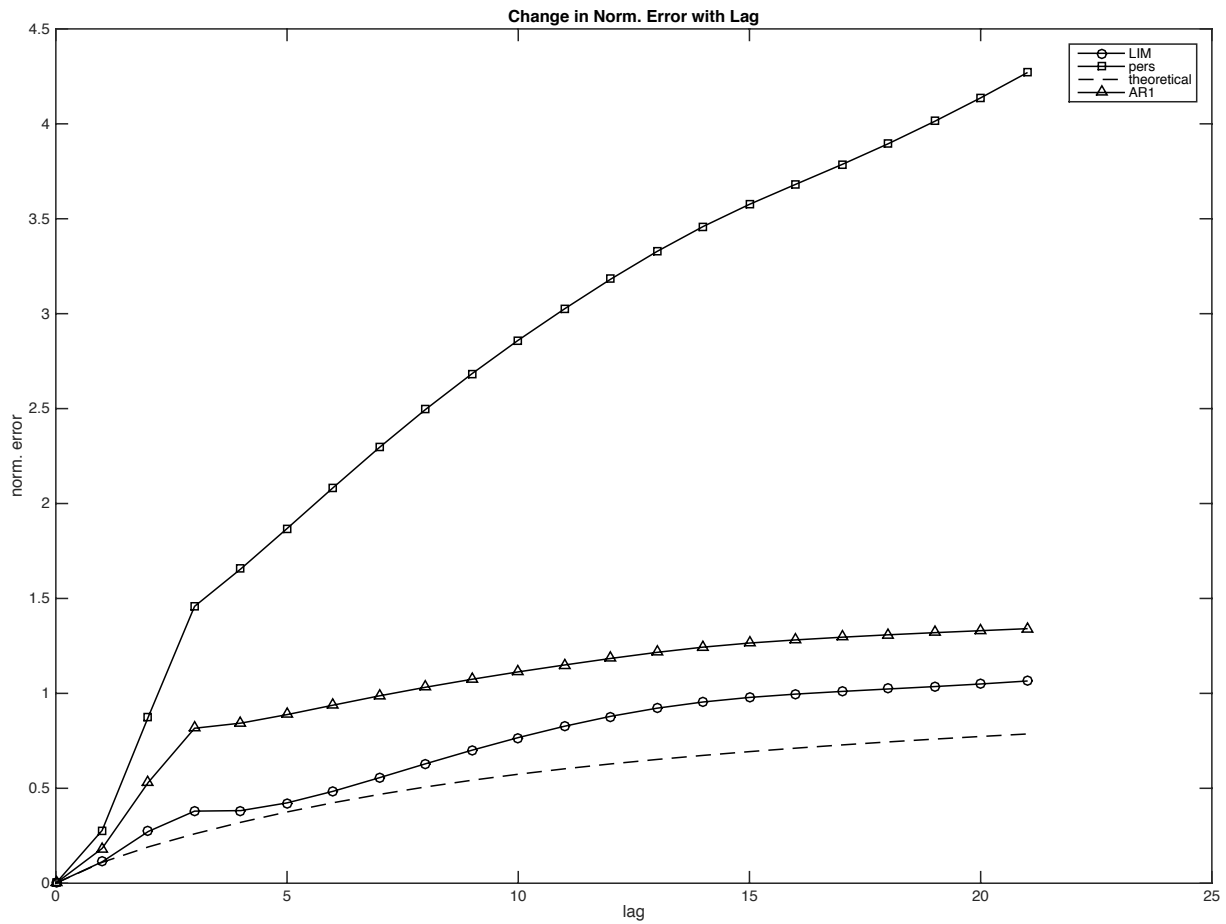
Figure 5.5: Change in error variance with changing forecast interval predicted by theory (black dash), produced by the LIM (open circles), an AR(1) process (open triangles) and persistent (open squares).
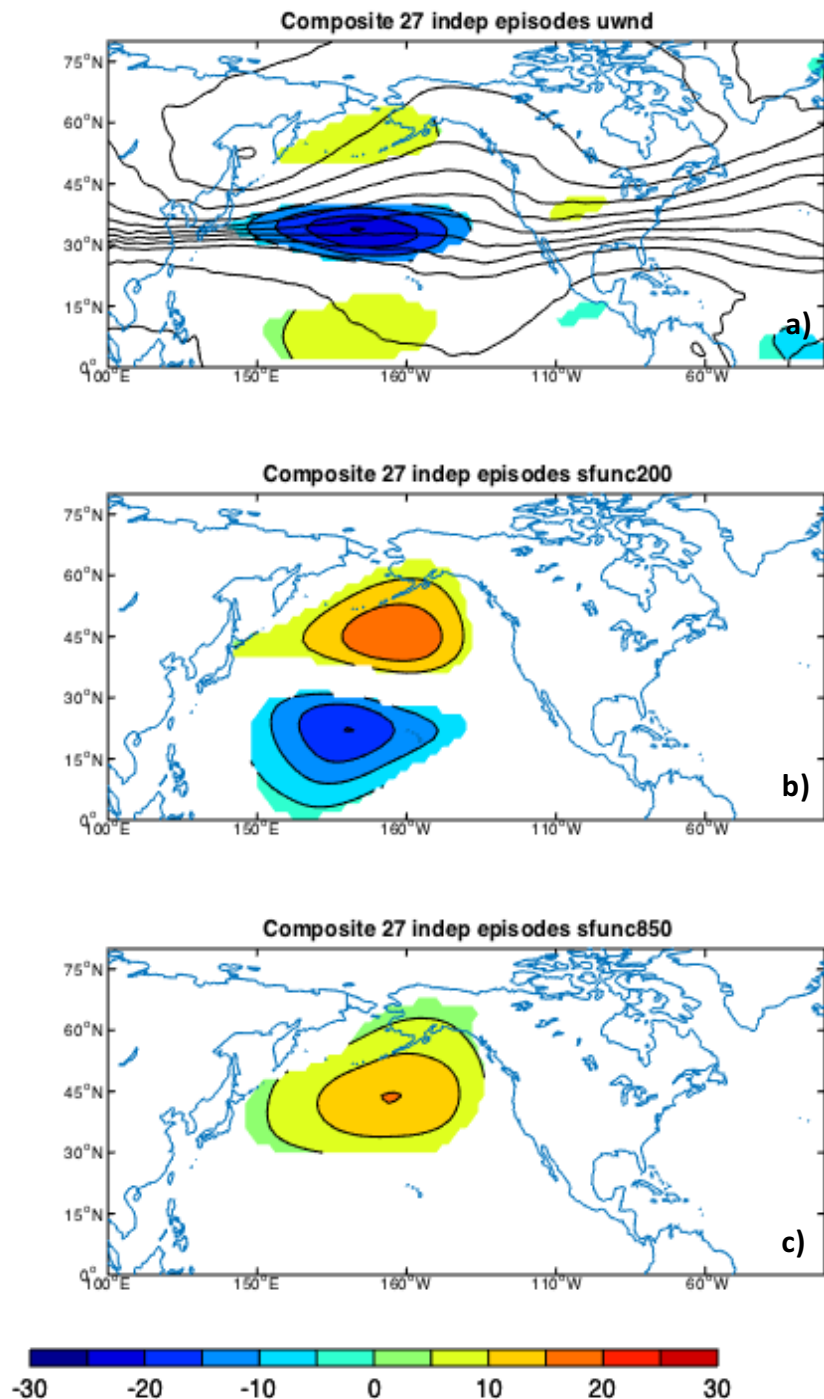
Figure 5.6: The color shading shows the composite unstandardized a) 200 hPa u'$_\psi$ b) 200 hPa ψ', and c) 850 hPa ψ', for the first day (Day 0) of 27 independent retractions identified for DJF, 1979-2014. The units of u'$_\psi$ are m s^{-1} and the units of stream function ψ' are 10^6 m^2 s^{-1}. Only values significant at the 99% confidence level are shown. The black contours show the composite tropopause pressure at Day 0 starting at 50hpa in 25hPa intervals to 350hPa.

DJF 1979-2014 Mean Tropopause Pressure

Composite Tropopause Pressure at Retraction Onset
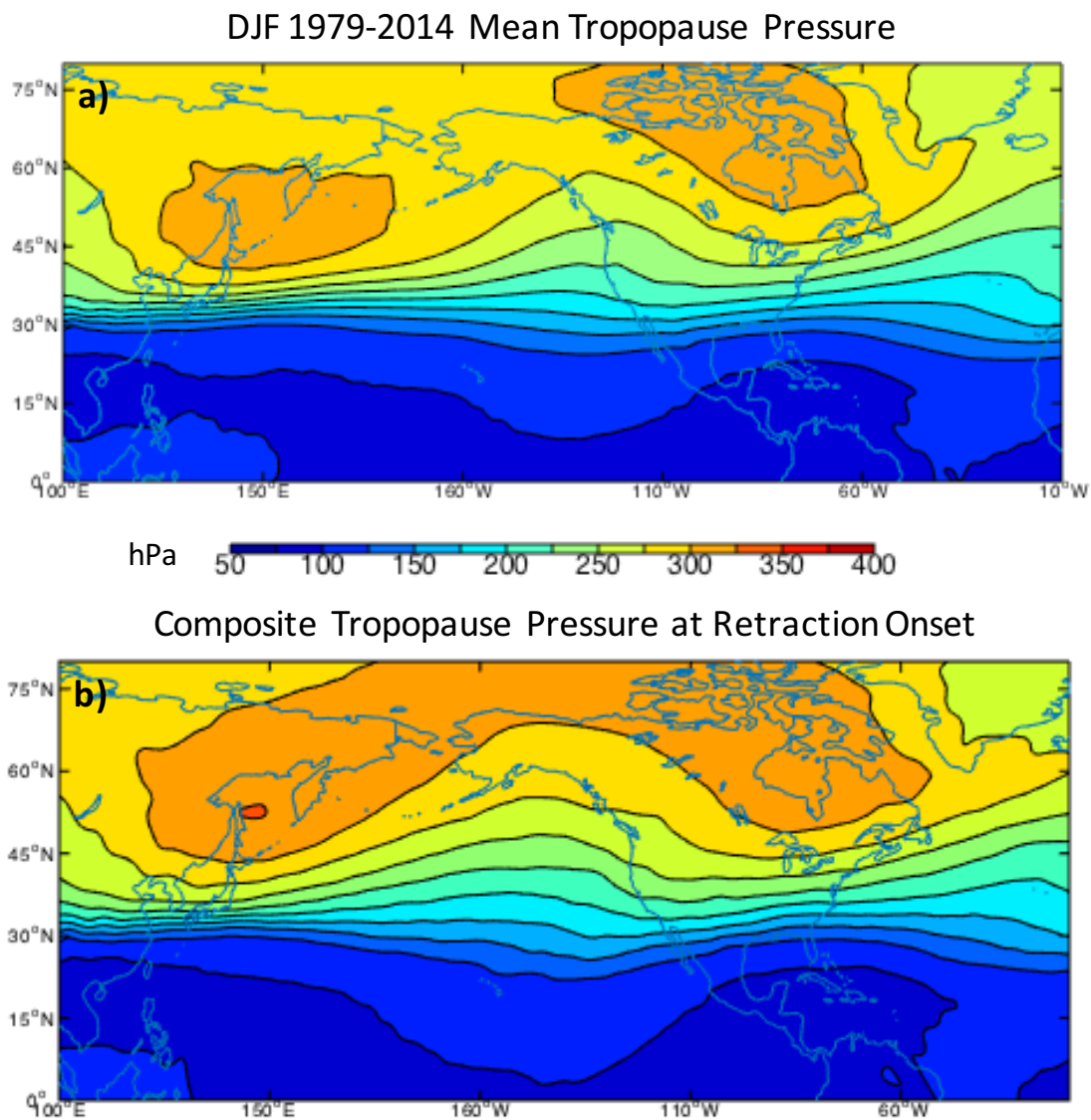
Figure 5.7: a) the color shading indicates the DJF 1979-2014 average tropopause pressure for all days in the time series, and b) shows the composite tropopause pressure averaged for the first day of each retraction event, in units of hPa.
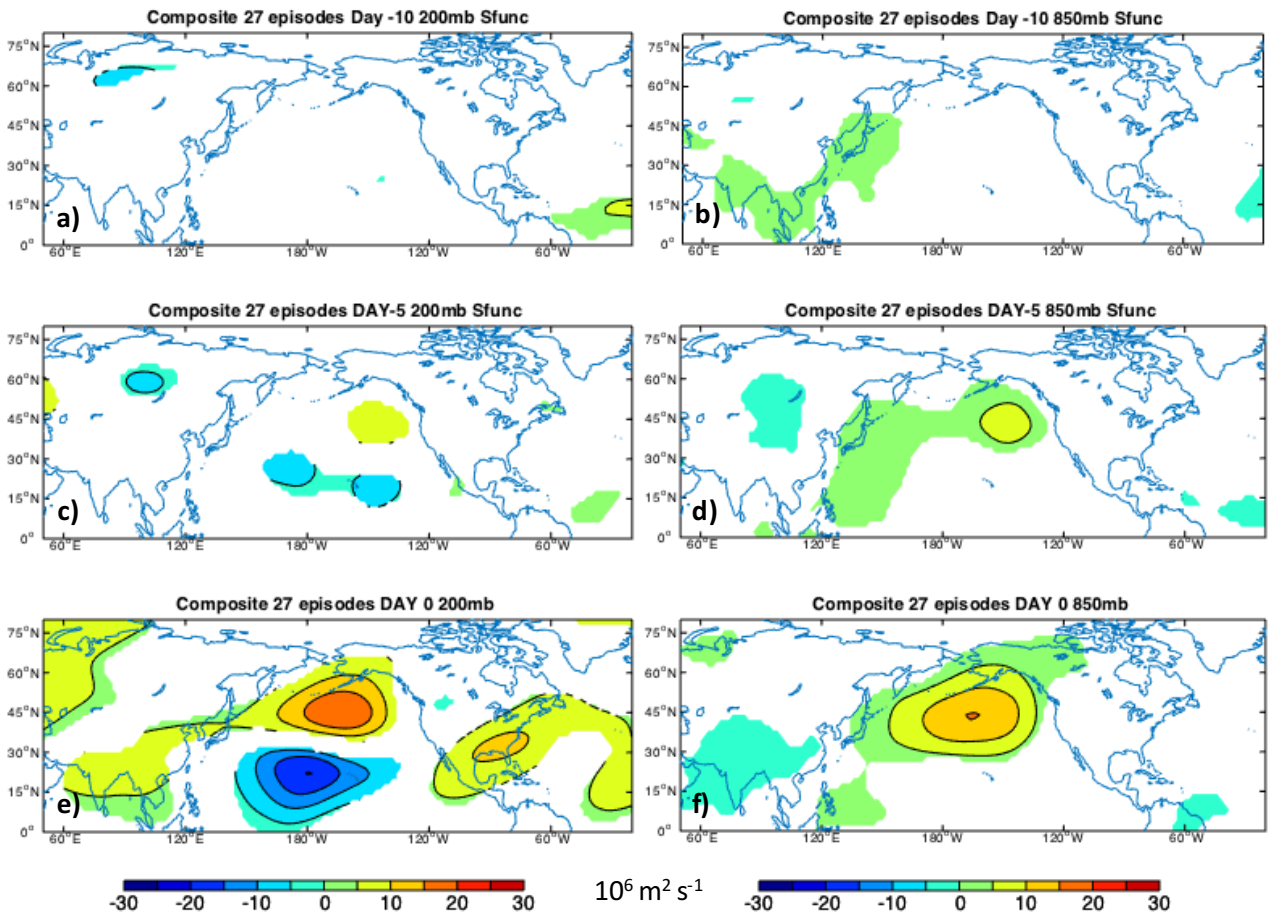
Figure 5.8: Composite evolution of 200 and 850 stream function anomalies at Day – 10, Day – 5 and Day 0 for 27 retraction cases identified. 200 hPa stream function evolution is shown in a), c) and e), and 850 hPa stream function evolution is shown in b), d) and f). The patterns shown are all significant at the 95% confidence level.
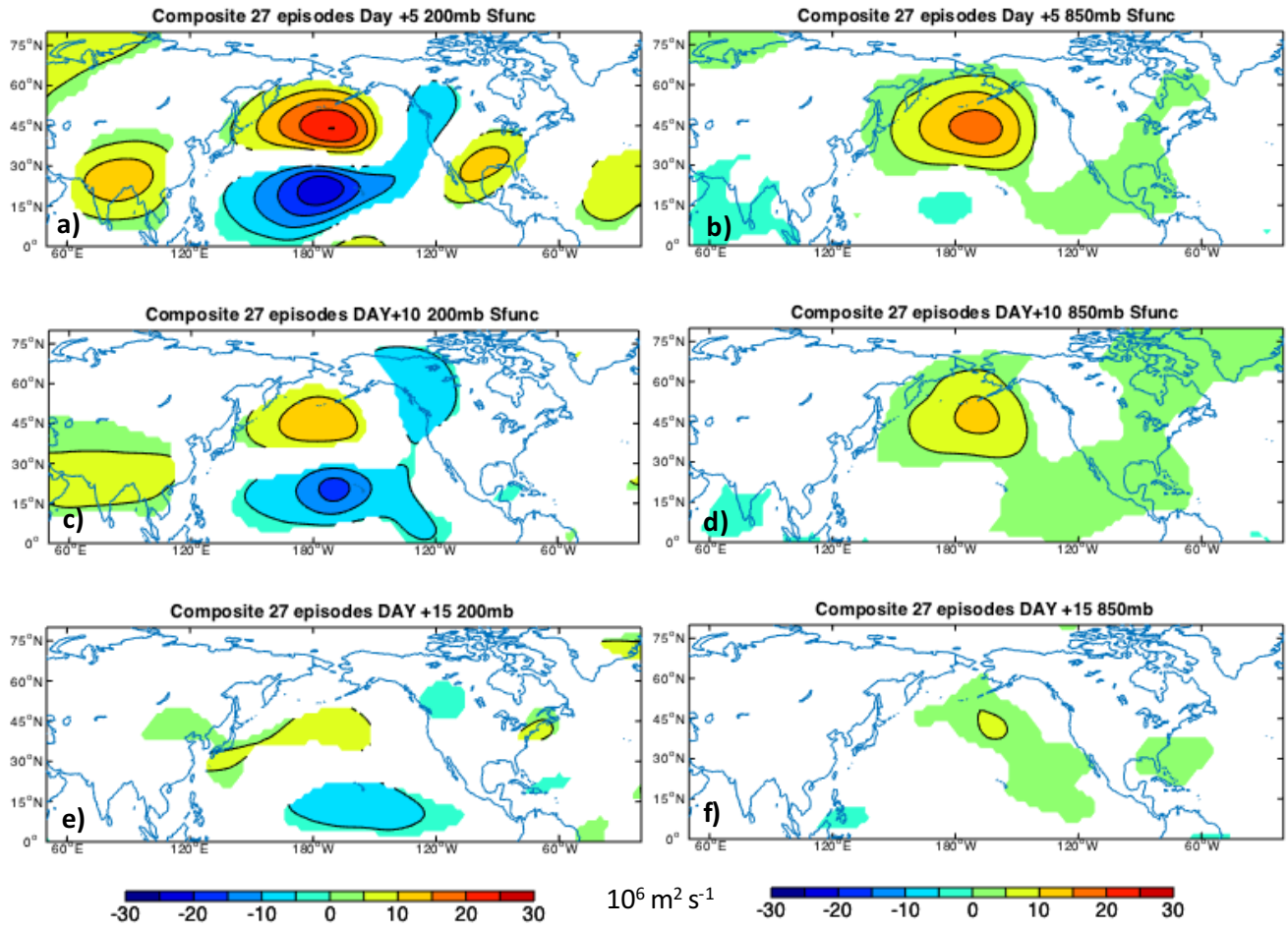
Figure 5.9: As in Fig. 5.8 except for Day +5, Day +10, Day + 15.
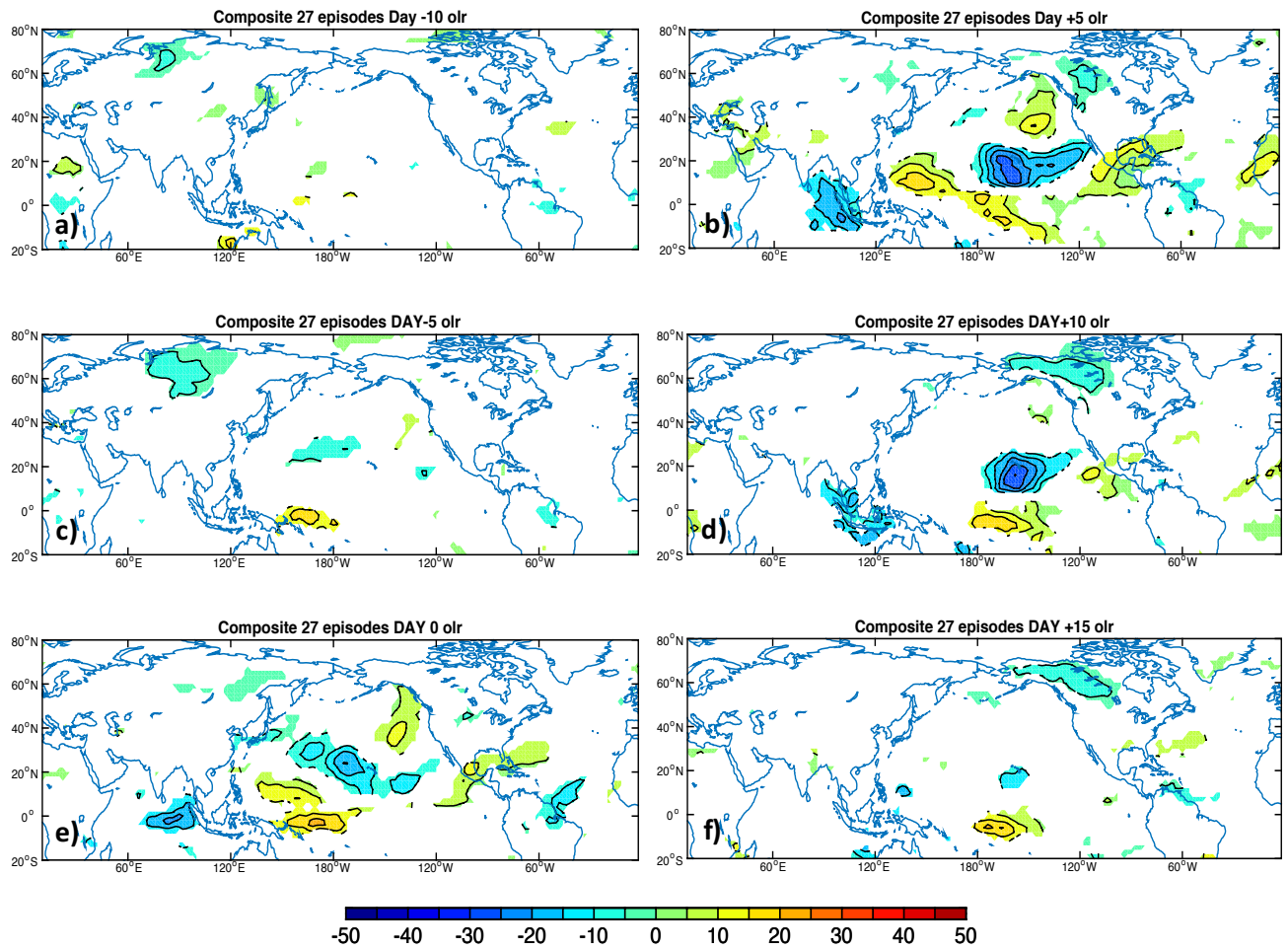
Figure 5.10: OLR anomalies associated with a) Day -10, b) Day -5, c) Day 0, d) Day +5, e) Day +10, and f) Day +15.

sfunc$_m$id$_2$00--L-matrix--initial

$\times 10^7$

sfunc$_m$id$_2$00--L-matrix--final

$\times 10^7$
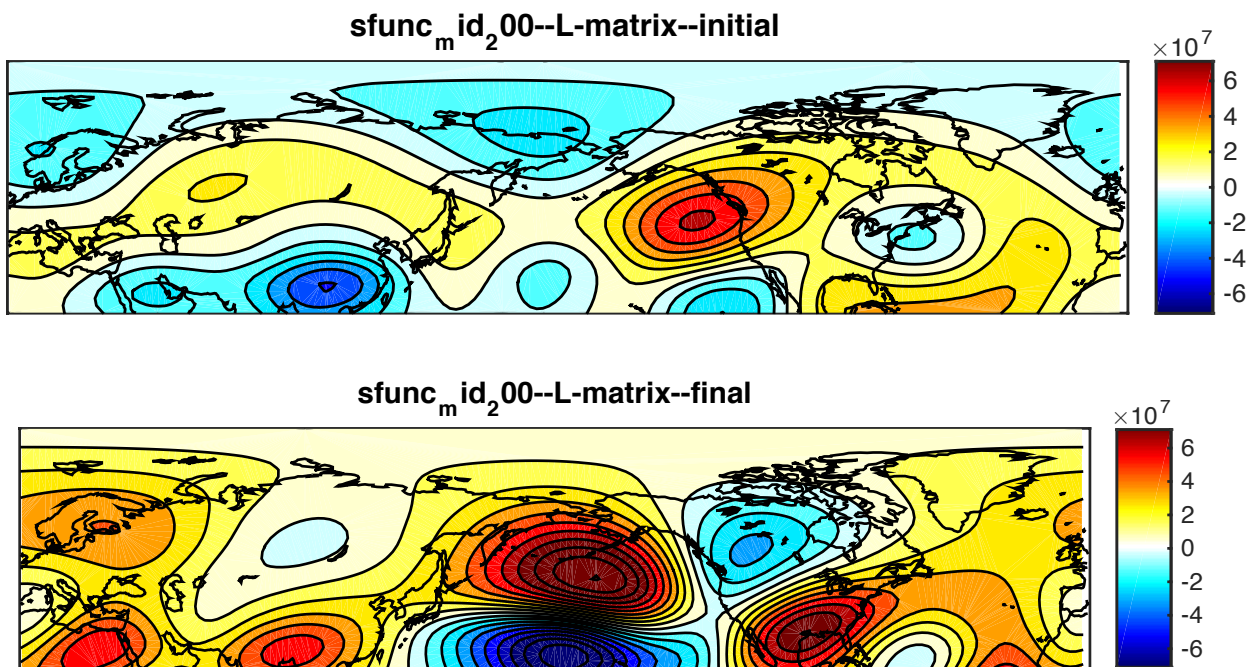
Figure 5.11: The top panel shows the initial optimal 200 hPa stream function pattern produced by the LIM for a 10-day optimization interval, and the bottom panel shows the final evolved 200 hPa stream function pattern. Units are m^2 s^{-1}.

sfunc$_m$id$_8$50--L-matrix--initial

sfunc$_m$id$_8$50--L-matrix--final
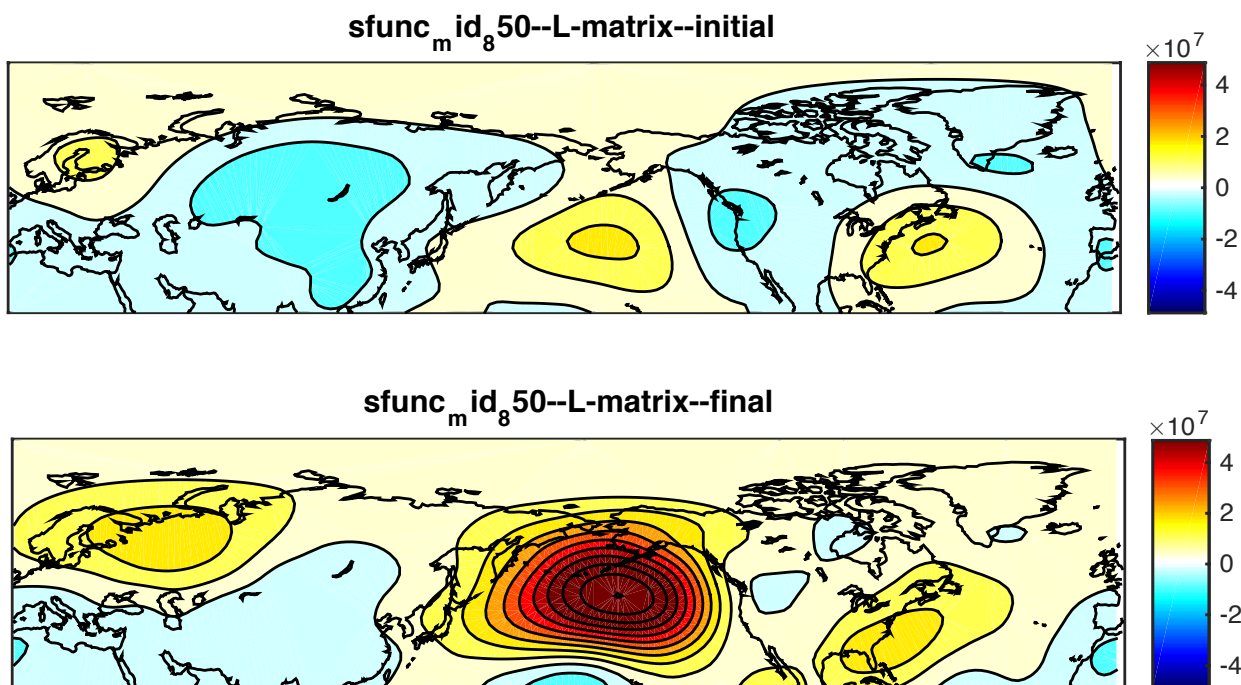
Figure 5.12: The top panel shows the initial optimal 850 hPa stream function pattern produced by the LIM for a 10-day optimization interval, and the bottom panel shows the final evolved 850 hPa stream function pattern. Units are m^2 s^{-1}.

olr$_t$rop$_1$--L-matrix--initial

olr$_t$rop$_1$--L-matrix--final
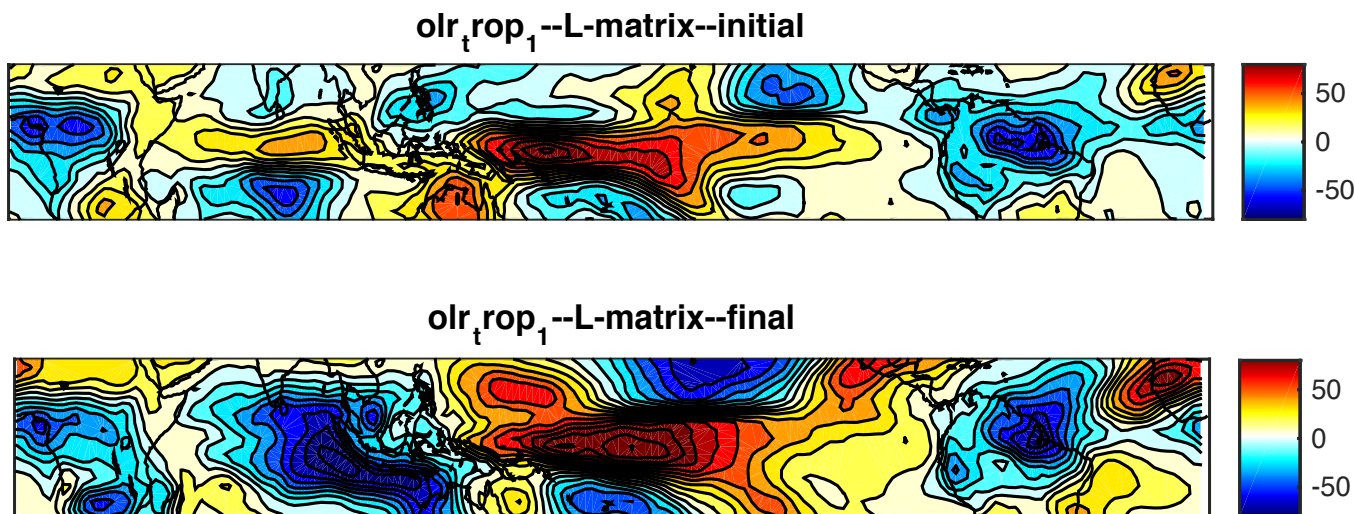
Figure 5.13: The top panel shows the initial optimal tropical OLR anomaly pattern produced by the LIM for a 10-day optimization interval, and the bottom panel shows the final evolved OLR anomaly pattern. Units W m^{-2}.
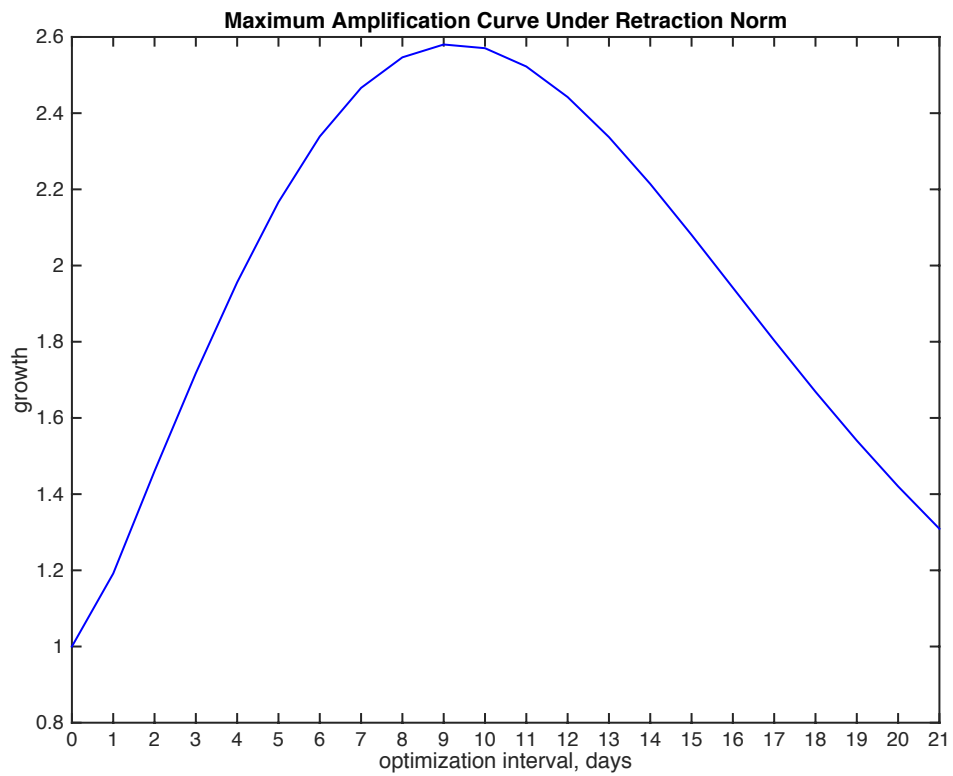
Figure 5.14: Maximum amplification curve of the initial optimal structures under the retraction norm. The period over which the optimals are computed is shown on the x-axis, with the corresponding amount growth at each lag plotted on the y-axis.
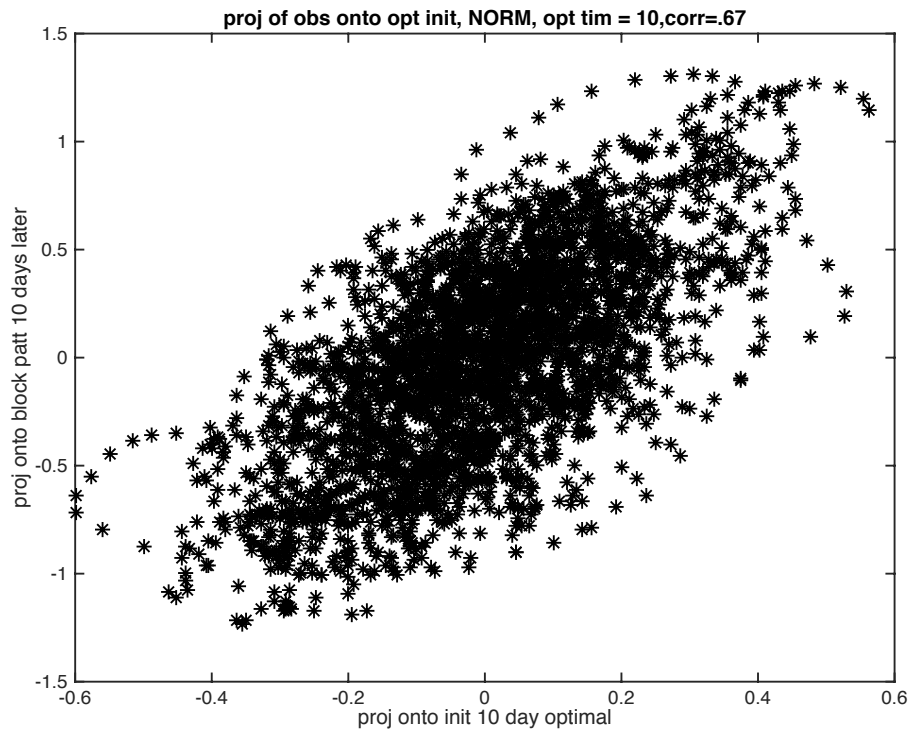
Figure 5.15: Projection of optimal initial pattern onto the standardized principle components of the 850 and 200-hPa streamfunction (x-axis) versus projection of retraction norm onto the principle components ten days later (y-axis).

CHAPTER 6: CONCLUSIONS

In this dissertation, the initiation of boreal winter north Pacific jet retractions was investigated through two independent but complementary techniques: quasi-geostrophic piecewise tendency diagnosis and linear inverse modeling. Two case studies of retractions in February 2006 and 2017 were undertaken, and through synoptic analysis and QGPV inversion, the processes facilitating retraction were identified. Additionally, the processes governing the evolution of eddies involved in retraction were examined. Both of the retractions investigated here occurred in February and were associated with substantial Hawaiian precipitation, often leading to flooding and mudslides during the retracted period. It was found that anticyclonic wave breaking at high latitude and on lower-than-average isentropic surfaces frequently occurred during retraction, while to the south stationary, smaller-scale troughs were observed. Another commonality between the cases, and other retractions cursively examined, is the emergence of anticyclonic anomaly that reaches the jet entrance region on the cyclonic shear side of the jet, inducing a wave train and the development of the LC1 breaking waves.

Deemed important features that commonly facilitate retraction, the lifecycle of the first anticyclonically- breaking wave was analyzed using piecewise tendency diagnosis in each case. Both lifecycles were heavily governed by preexisting deformation, particularly in the jet exit region. The exit region was characterized by a northward (southward) diverted QGPV gradient on its northern (southern) side, which led the waves to cease propagating eastward, become stationary and overturn. In particular, the meridional straining of ridges by deformation in the environment initially aids in the development of the ridges, increasing their amplitude overall. However, at a certain point the anomalies become deformed in a way that their circulation is attenuated, not consolidated, and the height anomaly ceases to amplify via deformation. The

'straining' of the positive height anomalies by the mean state deformation is similar to the eddy straining mechanism proposed by Shutts (1983) as a blocking maintenance mechanism. In the 2006 case the straining of Feature A coincided with the upstream movement of a high-amplitude block in the flow, at the same moment that the deformation term weakened A by attenuating its shape, not consolidating it. Therefore, at the point when deformation weakens a transient disturbance such as A, it is possible the background, low-frequency flow is strengthened. The effect of the subsequent anticyclonic wave breaking north of the climatological jet axis and within the 315-330K isentropic layers reinforced the preexisting block and associated weak westerly winds, maintaining the retraction.

Deformation thus had two roles in retraction: governing the shape and development of eddies, while simultaneously altering their propagation characteristics. In some cases, this sequence of events repeated due to a second positive height anomaly reaching the entrance region, and the resultant serial anticyclonic wave breaking events reinforced the retracted state, and helped maintain a persistent Rex block.

A novel expansion of piecewise tendency diagnosis to quantify the QG, piecewise contributions to geostrophic wind tendencies has been introduced. The meridional gradient of height tendencies was found to be proportional to the tendency of the zonal geostrophic wind, and similarly, the zonal gradient of height tendencies is proportional to the change in meridional geostrophic wind. By assuming QGPV conservation following the geostrophic flow, geostrophic wind tendencies can be diagnosed in a piecewise manner just as height tendencies are in traditional PTD. The assumption of QGPV conservation is valid for large-scale (Rossby number <1) adiabatic, frictionless flow (Holton 1996).

The quasi-geostrophic zonal wind tendencies attained from the expanded piecewise tendency diagnosis matched the observed change in zonal wind quite well. It was found that the instantaneous acceleration was dominated by the movement of height anomalies, which reflects the opposing effects of the upstream propagation of the wave along the PV gradient, and the rate at which the mean flow advects features downstream. The instantaneous deceleration at a particular location is linked to the periodic movement of waves and their height tendencies, which fluctuate with time. However, jet retractions are defined as periods when the zonal wind weakens for a prolonged period of time, so despite the short-term undulations in the acceleration, for the cases examined here a net weakening of the zonal wind occurred. To quantify the net deceleration experienced during retraction, deceleration was averaged over a horizontal box that encompassed the jet exit region in two cases. The five-day cumulative deceleration was then computed using observations, which was then compared to the deceleration explained by the sum of the piecewise zonal wind tendency terms. In both cases the non-linear vortex-vortex interactions associated with 50-500hPa QGPV accounted for the majority of the net, five-day retraction. The non-linear terms are, by definition of the time- averaged mean state used here, the only terms that *could* account for the 5-day mean deceleration, but there was no guarantee that any of the observed retraction *would* be accounted for by QG processes.

The synoptic context in which the nonlinear terms produced a forcing for retraction was investigated. A wave train induced by the upstream anticyclone on the poleward side of jet is arranged in a way that leads to a contiguous band of negative PV advection, height rises, and a concomitant forcing to weaken the zonal wind. Two negative PV anomalies were situated farther northward than the trough in between them, leading to the *southward* advection of anomalous, negative PV in both cases. Of note is that the wave train was characterized by

positively-tilted anomalies on the cyclonic shear side of the jet axis in both cases, a configuration conducive to barotropic energy extraction by the eddies from the environment, consistent with a weakening of the low-frequency zonal wind and amplification of height anomalies.

The two ways in which PTD was applied to diagnose the onset of retractions, through investigation of the ways eddies force the zonal wind to weaken, and the ways eddies themselves develop during retraction, offers a new perspective on old ideas regarding the impact of deformation in the flow. Two important types of deformation are at play in retraction: shearing deformation associated with the jet entrance region and jet core, and stretching deformation associated with the jet exit region. Mak and Cai (1989) showed that a positively-tilted anomaly located in a region of cyclonic shear is conducive to barotropic growth of the anomaly at the expense of the mean state kinetic energy. In both cases this condition for barotropic growth was met, and accordingly the jet was observed to weaken. The synoptic situation observed at retraction onset appears to be conducive to both barotropic energy exchange and to strong vortex-vortex interactions, and both processes act to weaken the zonal wind in the cases shown here.

Vortex-vortex interactions represent an eddy forcing to the low-frequency QGPV gradient, which have been considered important for blocking maintenance (Hoskins et al 1983; Postel and Hitchman 2001; Athanasiadis et al 2007; Yamazaki and Itoh 2013). Hoskins et al. (1983) demonstrated the relationship between eddy vorticity flux convergence and the low-frequency QGPV gradient, and that convergence of the eddy vorticity flux will weaken the QGPV gradient and is important for understanding blocking onset and maintenance. Yamazaki and Itoh (2013) suggested that blocking anticyclones preferentially absorb small-scale anticyclones and repel cyclones, outlining a novel species of vortex-vortex interaction called the

'selective absorption mechanism'. The vortex-vortex interactions that facilitate retraction seem rather distinct from these two perspectives. In the two cases analyzed thus far, a zonally-elongated region of nonlinear QGPV advection along the jet axis weakened the zonal wind. A positively-tilted wave train, and the nonlinear advection of negative QGPV achieved by the waves, was conducive to this pattern of eddy forcing. This specific and novel eddy-mean interaction is contemporaneous with an environment conducive to barotropic energy extraction, a dynamical link that will be investigated in future research.

The entire transition to a retracted jet seems linked to the emergence of an external, anticyclonic anomaly that propagates across Eurasia and encounters the cyclonic shear side of the jet entrance region. This anomaly, referred to as Feature B in both cases, induced a positively-tilted wave train along the jet, and also weakened the zonal wind locally due to effects from its own height tendencies. Consistent with the emphasis on this upstream anticyclonic anomaly, Jaffe et al. (2011) identified a significant, negative PV anomaly situated north of the jet entrance region five days prior to retraction (Fig 1.8b). An anticyclonic impulse on the cyclonic shear side of the jet is somewhat analogous to a cyclonic impulse on the anticyclonic shear side, provided the combination of eddy tilt and environmental deformation are favorable. The latter configuration is observed when recurving tropical cyclones in the west Pacific approach the jet, and, similar to the retraction cases studied here, is related to an increase in wave amplitude (Archambault et al., 2013). Rothlisberger et al. (2016) developed a way to track regions where Rossby waves are initiated, and showed that initiation can occur when an arctic disturbance, in their case a tropopause polar vortex, moved southward over Siberia and then perturbed the midlatitude jet. Similarly, in the 2017 retraction case a wave train emanating from Siberia was observed, also leading to a perturbation of the jet which led to its retraction over the following

week. Once a wave train was induced, the waves propagated eastward, amplified, and then approached a region of stretching deformation that deformed the anomalies *and* halted their eastward movement.

The following overview offers a way retractions may generally evolve (Figure 6.1):

Given a zonal jet accompanied by deformation in the exit region, an external anticyclonic anomaly that approaches the cyclonic shear side of the jet entrance region will locally weaken the zonal wind, as well as induce the development of additional waves downstream (Figure 6.1a; a trough on the anticyclonic shear side of the jet, noted in gray, could produce the same response). The resultant wave train produces a pattern of negative PV advection via nonlinear, vortex-vortex interactions, wherein the circulation associated with QGPV anomalies rearranges the anomalous QGPV field. The resultant negative PV advection occurs along the jet, forcing a weakening of the zonal wind and leading to retraction (Figure 6.1b). Subsequently, anomalies within the wave train propagate eastward and enounter the deformation region, which can change the shape of eddies approaching it. Deformation also represents a distorted QGPV gradient that is oriented largely east-west, in contrast to the typical meridional orientation. There is first a period when the anomaly, particularly anticyclones, will amplify due to deformation as its circulation is consolidated. Amplification through this process eventually ceases, as the deformation region renders the ridge more diffuse and meridionally elongated (Figure 6.1c). Subsequently, the ridge ceases to propagate, and overturns. The overturning produces a blocking-type pattern within the flow, and the easterly flow on the southern edge of the overturning anticyclone weakens the westerlies. The upstream movement of the mean state deformation region is thus maintained and often shifted upstream during the wave breaking event (gray lines Fig 6.1c).

The maintenance of the retraction depends upon additional external anomalies (Feature 'C' observed in the 2006 case) or in-situ processes like diabatic heating, which erodes PV at high levels has been shown to affect the persistence of blocking anticyclones (Pfahl et al., 2015). The selective absorption mechanism proposed by Yamazaki and Itoh (2011) is another way a block, which in the right location maintains retraction, could persist. Future research will apply the diagnostics used in this thesis to examine retraction *initiation* to diagnose the processes governing retraction *maintenance*.

To evaluate the robustness of the features emphasized in the cases studies, a linear inverse model was used to identify the atmospheric structure that optimally grows into a retracted pattern. The LIM used here was composed of tropical OLR, a proxy for convective activity, and midlatitude stream function at 200 and 850 hPa. Within the LIM framework one assumes the system of interest can be approximated by linear dynamics and stochastic white noise forcing. Penland and Sardeshmukh (1995) outlined ways to confirm these assumptions are accurate, and application of these tests show that assumption of linearity in the model holds up well. LIM can objectively identify optimal, initial structures in the atmosphere that most rapidly amplify over a specified time interval, here an interval of ten days. A strong advantage of LIM is that growth can be optimized towards a particular prescribed pattern, such as the circulation associated with a jet retraction. The tropopause-level structure identified by the model that grows most rapidly into a retraction, at a lag of 10-20 days, resembles the patterns observed as precursors to retraction observed in the two cases. Most notably the presence of an anticyclonic anomaly located over Eurasia in the midlatitudes, poleward of the jet axis, is similar to Feature B which was shown to be a key dynamic actor in facilitating retraction. Additionally, the optimal initial structure included a preexisting ridge in the far eastern midlatitude Pacific, and a trough to

its south. Together these anomalies produce deformation in the environment in the days just before retraction. Preexisting deformation was also observed and considered a crucial feature in the transition to a retracted jet in the case studies.

In this thesis the relationship between the shape, propagation, and influence of transient disturbances on the zonal wind was rigorously investigated. Particular combinations of the wave orientation with the background shearing deformation within the jet, and with stretching deformation in the jet exit region, appear to be conducive to the retraction of the north Pacific jet in boreal winter. Through a novel expansion of piecewise tendency diagnosis, it was found that nonlinear, vortex-vortex interactions created a net eddy forcing to weaken the zonal wind, consistent with previous studies that emphasized the role of nonlinear processes in weakening the mean QGPV gradient.   Case study analysis based on observations and QG diagnostics was complemented with the use of a statistically-based linear inverse model. The LIM used the statistics of a simple system to identify optimal initial circulation patterns that most rapidly grow into a retracted state over a ten-day period. The initial patterns identified objectively reveals features that were observed in the case studies and were shown to exert a powerful influence on the zonal wind. Thus, via two independent techniques, similar precursors to retraction were identified. The dynamic impacts of those precursors on the zonal wind, and their subsequent evolution during retraction, were contextualized and quantified via QG piecewise tendency analysis. The combination of detailed, theory-rooted case studies, along with the use of an empirical statistical model, and the complementary, consistent information regarding retraction each tool provided, suggests the results presented in this thesis are somewhat robust. In the future these two tools – QGPV inversion and the LIM – will be applied to further untangle and
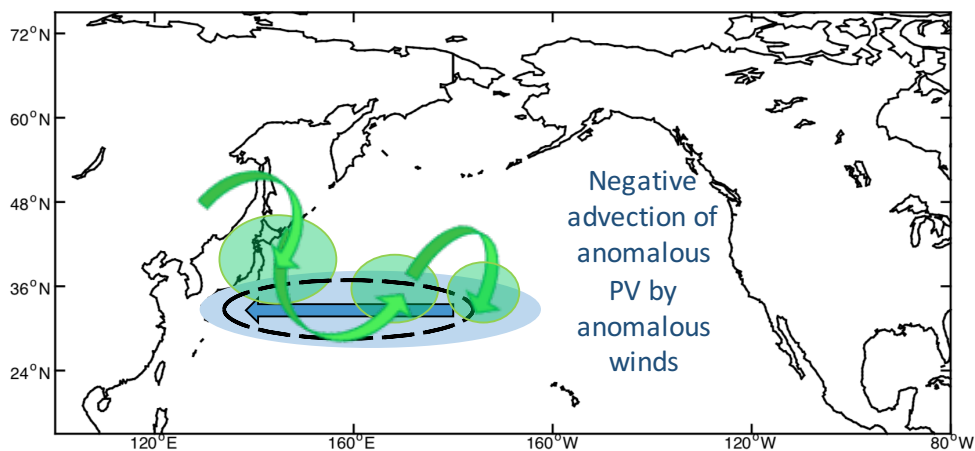
generalize the processes routinely governing retraction and to interrogate other important

synoptic transitions in the large-scale circulation.

Environment Conducive to Retraction: Barotropic Growth
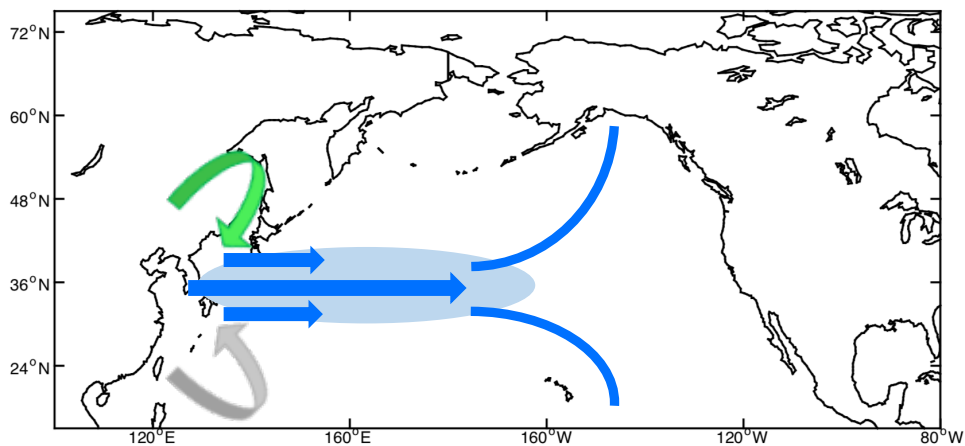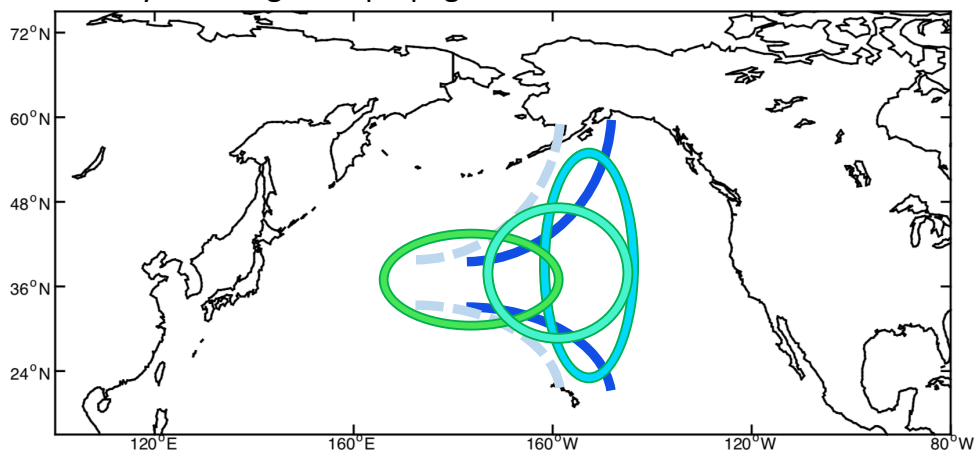

a)

Retraction via nonlinear vortex-vortex interactions

b)

Eddy straining halts propagation and maintains deformation

c)

Figure 6.1: Schematic evolution that produces retraction. a) shows a positively-tilted anticyclonic anomaly in green reaching the cyclonic shear side of the jet, conducive to generating waves and barotropic energy extraction. The shear of the jet is represented by the blue arrows, and the jet core by the light blue oval. The gray negative height anomaly represents another combination of tilt and shear that could produce the same influence on the jet, but was not the focus in the case studies analyzed in this thesis. b) illustrates the subsequent evolution of the waves and the position of the zonal wind tendency associated with nonlinear QGPV advection (area encompassed by black dashed oval), a forcing for the zonal wind to weaken (blue/black arrow). The blue shaded area marks the mean jet core, and the two green shade areas show the location of two negative QGPV anomalies, which are advected by the anomalous winds in green, to weaken the jet. c) illustrates the effect of stretching deformation in the environment (dark blue lines) on a positive height anomaly by changing the anomaly's shape (eddy straining), and by halting its eastward movement. Anticyclonic wave breaking frequently follows eddy straining, helping to maintain retraction. The light blue dashed lines indicate the upstream movement of the deformation region due to the evolution of the height anomaly in green.

REFERENCES

1. Athanasiadis P. J., J. M. Wallace, and J. J. Wettstein, 2010: Patterns of wintertime jet stream variability and their relation to the storm tracks. *J. Atmos. Sci.,* **67,** 1361-1381, doi:10.1175/2009JAS3270.1.

2. R. Berggren, B. Bolin & C.-G. Rossby (1949) An Aerological Study of Zonal Motion, its Perturbations and Break-down, Tellus, 1:2, 14-37

3. Blackmon, M.L., J.M. Wallace, N. Lau, and S.L. Mullen, 1977: An Observational Study of the Northern Hemisphere Wintertime Circulation. *J. Atmos. Sci.,* **34**, 1040–1053.

4. Blackmon, M. L., Lee, Y.-H., J. M. Wallace, H.-H. Hsu 1984: Horizontal structure of 500 mb height anomaly fluctuations with long, intermediate and short time scales as deduced from lag-correlation statistics. *J. Atmos. Sci.*, **41,** 981-991.

5. Charney, J. G. and M. E. Stern, 1962: On the stability of internal baroclinic jets in a rotating atmosphere. *J. Atmos. Sci.,* **19**, 159-172.

6. Colucci, S. J., and D. P. Baumhefner, 1998: Numerical Prediction of the Onset of Blocking: A Case Study with Forecast Ensembles. *Mon. Wea. Rev.*, **126**, 773-784.

7. Davis, C., and K. A. Emanuel, 1991: Potential vorticity diagnostics of cyclogenesis. *Mon. Wea. Rev.,* **119,** 1929-1953.

8. Dee, D. P., S. M. Uppala, A. J. Simmons, P. Berrisford, P. Poli, S. Kobayashi, U. Andrae, M. A. Balmaseda, G. Balsamo, P. Bauer, P. Bechtold, A. C. M. Beljaars, L. van de Berg, J. Bidlot, 5. N. Bormann, C. Delsol, R. Dragani, M. Fuentes, A. J. Geer, L. Haimberger, S. B. Healy, H. Hersbach, E. V. Hólm, L. Isaksen, P. Kållberg, M. Köhler, M. Matricardi, A. P. McNally, B. M. Monge-Sanz, J.-J. Morcrette, B.-K. Park, C. Peubey, P. de Rosnay, C. Tavolato, J.-N. Thépaut and F. Vitart, 2011: The ERA-Interim reanalysis: configuration and performace of the data assimilation system. *Quart. J. Roy. Meteor. Soc.*, **137-656**, Part A, 553–597. DOI: 10.1002/qj.828.

9. Dole. R. and N. D. Gordon, 1983: Persistent anomalies of the extratropical Northern Hemisphere wintertime circulation: Geographical distribution and regional persistence characteristics. *Mon. Wea. Rev.,* **111,** 1567–1586.

10. Eady, E. T., 1949: Long waves and cyclone waves. *Tellus*, **1 (**Part **3),** 33-52**.**

11. Eichelberger, S. J., and D. L. Hartmann, 2007: Zonal jet structure and the leading mode of variability. *J. Climate,* **20**, 5149– 5163.

12. Elliot R. D. and T. B. Smith: A study of the effects of large blocking highs on the general circulation in the northern-hemisphere westerlies. *J. Meteor.*, **6**, 67-85.

13. Evans, K. J. and R. X. Black, 2003: Piecewise tendency diagnosis of weather regime transitions. *J. Atmos. Sci.,* **60**, 1949-1959.

14. Farrell, B., 1988: Optimal excitation of neutral Rossby waves. *J. Atmos. Sci.*, **45**, 163-172.

15. FEMA: https://www.fema.gov/disaster/1640#tabs-2

16. Fleming, E. L., G.-H. Lim, and J. M. Wallace, 1987: Differences between the spring and autumn circulation of the Northern Hemi- sphere. *J. Atmos. Sci.,* **44,** 1266–1286.

17. Franzke C, Feldstein SB, Lee S (2011) Synoptic analysis of the Pacific-North American teleconnection pattern. *Quart. J. Roy. Meteor. Soc* **137**, 329–346.

18. Frederiksen, J.S., 1983: A Unified Three-Dimensional Instability Theory of the Onset of Blocking and Cyclogenesis. II. Teleconnection Patterns. *J. Atmos. Sci.,* **40**, 2593–2609

19. Griffin, K. S., and J. E. Martin, 2017: Synoptic features associated with temporally coherent modes of variability of the north Pacific jet stream. *J. Climate*, **30**, 39-54.

20. Handlos, Z. J., and J. E. Martin, 2016: Composite analysis of large-scale environments conducive to west Pacific polar/subtropical jet superposition *J. Climate* , **29**, 7145-7165.

21. Henderson, S.A., E.D. Maloney, and E.A. Barnes, 2016: The Influence of the Madden–Julian Oscillation on Northern Hemisphere Winter Blocking. *J. Climate,* **29**, 4597–4616.

22. Held, I. M., and A. Y. Hou, Nonlinear axially symmetric circulations in a nearly inviscid atmosphere, J. Atmos. Sci., 37, 515-533, 1980.
Hoskins, B.J. and P.J. Valdes, 1990: On the Existence of Storm-Tracks. *J. Atmos. Sci.,* **47**, 1854–1864.

23. Horel, J.D. and J.M. Wallace, 1981: Planetary-Scale Atmospheric Phenomena Associated with the Southern Oscillation. *Mon. Wea. Rev.,* **109**, 813–829.

24. Hoskins, B.J., I.N. James, and G.H. White, 1983: The Shape, Propagation and Mean-Flow Interaction of Large-Scale Weather Systems. *J. Atmos. Sci.,* **40**, 1595–1612.

25. Hoskins, B.J. and T. Ambrizzi, 1993: Rossby Wave Propagation on a Realistic Longitudinally Varying Flow. *J. Atmos. Sci.,* **50**, 1661–1671

26. Jaffe, S. C., J. E. Martin, D. J. Vimont, and D. J. Lorenz, 2011: A synoptic-climatology of episodic, sub-seasonal retractions of the Pacific jet. *J. Climate*, **24**, 2846-2860.

27. Jayawardena, I. M and Y. L. Chen, A. J. Nash, K. Kodama, 2012: A Comparison of three prolonged periods of heavy rainfall over the Hawaiian Islands. *J. Appl. Meteor.,* **51**, 722-744.

28. Krishnamurti, T.N., 1961: THE SUBTROPICAL JET STREAM OF WINTER. *J. Meteor.,* **18**, 172–191.

29. Legras, B. and M. Ghil, 1985: Persistent Anomalies, Blocking and Variations in Atmospheric Predictability. *J. Atmos. Sci*, **42-5,** 433-471.

30. Lewis, J.M., 2003: OOISHI'S OBSERVATION. *Bull. Amer. Meteor. Soc.,* **84**, 357–370, https://doi.org/10.1175/BAMS-84-3-357.

31. Mak, M., and M. Cai, 1989: Local barotropic instability. J. Atmos. Sci., **46,** 3289–3311.

32. Martius, O., C. Schwierz and H.C. Davies, 2007: Breaking Waves at the Tropopause in the Wintertime Northern Hemisphere: Climatological Analyses of the Orientation and the Theoretical LC1/2 Classification. *J. Atmos. Sci*., **64**, 2576-2592

33. Martius, O., C. Schwierz and H.C. Davies, 2010: Tropopause Level Jet Wave-Guides. *J. Atmos. Sci.,* **67**, 866 – 878.

34. Matsueda, M., M. Kyouda, Z. Toth, H.L. Tanaka, and T. Tsuyuki, 2011: Predictability of an Atmospheric Blocking Event that Occurred on 15 December 2005. *Mon. Wea. Rev.,* **139**, 2455–2470.

35. McIntyre, M.E. and T. N. Palmer, 1983: Breaking Planetary waves in the stratosphere. *Nature*, **305**, 593-600.

36. Moore, R.W., O. Martius, and T. Spengler, 2010: The Modulation of the Subtropical and Extratropical Atmosphere in the Pacific Basin in Response to the Madden–Julian Oscillation. *Mon. Wea. Rev.,* **138**, 2761–2779.

37. Namias, J. 1947: Physical nature of some fluctuations in the speed of the zonal circulation. *J. Meteor.,* **4**, 125-133.

38. Namias, J. and P. F. Clapp 1949: Confluence theory of the high tropospheric jet stream. *J. Meteorology*, **6**, 330-336.

39. NCEP Reanalysis 2: *Boulder, Colorado, USA, from their Web site at http://www.esrl.noaa.gov/psd/*

40. Newman, M., and P. D. Sardeshmukh, 1998: The impact of the annual cycle on the North Pacific/North American response to remote low-frequency forcing. *J. Atmos. Sci*., **55,** 1336–1353.

41. Nielsen-Gammon, J. W. and R. J. Lefèvre, 1996: Piecewise Tendency Diagnosis of Dynamical
Processes Governing the Development of an Upper-Tropospheric Mobile Trough. *J. Atmos. Sci.,* **53**, 3120–3142.

42. Otkin, J. A., and J. E. Martin, 2004. The large-scale modulation of subtropical cyclogenesis in the central and eastern Pacific Ocean. *Mon. Wea. Rev.*, **132**, 1813-1828.

43. Palmén, E., 1948: On the distribution of temperature and winds in the upper westerlies. *J. of Meteorology,* **5**, 20-27.

44. Palmén, E. and C. W. Newton 1969: *Atmospheric circulation systems.* Academic Press., **13,** 606.

45. Pelly, J. L. and B. J. Hoskins, 2003: A new perspective on blocking. J. Atmos. Sci., **60**, 734-755.

46. Penland, C. and P.D. Sardeshmukh, 1995: The Optimal Growth of Tropical Sea Surface Temperature Anomalies. *J. Climate,* **8**, 1999–2024.

47. Pfahl, S., C. Schweirz, M. Croci-Maspoli, C. M. Grams, & H. Wernli, 2015: Important of latent heat release in ascending air streams for atmospheric blocking. *Nature Geoscience.* **8**, 610-614.

48. Reiter, 1963: <u>Jet Stream Meteorology</u>. University of Chicago Press, 513 pp.

49. Rex, D. F., 1950: Blocking action in the middle troposphere and its effect upon regional climate. *Tellus*, **2-3**, 196-211.

50. Röthlisberger, M., S. Pfahl, and O. Martius, 2016: Regional-scale jet waviness modulates the occurrence of mid-latitude weather extremes. *Geophys. Res. Lett.*, **43**, 10,989–10,997.

51. Shutts, G. J., 1983: The propagation of eddies in diffluent jetstreams: Eddy vorticity forcing of ''blocking'' flow fields. *Quart. J. Roy. Meteor. Soc.*, **109**, 737–761.

52. Simmons, A. J. and B. J. Hoskins 1980: Barotropic influences on the growth and decay of nonlinear baroclinic waves. *J. Atmos. Sci.,* **37,** 1679-1684

53. Strong, C. and G. Magnusdottir, 2008: How Rossby wave breaking over the Pacific forces the North Atlantic Oscillation. *Geophys. Res. Lett.*, **35-10**, L10706.

54. Thorncroft, C. D., B. J. Hoskins and M. E. McIntyre, 1993: Two Paradigms of Baroclinic-wave life-cycle behavior. *Quart. J. Roy. Meteor. Soc.* **119,** 17-55.

55. Tibaldi, S., E. Tosi, A. Navarra, and L. Pedulli, 1994: Northern and Southern Hemisphere Seasonal Variability of Blocking Frequency and Predictability. *Mon. Wea. Rev.,***122**, 1971–2003

56. Vimont, D.J., 2012: Analysis of the Atlantic Meridional Mode Using Linear Inverse Modeling: Seasonality and Regional Influences. *J. Climate,* **25**, 1194–1212

57. Wallace, J. M. and D. S. Gutzler, 1981: Teleconnections in the Geopotential Height Field during the Northern Hemispher Winter. *Mon. Wea. Rev.,* **109**, 784-812.

58. Weickmann, K. M., and R. M. Chervin, 1988: The observed and simulated atmospheric seasonal cycle. Part I: Global wind field modes. *J. Climate,* **1,** 265–289.

59. Winkler, C.R., M. Newman, and P.D. Sardeshmukh, 2001: A Linear Model of Wintertime Low-Frequency Variability. Part I: Formulation and Forecast Skill. *J. Climate,* **14**,4474–4494

60. Winters, A. C., and J. E. Martin, 2014: The role of a polar/subtropical jet superposition in the May 2010 Nashville Flood. *Wea. Forecasting*, **29**, 954-974.

61. Yamazaki, A. and H. Itoh, 2013: Vortex–Vortex Interactions for the Maintenance of Blocking. Part I: The Selective Absorption Mechanism and a Case Study. *J. Atmos. Sci.,***70**, 725–742.